Laser Welding of Medium-Manganese Steel

by

Nathan Lun

A thesis
presented to the University of Waterloo
in fulfillment of the
thesis requirement for the degree of
Master of Applied Science
in
Mechanical Engineering

Waterloo, Ontario, Canada, 2016

Author's Declaration

I hereby declare that I am the sole author of this thesis. This is a true copy of the thesis, including any required final revisions, as accepted by my examiners.

I understand that my thesis may be made electronically available to the public.

Abstract

Medium-Manganese (MMn) third generation advanced high strength steel (AHSS) was joined using laser welding. The effects of rapid heating and cooling thermal cycles imposed by laser welding on MMn steel was investigated. Microhardness profiles of large heat input diode laser bead-on-plate (BoP) welds found that the steel was not susceptible to heat affected zone (HAZ) softening. The peak temperature above the upper critical temperature (A_3) was determined to have a significant effect on the microstructure and morphology of austenite in the HAZ. The solidification mode of the diode laser fusion zone (FZ) was primarily columnar dendritic in nature and microsegregation of Mn to the inter-dendritic spaces was observed.

Higher energy density fiber laser welding was used to produce laser welded blanks (LWB) containing MMn steel, high strength low alloy (HSLA) and dual-phase (DP) steel. Columnar dendritic solidification was also observed in fiber laser welds of MMn steel. Dissimilar welds containing HSLA and DP980 were found to produce a martensitic FZ with a fraction of stable austenite. HAZ softening was also absent from microhardness profiles of fiber laser welded MMn steel due to the absence of pre-existing martensite and austenite grain growth. Sub-sized similar MMn steel laser welded tensile blanks were observed to exhibit high joint efficiency with respect to the BM. Tensile testing conducted on dissimilar blanks of HSLA and DP980 were observed to fracture in their respective BM due to a difference in yield and ultimate tensile strength. Formability of similar MMn steel LWB was limited, but welding to HSLA or DP980 improved the LWB formability.

LWBs of MMn steel were investigated for potential as a new press hardened steel (PHS) chemistry. Standard size tensile geometries of MMn steel LWB showed that the FZ was sensitive to loading conditions where large strains begin to accumulate. Heat treating and quenching a LWB at an inter-critical annealing temperature showed that the austenite reverse transformation can occur in the laser weld FZ. Laser weld joint ductility was determined to significantly improve by heat treating at a lower temperature (700 °C) and a shorter time (3-4 minutes) compared to conventional boron press hardened steels.

Acknowledgments

I would like to begin by thanking my academic supervisor Dr. Norman Y. Zhou for giving me an opportunity and a platform to challenge myself.

I would like to express my gratitude to Dr. Elliot Biro of Arcelor-Mittal Dofasco for all his guidance, time and insights. His expertise and professionalism have inspired me to expand my knowledge of welding.

Dr. Michael Worswick and the Forming and Impact Mechanics Research group are gratefully acknowledged for granting access to equipment and assisting with expanding my understanding of forming operations and mechanical testing.

I also wish to extend my expression of gratitude to my CAMJ colleagues; thank you for making my time at the University of Waterloo a memorable one.

Support for this research from Dr. Frank Goodwin and the International Zinc Organization North American GAP collaborators are also gratefully acknowledged.

Finally, to my family; thank you for your sacrifice and unyielding support. Your hospitality and constant encouragement has steadied the ship more times than I can count. Thank you for believing in me.

...In memory of my father

Table of Contents

List of Tables

List of Figures

List of Symbols

α	Ferrite
α'	Martensite
α_{B}	Bainite
δ	Delta ferrite
$\epsilon_{\mathrm{Total}}$	Total engineering strain
ϵ_{YPE}	Yield point elongation
γ	Austenite
σ_{UTS}	Ultimate tensile strength
σ_{YS}	Engineering yield strength
θ	Cementite
A_1	Lower critical transformation temperature
A_3	Upper critical transformation temperature
M_{f}	Martensite finish temperature
M_{s}	Martensite start temperature
wt%	Weight Percent

List of Abbreviations

AHSS Advanced High Strength Steel

3G Third Generation

MMn Medium-Manganese

LWB Laser Welded Blanks

HSLA High Strength Low Alloy

DP Dual-Phase

TRIP Transformation Induced Plasticity

TWIP Twinning Induced Plasticity

BCC Body Centered Cubic

FCC Face Centered Cubic

HCP Hexagonal Closed Packed

BCT Body Centered Tetragonal

SFE Stacking Fault Energy

UFG Ultra-Fine Grain

BoP Bead-on-Plate

OM Optical Microscopy

SEM Scanning Electron Microscopy

EDS Energy Dispersive Spectroscopy

XRD X-Ray Diffraction

DIC Digital Image Correlation

LDH Limiting Dome Height

BM Base Metal

HAZ Heat Affected Zone

SCHAZ Sub-critical Heat Affected Zone

ICHAZ Inter-critical Heat Affected Zone

FB Fusion Boundary

FZ Fusion Zone

CCT Continuous Cooling Transformation

PHS Press hardened steel

EBSD Electron Backscattered Diffraction

Chapter 1

Introduction

1.1 Overview

Utilization of advanced high strength steels (AHSS) has increased substantially in the automotive industry to improve vehicle fuel efficiency without sacrificing crashworthiness. Third generation (3G) AHSS, such as medium-manganese (MMn) steel, have recently gained significant interest as a potential steel chemistry solution to meet desirable mechanical property targets. Furthermore, the increased usage of laser welded blanks (LWB) in the vehicle design process allows for improved steel utilization and allocation in specific structural components. In order to understand the applicability of MMn steels in the automotive industry, research must be conducted on the weldability and mechanical performance of LWB containing MMn steel.

1.2 Problem and Justification

External pressure from regulating bodies governing environmental and safety policies have resulted in competing targets for steel manufacturers. Increasing concern about global warming have enforced targets concerning improvement of vehicle fuel efficiency. In North America, the U.S. Environmental Protection Agency (EPA) and the National Highway Traffic Safety Administration (NHTSA) finalized aggressive Corporate Average Fuel Economy (CAFE) targets to increase average fuel economy of new passenger cars, light-duty trucks and medium duty passenger vehicles from 35.5 miles per gallon (mpg) in 2016 to 54.5 mpg by 2025 [1, 2]. A legitimate method to address the requirements stem from the

correlation between of vehicle curb weight and fuel consumption. For every 10% reduction in curb weight, fuel consumption has been estimated to decrease by approximately 7% for new cars or light trucks [3]. However, design engineers must also consider automotive safety regulations, which ultimately determine the crashworthiness of the vehicle from a structural standpoint. As a result, implementation of advanced high strength steels (AHSS) has been a proven method to achieve compliance with environmental targets by increasing the strength-to-weight ratio of steel structural components. In order to maximize weight savings, LWB of different chemistry and thickness have become commonplace in the automotive industry. Depending on the design criteria, steels with specific mechanical properties can be placed at strategic locations on the blank and stamped as a single part, reducing reinforcements and the need for thicker gauge steels. Therefore, the pairing of AHSS in LWBs satisfy both the environmental and safety regulations while suppressing manufacturing and material costs. With each successive improvement in automotive steel design, the weldability and mechanical properties of new AHSS must be understood in order to determine the production feasibility of the product in high volume manufacturing.

1.3 Objectives

The objective of this thesis is to investigate the effects of laser welding on a novel MMn AHSS. The specific objectives include:

1. Characterize the microstructural effects associated with the rapid thermal cycle induced by laser welding processes
2. Evaluate the mechanical performance of LWB combinations of similar and dissimilar MMn AHSS
3. Investigate the potential for extending MMn LWB to press hardening applications

1.4 Criteria and Constraints

Initial laser processing parameter windows were established following SEP 1220-3 as a guideline. Visual inspection and cross sectioning of welds were assessed according to GMA4485. Tensile testing procedures outlined in ASTM E8-13 were observed for quasi-static uniaxial tensile tests. Nakajima hemispherical dome tests were performed to ISO

12004-2 as a guideline. Further details regarding the specifics of the laser processing, metallography and mechanical testing are outlined in Chapter 3.

1.5 Thesis Outline

The organization of the thesis is as follows:

Chapter 1: Introduction - this chapter includes the thesis overview, justification, objectives and constraints of the research work.

Chapter 2: Literature review - this chapter includes a relevant summary of published literature on laser welding, AHSS and MMn.

Chapter 3: Experimental methods - this chapter summarizes the material chemistry, laser welding process, metallographic preparation, characterization techniques and mechanical testing methods involved in the research effort.

Chapter 4: Microstructure evolution of laser welded MMn steel - this chapter reports on the effects of laser welding on the microstucture evolution on MMn steel with respect to the fusion zone and heat affected zones.

Chapter 5: Microstructure and mechanical properties of fiber laser welded MMn steel - this chapter reports on the correlation between the perceived microstructure to the mechanical properties of laser welded blanks including microhardness, quasi-static uniaxial tension and formability.

Chapter 6: Heat Treatment of laser welded MMn steel - this chapter reports on the mechanical properties achieved by press hardending laser welded blanks of MMn steel.

Chapter 7: Conclusions and recommendations - this chapter summarizes the main findings and contributions of the research and recommends additional avenues for future work.

Chapter 2

Literature Review

2.1 Lasers and Welding

2.1.1 Laser Fundamentals

The term 'laser' is a well-known acronym coined by Gordon Gould which stands for **L**ight **A**mplification **S**timulated by the **E**mission of **R**adiation [4, 5]. In order to achieve lasing behaviour, an active medium capable of optical gain is required. The active medium may consist of gases, liquids, or solids such as rare-earth doped crystals or semiconductors. The commonality behind all types of lasing media results from the ability of the material to absorb external energy (pumping) leading to excitation of electrons by elevating them from a stable ground state orbital to an excited state orbital. Consequently, two types of de-excitation can occur in order for the electron to return to the preferable ground state: spontaneous or stimulated. To achieve stimulated emission, two requirements must be met: population inversion and optical resonance. Population inversion refers to the state in which higher energy levels in the atom are more densely populated than the lower energy levels. The only method of obtaining a condition contrary to natural thermal equilibrium is to artificially increase the energy of the electrons to even higher energy state "pumping levels". Optical resonance is required to ensure that the amount of stimulated emissions are greater than the spontaneous emissions occurring in the lasing medium. The classical example of ensuring the condition is to confine the ends of the lasing medium within parallel reflective mirrors such that sufficient directional intensification can occur. Photons with non-perpendicular directional vectors are subsequently excluded from the lasing medium. As a result, the light emitted by lasers differ from conventional sources by

three unique emission properties: monochromatic emission, coherence and directionality. Monochromatic emission occurs when the photons emitted by the source consists of wavelengths of identical magnitude. Coherence is achieved when the photons are completely in-phase while directionality refers to the same spatial axial direction to which all the emitted photons are aligned. The first publicly recorded operation of a lasing device was conceived by Theodore Maiman in 1960 and the number of laser applications has increased exponentially ever since.

2.1.2 Laser Welding

In terms of materials processing applications, the first recorded utilization of a laser was to cut materials. Shortly after, the advantages of using lasers as a heat source in fusion processes to join materials were realized. The premise of fusion processes for joining materials stems from the liquefaction of two interfaces to create a seamless solidified junction between the prior separate entities. Prior to the advent of laser welding, the vast majority of joining processes employed either electric arc, friction or resistance processes to generate sufficient heat to achieve melting. Laser welding utilizes photonic energy in the form of a monochromatic, coherent and highly collimated point source to generate sufficient heat for fusion. As a result, the energy density of laser sources are much higher than conventional arc, friction or resistance processes for welding applications. Consequently, laser welding processes take form in two distinct modes as portrayed by Figure 2.1.

In conduction mode welding, the incident laser irradiation induces surface melting of the substrate. Both the surface penetration and energy density of conduction mode welding is significantly lower than that of keyhole welding as summarized in Figure 2.1. True to the namesake, conduction mode welding occurs when laser radiation is incident on the material surface and heat is transferred to adjacent atoms by phonons. The resultant weld has a low aspect ratio and can have a significantly wider HAZ when compared to welds made by keyhole mode.

Keyhole welding is characterized by operation in high energy density mode with high resultant weld aspect ratio given that the penetration into the material scales with the energy density. Due to the high energy density, a vertical keyhole is formed within the molten pool resulting causing some vapourization of the material. At sufficient travel speeds, vapour pressure prevents the collapse of the keyhole, thus acting as a stabilizer to allow for greater penetration by trapping the incident radiation [7, 8]. When keyhole mode welding is established in metallic materials, two absorption processes are of main concern: inverse bremsstrahlung and Fresnel absorption [9, 10].

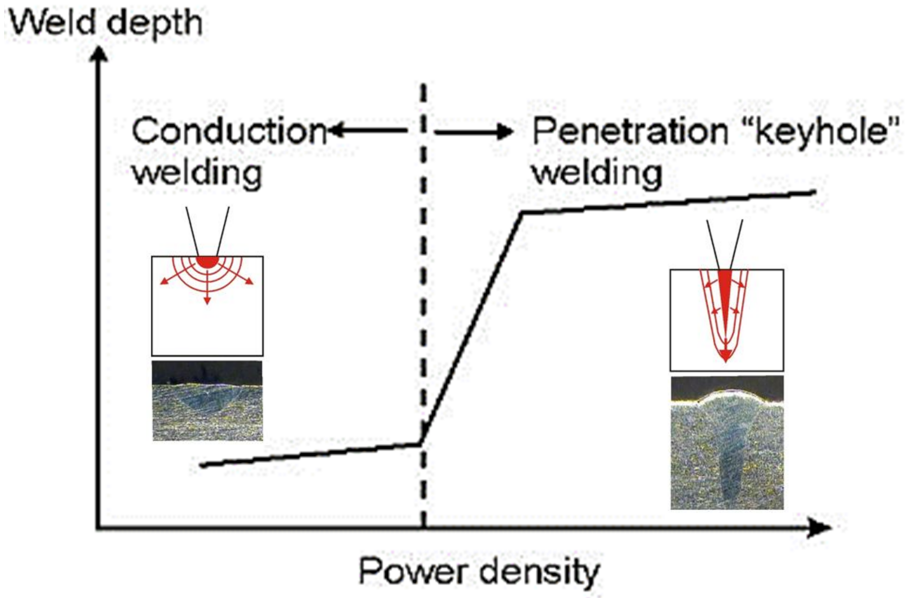

Figure 2.1: Difference between conduction and keyhole laser welding modes [6]

Inverse Bremsstrahlung absorption occurs as the free electrons in the ejected plume of heavy metal ions absorb energy from the incident laser light and increase in kinetic energy [11]. The kinetic energy increases to a point at which impact ionization with other metal gas atoms is achieved, electrical breakdown ensues and a plasma is generated above the keyhole [11]. The result is a decrease in laser efficiency as the plume absorbs the incident photons to sustain the plasma. The laser induced plasma raises the internal temperature of the keyhole by protecting the walls from colder atmospheric gases [9]. Fresnal absorption occurs with the remaining laser energy that is not subjected to inverse bremsstrahlung absorption. According to Zhou, the keyhole formation improves laser light absorption by causing multiple reflections within the cavity [9].

2.1.3 First Generation Industrial Lasers

The first lasers used for material processing purposes consist mainly of sealed tube gaseous gain medium; most notably a combination of CO_2, N_2 and He. The gain medium is electrically pumped using a variety of methods such as direct current or radio frequency discharge. The main constituent in the gain medium is CO_2 gas, which attain excitation when colliding with N_2 molecules. The high thermal conductivity of He is used to remove

heat and also coupled as a depopulating medium. The typical wavelength emitted by CO_2 lasers is on the order of 10.6 μm and can operate at extremely high power (up to 50 kW). Traditionally, CO_2 lasers require a significant array of optical components to direct the light from source to the workpiece. Power output scales with lasing medium cavity length and as such, large kW units may occupy copious amounts of floor space. A shift in technology occurred with the introduction of the solid state gain medium. Neodymium doped Ytterbium Aluminum Garnet (Nd:YAG) crystals were first discovered to exhibit lasing behaviour by Geusic et al. in 1964 [12]. The ability to dope crystals to shift the energy states within a gain media enabled the expansion of lasers to a broader range of wavelengths (i.e. 1.06 μm). This lead to a massive increase in laser applications for different types of materials.

2.1.4 Second Generation Industrial Lasers

The second generation of lasers used for material processing purposes were realized by the extension of the solid state laser to different configurations. The realization that solid state gain mediums could be utilized to develop high energy beams allowed for increased design flexibility. The burgeoning semiconductor industry and popularization of light emitting diodes (LEDs) improved the optical pumping method over traditional mercury flash lamps. Along with the improved thin-film and micro-fabrication techniques, it was proved that specific semiconductor P-N junctions were capable of lasing phenomena by directly applying current. The large active region between the p-type and n-type semiconductors acts as the gain media. Power scaling can be achieved by simply increasing the number of diodes in a stack. High powered diode lasers emit laser light from a narrow waveguide, as a result, the beam is prone to diffracting. Consequently, the beam generally exhibits a Gaussian energy distribution over an elliptical profile [13]. The lower energy density restricts diode laser to conduction mode welding [14]. A critical aspect of the design was to develop thin film means to act as optical resonators for high power operation. As a result, Bragg gratings, which consisted of alternating thin films of materials with specifically designed refractive indices, were utilized to contain desired emission wavelength.

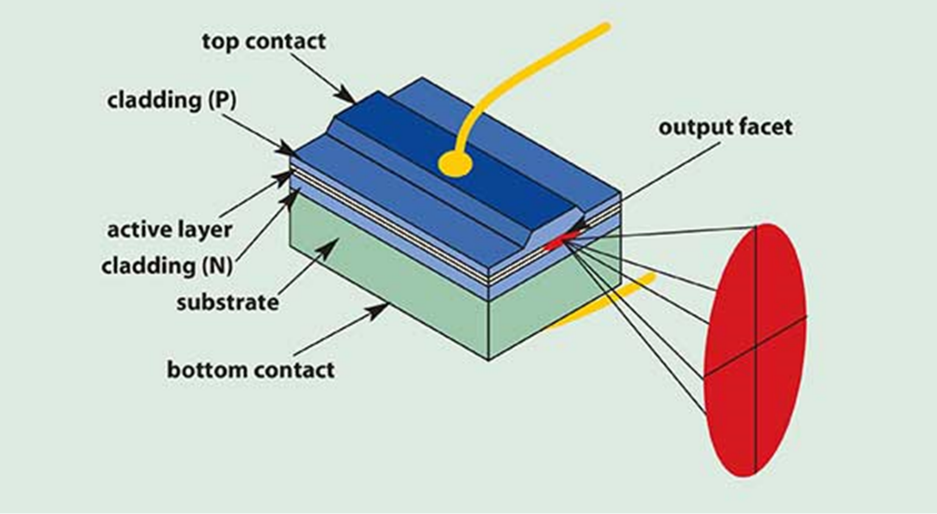

Figure 2.2: Schematic structure of a high powered diode laser [15]

2.1.5 Third Generation Industrial Lasers

The popularization of optical fiber technologies as a medium for confining optical transmissions for data transfer ultimately lead to the commercial development of fiber lasers. Although the concept of achieving optical resonance within a fiber was demonstrated in the early 1960, the cumulative improvements in semiconductor doping, transmission technology and production costs facilitated the industrialization of high powered, flexible lasers [16]. The miniaturization of Bragg gratings to be included in the optical fiber also allowed for wavelength specific confinement, enabling the production of self-contained laser systems with unparalleled scalability and beam quality [17]. Fiber laser are generally diode-pumped systems, and due to the large surface area of the fiber, improvements in heat dissipation contributes to industry leading wall-to-plug energy efficiencies. The combination of reliable beam quality, system flexibility and energy efficiency have propelled fiber lasers to the forefront of material processing applications in recent years.

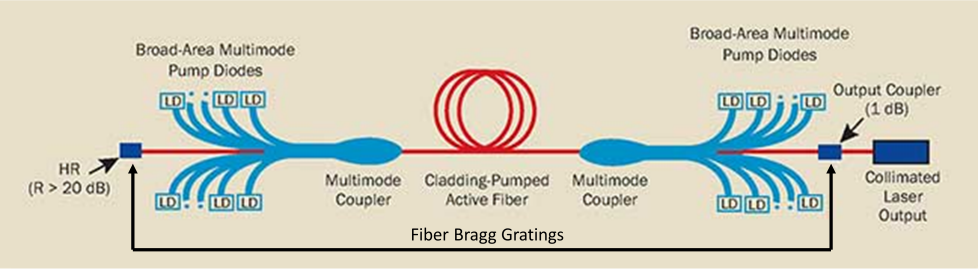

Figure 2.3: Schematic illustration of a fiber laser system (HR: high reflector, R:extinction ratio)[18]

2.2 Laser Welded Blanks

The pressures to meet regulatory requirements for fuel efficiency in vehicles have pushed manufacturers to look at different options for light weighting. One such alternative design process involves the concept of using materials specific to the application. In the body-in-white structure, components are designed to fulfill different load bearing requirements such as stiffness, energy dissipation and adsorption. The usage of LWB enables greater flexibility in the design process and reduced costs by enabling the joining of different steel chemistries and thicknesses prior to stamping. The first mass production components to implement LWB technology were floorpans made by Thyseen Stahl AG for Audi in 1985 [19, 20]. With the improvement in technology and economies of scale, the utilization of LWB in the automotive industry has increased ever since [21, 22].

2.2.1 Weldability

Weldability of steel LWB is predicated on the ability of the steels to form an acceptable joint. Conventional AHSS steels with similar coatings and chemistries are relatively simple to laser weld, however, the general movement to higher strength steels and the introduction of new coatings and alloys have made weldability an important metric for steel manufacturers. Quality metrics to assess the weldability of LWB include assessing joint geometry, internal porosity and mechanical properties.

2.2.2 Laser Welding Parameters

Key welding parameters for laser welding include laser power, welding speed, defocusing distance and offset distance. Clamping and joint fit-up can also have a significant effect on the final joint geometry. For CO_2 lasers, the shielding gas has been found to significantly affect the weld quality due to the interaction of the specific laser wavelength. For shorter wavelength lasers such as Nd:YAG and fiber lasers, the laser-gas interaction is limited, thus, shielding gas is mainly used for cosmetic purposes and displacement of the plasma plume. For non-autogeneous welds, parameters such as filler wire composition and wire feed rate are important factors to consider.

2.3 Advanced High Strength Steels

2.3.1 First Generation Advanced High Strength Steel

Automotive manufacturers and steel makers alike have consolidated different advanced high strength steel (AHSS) grades into generational categorizes according to the ultimate tensile strength and total elongation. Although such organization leads to severe oversimplification of the mechanical properties for a wide spectrum of steels, it has been frequently used to focus research and development efforts. Figure 2.4 demonstrates the wide spectrum of mechanical properties that are available with current technology.

Development of the first generation AHSS primarily focused on achieving improved strength and ductility through metallurgical and thermo-mechanical modification of the body center cubic (BCC) crystallographic structure of ferrite (α) based microstructures. These steels employ a wide range of metallurgical techniques to achieve increased mechanical processes. For example, grain size refinement through microalloying additions of Ti, Nb and V in high strength low alloy (HSLA) steel allowed for the direct manipulation of the α grain size by introducing carbide nucleation. A smaller grain size leads to an increase in tensile strength according to the Hall-Petch relation by impeding the movement of dislocations through the α matrix [24, 25, 26]. Furthermore, higher alloying constituent steels have been successfully inter-critically annealed to produce dual-phase (DP) steels which have a duplex microstructure containing martensite (α') and α [27]. The total tensile strength achievable by DP steel is dependent upon the volume fraction of α'. Careful manipulation of the chemical composition and the heat treatment of the steel can tailor the mechanical properties of the steel to specific applications. However, steels classified as first generation AHSS typically exhibit an inverse relationship between tensile strength and

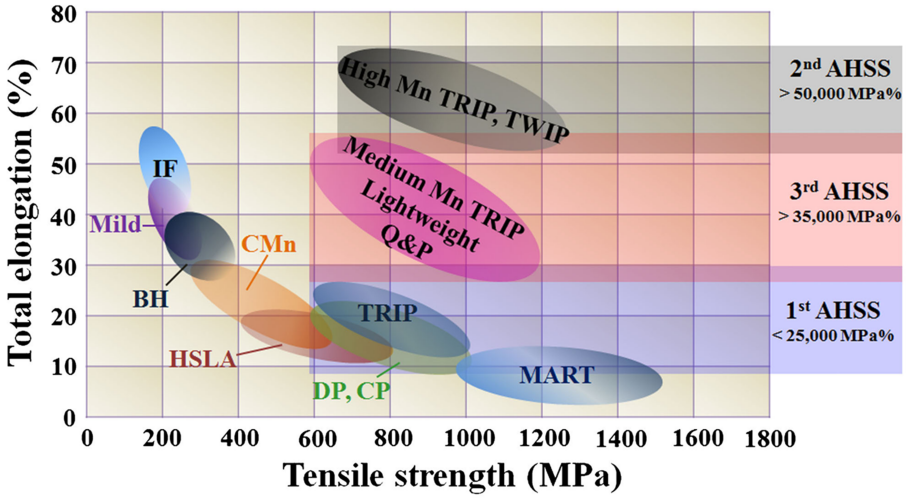

Figure 2.4: Advanced high strength steels and their mechanical properties [23]

elongation. Higher martensite volume fractions, which contribute to extremely high tensile strengths, are offset by a decrease in ductility. As such, the approximate product limit of the ultimate tensile strength σ_{UTS} and total elongation is <25,000 MPa%. Transformation induced plasticity (TRIP) steels containing less than 2.5wt% Mn were also classified as a first generation AHSS because the volume fraction of austenite (γ) was very small. Usage of LWB consisting of first generation AH SS has been thoroughly researched and successfully implemented into vehicle design [28, 29, 30]. More recently, applications of LWB to press hardened steel (PHS) have enabled the production of full door panels exhibiting ultra-high strength steels [31, 32].

2.3.2 Second Generation Advanced High Strength Steel

It was soon discovered that high tensile strength and elongation need not be inversely proportional when the steel consisted of room temperature stable γ rather than α. Manganese, an effective solid solution hardening element in all types of steel, was determined to be a more cost effective solution than employing large amounts of nickel, another γ stabilizing element [33]. Therefore, the majority of second generation AHSS are based on high-Mn steels which depend on the ability the austenite phase to dynamically work harden through the TRIP or Twinning Induced Plasticity (TWIP) effect. TRIP steels typically

differ from TWIP steels due to the stress-induced transformation of the face center cubic (FCC) γ into the hexagonal closed packed (HCP) structure of ϵ-martensite. The fundamental mechanism by which the TRIP effect occurs is a result of the ability of the atoms in γ to accommodate stress by the rearrangement in the crystallographic system. The TRIP effect has been determined to occur only if the stacking fault energy (SFE) of the steel is less than 18-20 mJm^{-2} [34]. Conversely, the TWIP effect was determined to occur in steels with SFEs of greater than 20 mJm^{-2} [35]. The TWIP effect occurs when the FCC structure of the austenite phase accommodates the induced plastic strain by preferentially creating a mechanical twin, which as shown in Figure 2.5, enables the dissipation of strain energy throughout the lattice to delay fracture. As a result, the product between σ_{UTS} and total elongations achievable by both high manganese TRIP and TWIP steel can exceed 50,000 MPa%.

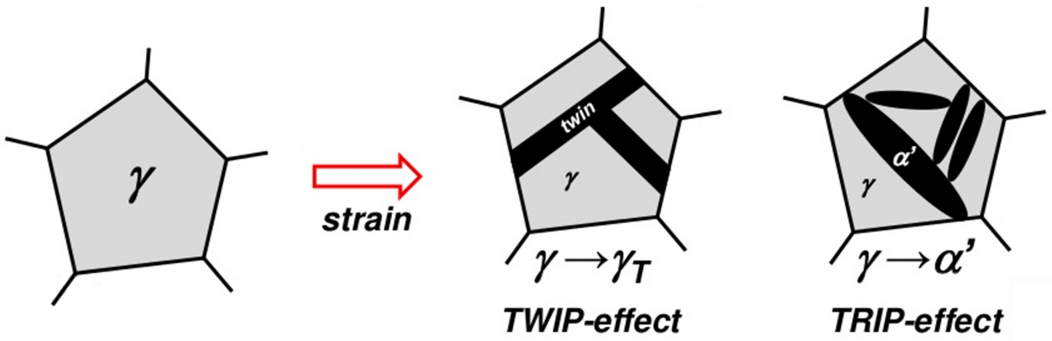

Figure 2.5: TRIP and TWIP strain hardening effects [36]

2.3.3 Third Generation Advanced High Strength Steel

Due to the large discrepancy between the first and second generation AHSS, a bimodal distribution of AHSS steel mechanical properties occurred. The genesis of which, was a direct result of two opposite approaches to achieving high strength without sacrificing ductility. In the first generation AHSS, strength and ductility were inversely proportional due to the modification of the α based microstructure modification. Comparatively, in second generation AHSS, strength and ductility can both be realized at the expense of cost savings, given that high-Mn steels generally require more sophisticated methods and processes to produce. Furthermore, issues with delayed hydrogen induced cracking [37, 38], liquid metal embrittlement [39, 40, 41, 42] and poor weldability [43, 44, 45, 46, 47] have

prevented the wide-spread adoption of second generation AHSS. As a result, a concerted effort led by the United States National Science Foundation 2007 sought a more practical compromise between the two largely unassociated generations of AHSS [48]. The United States Department of Energy (DoE) set two mechanical property targets for these third generation steels: first at >1.2 GPa σ_{UTS} and >30% total elongation and the second at >1.5GPa σ_{UTS} and >25% total elongation which fall into the product range between 30,000 - 50,000 MPa%.

Several different solutions have been proposed for achieving third generation mechanical properties. Most notably, quench and partitioning (Q&P) and MMn steels have been shown to exhibit promising properties. Both Q&P and MMn steels achieve the desired mechanical properties by increasing the volume fraction of retained austenite (γ_{RA}) in the base metal to promote additional work hardening and beyond the capabilities of the first generation AHSS. In the context of AHSS classification, conventional Q&P steel refers to C-Mn-Si steels which are austenized at a temperature above A_3, then rapidly cooled to a temperature between martensite start (M_s) and martensite finish (M_f)to achieve a certain volume fraction of martensite and retained austenite. The temperature of the steel is then subsequently raised to an intermediate temperature which promotes the carbon partitioning into γ_{RA} in order to enhance its stability at room temperature. MMn steels follow similar processing routes to achieve high γ_{RA} volumes, the main difference being chemistry and annealing temperature.

2.4 Medium-Manganese Steel

2.4.1 Chemistry

According to De Cooman [36] and Lee *et al.* [23] the definition of a MMn steel should be restricted to steels containing a Mn concentration between 3-12 wt%. This general definition distinguishes this class from the high-Mn steels (>12wt% Mn) in the second generation AHSS. The earliest publication of a MMn steel chemistry was reported by Miller in 1972 containing Fe-5.7Mn-0.1C [24]. The chemistry remained in obscurity until recently, where various research groups began considering higher solid solution alloying contents as a viable means to increase steel strength for automotive applications. Furukawa experimented with several different combinations, namely adding silicon to improve the work hardening of the α matrix of a Fe-5.3Mn-0.1C-2.0Si steel [49]. Han *et al.* [50] investigated the effects of initial quenched martensite on the microstructural evolution of a partitioned Fe-8.5Mn-0.05C-0.1Al-0.3Si steel. De Cooman [36] produced extensive work

of a 10Mn-xC-3Al-0.5Si steel evaluating the microstructure and metallurgical behaviour. More recently, three different research groups employed different MMn steel chemistries for press hardening applications: Yi *et al.* [51] reported using a MMn steel containing Fe-(5-8)Mn-(0.2-0.4)C-(0.7-2.5)Si, Rana *et al.* [52] used a Fe-9.8Mn-0.2C-1.4Al-0.2Si steel and Han *et al.* [50] used a Fe-(5-12)Mn-(0.1-0.2)C-(<2.0)Al-(0.1-2.0)Si steel. From the large variation in chemistries, it is evident that MMn steels show promising characteristics as a viable third generation AHSS.

Effect of Carbon

Carbon is an interstitial solute atom and the main alloying element that contributes to the hardenability in steel. Low carbon steels exhibiting carbon concentrations <0.85wt%C, are hypoeutectoid in nature and generally have a tendency to exist as allotromorphs of BCC α and cementite (θ). In a binary equilibrium system of Fe-C, room temperature γ is not thermodynamically stable. When steel is brought up to a high enough temperature to form γ then quenched rapidly, γ transforms displacively to metastable body centered tetragonal (BCT) α' and becomes supersaturated with carbon. At certain elevated isothermal temperatures, carbon has been found to exhibit strong partitioning behavior towards the FCC structure of γ_{RA} [53]. The binary equilibrium Fe-C phase diagram shows that carbon effectively expands the γ-phase region as shown in Figure 2.6 [54]. By promoting C partitioning from the supersaturated α' to the γ_{RA}, it is possible to obtain room temperature stable (γ) [53].

Effect of Manganese

Manganese is a substitutional solute atom and another major alloying element used in conventional steels to increase strength and hardenability. Unlike the Fe-C equilibrium diagram, the Fe-Mn diagram does not contain a closed γ-phase region, instead, the addition of Mn to steel effectively expands the solid solution γ-phase field by lowering the A_3 critical line according to Equation 2.1.

$$A_{c3} = 955 - 350C - 25Mn + 51Si + 106Nb + 100Ti + 68Al - 11Cr - 33Ni - 16Cu + 67Mo \quad (2.1)$$

Furthermore, the M_s temperature is also reduced with additional Mn content as shown in Equation 2.2.

$$M_s = 539 - 423C - 30.4Mn - 7.5Si + 30.0Al \quad (2.2)$$

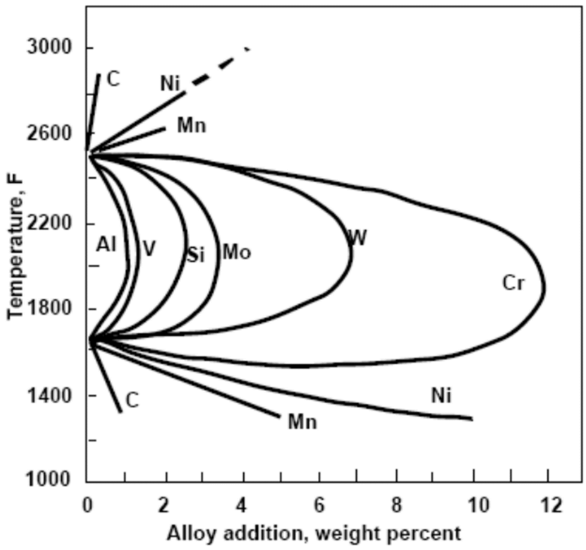

Figure 2.6: Austenite regions in different iron-alloy binary systems [54]

The combined effect results in a downward shift of the M_s temperature and a suppression of the α_B nose in the continuous cooling transformation (CCT) diagram as shown in Figure 2.8.

Steels containing high concentrations of Mn such as TWIP and Hadfield steels exhibit stable γ microstructures for this reason. Special efforts to control the sulphur concentration in high Mn bearing steels must be taken in order to reduce the propensity to form MnS inclusions which are severely detrimental to the solidification behaviour of as cast slabs and welds. This stems from the fact that Mn exhibits high activity levels in the molten state. At high enough concentrations, Mn also has a tendency to form stable carbide complexes in steel as evident in Figure 2.7. During non-equilibrium solidification, Mn has a tendency to enrich the liquid film at the solidification front due to a difference between solubility in the growing solid and the molten steel, resulting in segregation between dendrite cores in high-Mn steels [45, 55, 47].

Effect of Silicon

Addition of Si to the steel melt is an effective method to improve α solid solution strengthening. However, unlike Mn, Si exhibits a closed γ-phase region and is much more effective as an α-phase stabilizer [54]. In high Mn steels, Si is an important element in controlling

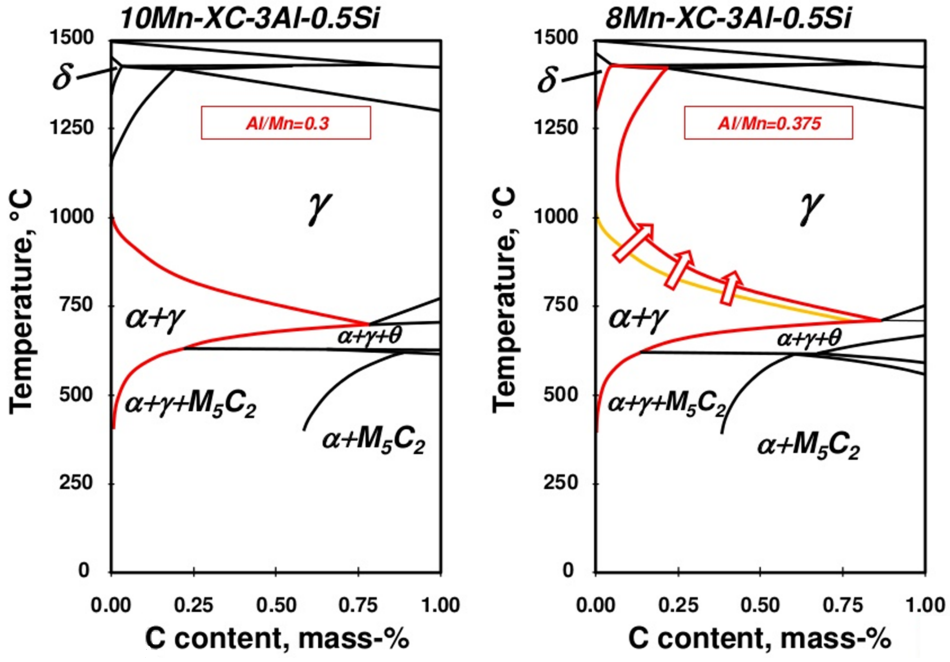

Figure 2.7: Equilibrium phase diagrams illustrating the effect of Mn on the A_3 temperature in MMn steels [36]

the SFE and suppressing the formation of cementite [36]. During inter-critical annealing, the bulk movement of Si solute atoms is generally towards the α phase .

Effect of Aluminum

The addition of Al is particularly useful in controlling the SFE of austenitic carbon steels. Although Al additions to high Mn steels do not typically exceed >3wt%, it has an significant affect on the formation of δ-ferrite. The primary purpose of Al in MMn steel is to expand the dual $\alpha + \gamma$ inter-critical region in the phase diagram which enables an increase in the C content in γ [36]. During intercritical annealing, the bulk movement of Al solute atoms is generally towards α.

2.4.2 Processing

In order to achieve a substantial γ volume required to improve dynamic work hardening and achieve greater ductility expected of third generation AHSS, MMn steels have been

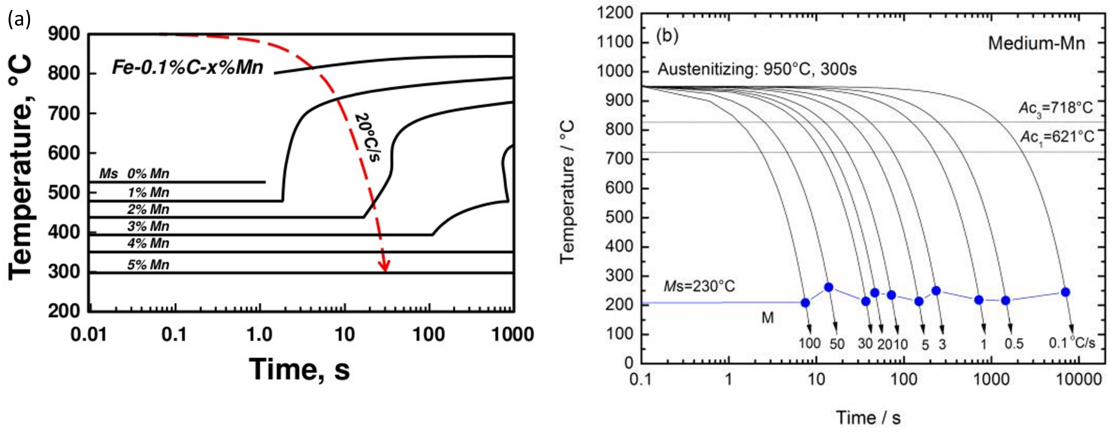

Figure 2.8: Continuous cooling transformation diagrams of (a) Fe-xMn-0.1C and (b) Fe-9Mn-0.05C steels [36, 56]

subjected to two different processing routes. Figure 2.9 illustrates the transformation routes that can be used to produce MMn steel. One such method is to austenitize the steel after quenching and induce a $\gamma \rightarrow \alpha$ transformation by cooling to the inter-critical region between A_3 and A_1, then performing an isothermal hold. The other method is to inter-critically anneal the steel directly after quenching to induce a α' $\rightarrow \gamma$ reverse austenite transformation. Nakada *et al.* [57] investigated the differences in the processing routes in a Fe-5Mn-0.1C MMn steel and found that the α' $\rightarrow \gamma$ transformation occurred significantly faster than the $\gamma \rightarrow \alpha$ transformation. As a result of this phenomenon, the processing times required to achieve target microstructure and mechanical properties for MMn steel is economically feasible as some research groups have reported achieving third generation AHSS mechanical property targets with inter-critical annealing times of 120 s [58].

Processing of MMn steel is predicated on the α' $\rightarrow \gamma$ reverse austenite transformation. The primary exploit of the heat treatment schedule required to obtain an ultra-fine grain (UFG) duplex microstructure of α and γ is dependent on the partitioning of C and Mn from the super-saturated α' into γ which is necessary to stabilize the γ phase [59, 33]. Figure 2.10 illustrates the partition effect on the stabilization of γ during the reverse transformation.

In 1972, Miller found that steel containing Fe-5.7Mn-0.1C resulted in an ultra-fine lamellar grain structure to which he associated with alternating layers of room temperature stable γ and α. This microstructure has been consistently reported numerous times by multiple different international research groups since [49, 61, 62, 63, 58, 56]. The mechanism by which the ultra-fine lamellar structure arises from the initial microstructure of the α'

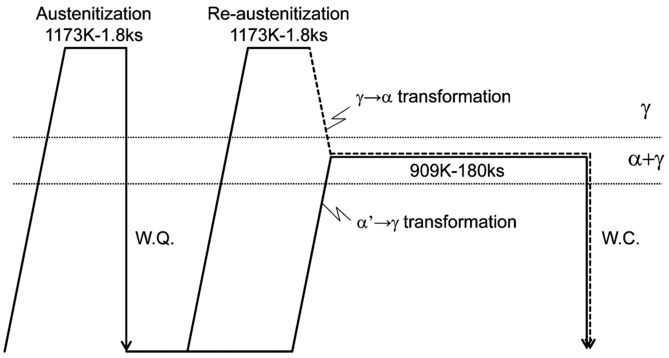

Figure 2.9: Heat treatment schedules for different transformation routes in MMn steel [57]

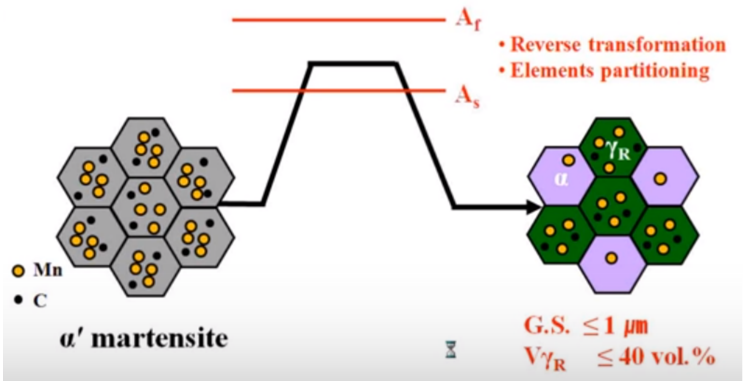

Figure 2.10: Schematic illustration of the partitioning of C and Mn to stabilize austenite during the reverse transformation [60]

is shown in Figure 2.11. The high angle boundaries corresponding to prior austenite grain boundaries (PAGB) and block/packet boundaries of the α' microstructures are ideal high energy nucleation sites for austenite upon inter-critical annealing [64]. According to Shi *et al.* [65, 66], carbides nucleate at the low angle boundaries where the dislocation density is high, which in turn, provides nucleation sides for γ. With increasing annealing time, it has been suggested that the carbides redissolve into the solid solution and austenite volume fraction continues to increase, eventually nucleating at some low angle boundaries as well (Figure 2.11) [66].

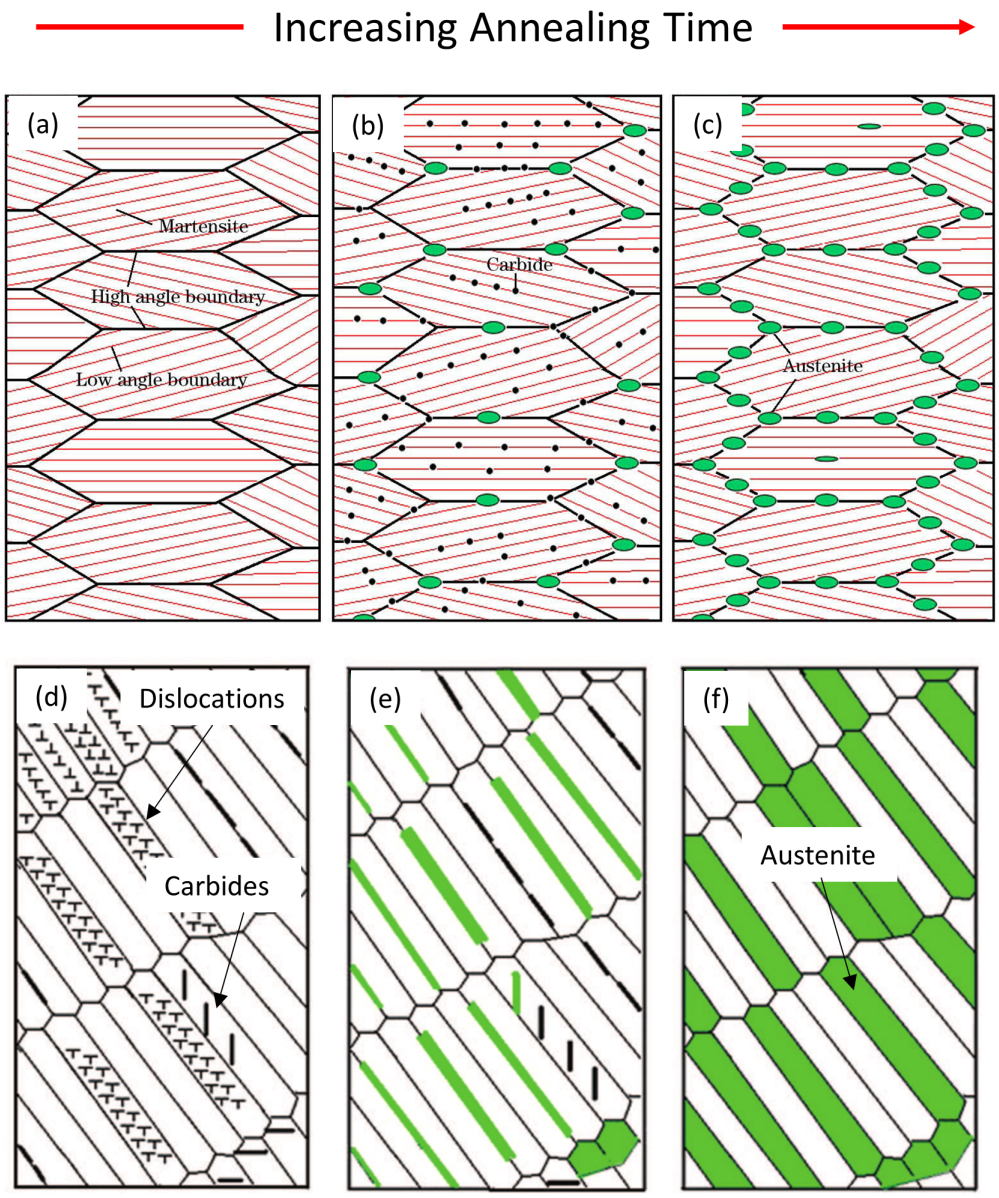

Figure 2.11: Schematic illustration of the macroscopic nucleation of austenite (a-c) during inter-critical annealing and the microscopic evolution (d-f) of the ultra-fine lamellar structure of MMn steels during the austenite reverse transformation [65, 66]

Chapter 3

Experimental Methods

3.1 Materials

The materials used throughout the research work include galvanized HSLA, DP980 and MMn steel. The chemical compositions of the steels are summarized in below in Table 3.1. The carbon equivalency (CE_N) is calculated by Equation 3.1 below.

Table 3.1: Chemical composition of steels used (wt.%)

Steel	**C**	**Mn**	**Si**	**Al**	**CE_N**
MMn	0.15	10.4	0.17	1.49	N/A
HSLA	0.05	0.56	0.12	0.03	0.12
DP980	0.09	2.11	0.31	0.30	0.37

$$CE_N = C + A(c)(Si/24 + Mn/6 + Cu/15 + Ni/60 + (Cr + Mo + Nb + V)/5 + 5B) \quad (3.1)$$

Where:

$$A(c) = 0.75 + 0.25tanh(20 * (C - 0.12)) \quad (3.2)$$

The BM microstructures of the MMn, HSLA and DP980 steels are illustrated by the micrographs in Figure 3.1. The MMn steel microstructure comprised a mixture of ultra-fine lamellar structure of γ embedded in a α matrix (Figure 3.1(a)). The average width of the γ laths ranged from approximately 100 - 400 nm. Denser lamellar colonies were observed dispersed throughout the steel and exhibited narrower lath widths. The microstructure was consistent with findings from literature which reported that inter-critically annealed

MMn steels are prone to developing lamellar duplex microstructures of γ and α [23, 62, 67, 63, 56, 68]. The microstructure of the HSLA steel was found to consist of finely dispersed carbides in α grains with a measured average grain size of 7.15 ± 0.73 μm (Figure 3.1(b)). The DP980 steel contained α' islands embedded in a ferritic matrix with a small fraction of retained austenite (Figure 3.1(c)).

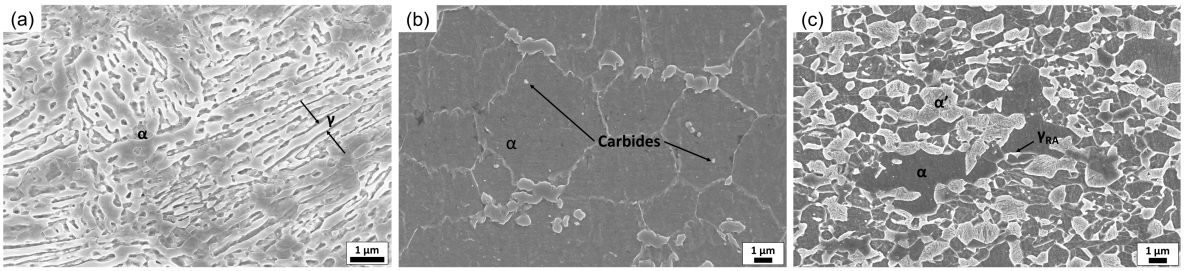

Figure 3.1: SEM micrographs showing the base metal of (a) MMn, (b) HSLA, and (c) DP980; (α: Ferrite, γ: Austenite, α': Martensite).

3.2 Metallographic Preparation

Metallographic preparation was conducted by isolating a specimen of desired dimension using an abrasive cut-off saw. Specimens were hot mounted in conductive phenolic compound (Struers Polyfast^{TM}) and ground using consecutively finer silicon carbide papers (180, 600, 1200grit). Polishing was accomplished by using diamond suspension sprays (LECO$^{®}$) of particle sizes 0.6 and 0.1 micron. Additionally, in order to eliminate mechanically stress induced transformation of γ to ϵ during rough grinding, vibratory polishing (Buhler VibroMet^{TM}) was performed using a 0.01 micron colloidal silica suspension for approximately 1 hour. Metallographic etching was performed using a solution of 4% Nital for 2-4 seconds for optical microscopy and scanning electron microscopy purposes. Occasionally, a colour tint etching step with 5% sodium metabisulphite was used to increase contrast for optical microscopy.

3.3 Microhardness

Microhardness testing was performed on polished and etched weld cross sections using a Clemex-JS 2000 automated hardness tester with a 200 g load and 15 s dwell time.

Indentations were sequentially distanced 2-3 times the diagonal to avoid strain field effects of the adjacent indents. For cross section microhardness profiles in fiber laser welds, the pattern in Figure 3.2 was used to obtain higher resolution hardness trends in the HAZ.

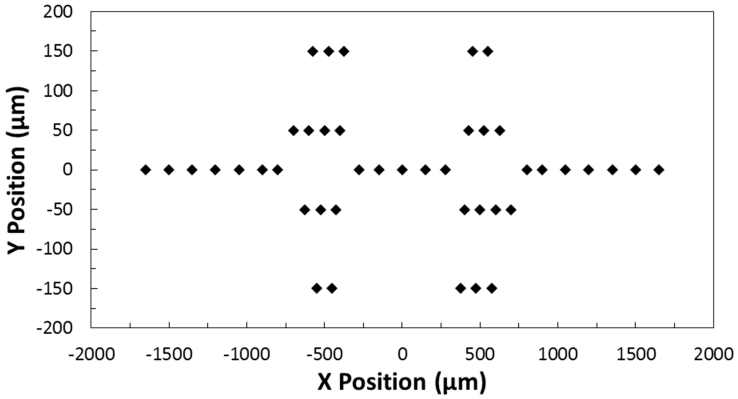

Figure 3.2: High resolution microhardness profile

3.4 Characterization

3.4.1 Microscopy

Optical microscopy (OM) was performed using a Olympus BX51M microscope with QCapture Pro Ver. 5.1 imaging software. Scanning electron microscopy (SEM) imaging (ZEISS LEO 1530) was conducted using a field emission gun under 10-15 kV accelerating voltage with a magnification range from 500 to 30,000X. Energy Dispersive Spectroscopy (EDS) (EDAX) was performed using the same accelerating voltage and a standard acquisition time of 60-100 seconds.

3.4.2 X-Ray Diffraction

X-ray diffraction (XRD) was conducted using a Co (k_α=1.79026Å) sealed tube source (Bruker D8 DISCOVER with a DAVINCI.DESIGN diffractometer). A power setting of 35kV and 45mA was used in conjunction with a microslit of 0.5 mm and a short collimator of 0.5 mm. A coupled θ-2θ scan with a frame exposure of 1200s/frame for 4 frames was

used for a 2θ range of 44-126^0. 2D frames were collected with DIFFRAC.Measurement Centre Version 3.0 software and integrated to 1D using a DIFFRAC.EVA Version 4.0, and displayed and analyzed in Topas Version 4.2 (all from Bruker-AXS). The austenite volume fraction was calculated by using the Rietveld refinement method which uses a full pattern analysis to integrate the characteristic peaks.

3.5 Microstructure Evolution of Laser Welded Medium-Manganese Steel

Diode laser welding was used to study the effects of non-isothermal heating on the γ stability of MMn steel. A Nuyvonx ISL-4000L diode laser head mounted on a 6-axis industrial robot was used to perform the welds (Figure 3.3). A 4 x 4 bead on plate (BoP) process optimization matrix was completed in order to select an appropriate welding parameter for the study. After parameter optimization, a surface focused laser power of 4kW and a linear robot movement speed of 1 m·min^{-1} was selected for the trials. Argon gas with a flow rate of 14 L·min$_{-1}$ was used as an a side assist gas to clear the weld zone of the plasma plume during welding.

Figure 3.3: Nuvonyx-4000L diode laser and 6-axis Panasonic robot

MMn steel specimens were sheared into 50 mm x 200 mm rectangles and degreased with ethanol prior to welding. Four 0.5 mm diameter holes were drilled on the back of the steel

blanks to 0.3 mm, 0.6 mm, 0.9 mm and 1.2 mm depths. K-type thermocouples were welded into the holes by capacitive discharge, with another thermocouple placed on the back surface (0 mm). A clamping fixture with an open back channel for thermocouple routing was used to restrict specimen movement and prevent heat warping. The thermocouples were connected to a data acquisition system (National Instruments: cDAQ-9171) running ExpressView to acquire the in-situ temperature during laser welding.

Cross section samples were cut from thermocouple placement locations to compare the microstructure and microhardness against the thermal profile experienced during welding. Further details regarding standard metallographic preparation procedure can be found the the aforementioned section.

3.6 Microstructure and Mechanical Properties of Fiber Laser Welded Medium-Manganese steel

The effects of fiber laser welding on the microstructure and mechanical properties of laser welded blanks containing MMn, HSLA and DP980 steels. A IPG Photonics YLS-6000L connected to a laser welding delivery head (Laser Mechanisms) was used to perform the welds (Figure 3.4). A 4 x 4 BoP process optimization matrix was completed in order to select an appropriate welding parameter for the study. After narrowing down the acceptable process envelope, several trials were conducted in the butt joint configuration. It was determined that in order to meet the weld geometrical requirements of GMA4485, it was necessary that a defocusing study be conducted to avoid excessive concavity. From the optimization studies, it was determined that laser power of 4kW and a linear robot movement speed of 12 $m \cdot min^{-1}$ with a defocus distance of 5mm above the blank surface was capable of achieving full penetration welds with acceptable geometry. Argon assist gas was used during the welding process, with a side and back-shield channel delivery flow rate of approximately 14 $L \cdot min_{-1}$ and 21 $L \cdot min_{-1}$ respectively.

Steel blanks were sheared into rectangles of 100 mm (RD) x 200 mm. The 200 mm edge used to form the butt joint was mechanically milled, deburred and degreased with ethanol to ensure a near perfect fit-up. The prepared blanks were clamped in a welding fixture with a slotted back channel shown in Figure 3.5. The clamping bar was held down by finger clamps at the start, middle and end to prevent the blank from warping during laser welding. After welding, the 200 mm x 200 mm blanks were allowed to cool to room temperature under ambient conditions.

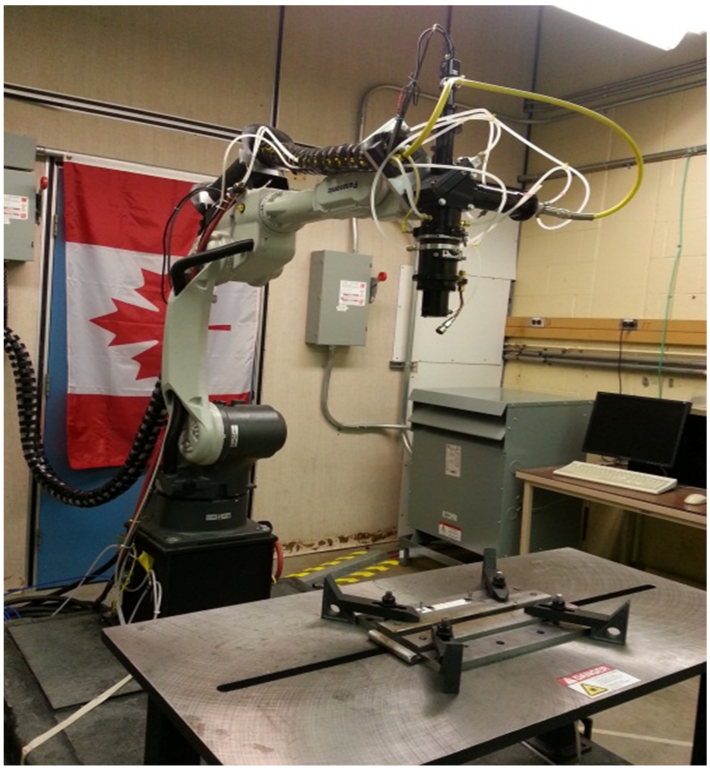

Figure 3.4: IPG Photonics YLS-6000L fiber laser and 6-axis Panasonic robot

In order to obtain representative cross sections of the welded joint, 20 mm from the laser start and stop of the sheared from the blank and discarded. Cross sections were taken from the blank for metallographic analysis and microhardness testing. 10 mm x 10 mm specimens containing the weld line were also prepared for XRD analysis.

Additional laser welded blanks using the same optimized welding parameters were produced for mechanical testing. Sheet-type sub-sized tensile specimens were machined from the laser welded blank with the laser weld perpendicular to the gauge length according to the dimensions listed in ASTM E8-13 as shown in Figure 3.6. Three dimensional digital image correlation (DIC) by Correlated Solutions Inc. was used to observe and assess uniaxial tensile testing conducted in a Tinius Olsen H10KT tensile system at a constant cross head speed of 10 $mm \cdot min^{-1}$. Tensile specimens were degreased with ethanol and speckled with a randomized black-on-white pattern using spray paint. Step and subset sizes used for the DIC analysis were 19 and 7, respectively. Image capture of the DIC system was conducted at a frequency of 4 Hz. All tensile tests were repeated three times and the

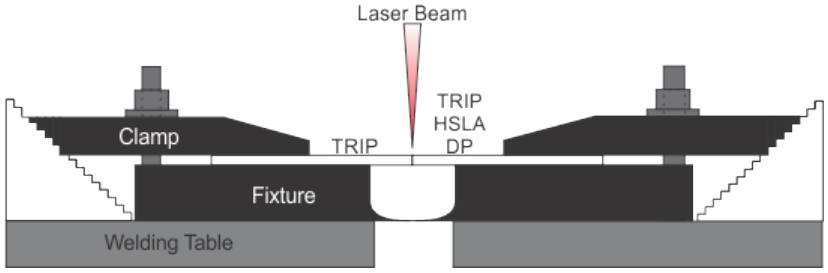

Figure 3.5: Schematic illustration of fiber laser welding fixture

average values are reported. Bi-axial stretch forming was assessed through conducting

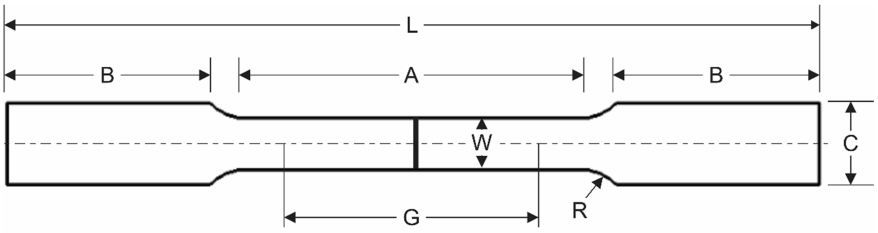

Label	G	W	R	L	A	B	C
Dimension (mm)	25	6	6	100	32	30	10

Figure 3.6: Subsize uni-axial tensile specimen dimensions

Heckers Limiting Dome Height (LDH) tests on 200 mm x 200 mm laser welded blanks. Three dimensional DIC was also performed to assess strain development during forming. Figure 3.7 shows the data processing and analysis flow of the forming procedure. CCD cameras mounted towards the plane of the laser welded blank captured images of the blank for strain analysis while a load cell in the dome tester monitored the force exerted during deformation. A multi-channel synchronizing unit matched time signatures of the images with the load cell data. Strain data was post-processed using DIC software (VIC-3D 7) to evaluate minor and minor strain profiles. Image capture of the DIC system was conducted at a frequency of 125 Hz while step and subset sizes used for the analysis were fixed at 35 and 7, respectively. Bi-axial stretch forming was evaluated with a MTS 866 hydraulic press with a hemispherical punch having a diameter of 101.6 mm with a circular draw bead diameter of 132 mm. Several teflon sheets were used a lubrication between the blank the punch. A clamping force of 650 kN was exerted on the blanks to prevent draw in and the punch was advanced upwards at a rate of 0.2 mm/s until a significant load drop occurred on the hydraulic analog readout. All LDH results reported were averaged across five trials.

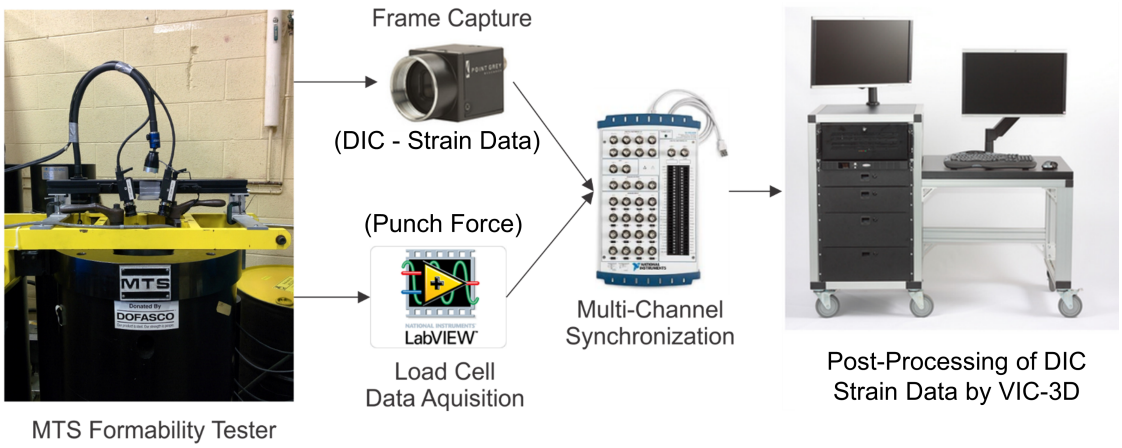

Figure 3.7: Illustration of the LDH strain and punch force data collection and processing steps for bi-axial stretch formability testing of fiber laser welded blanks.

3.7 Heat Treatment of Laser Welded Medium-Manganese Steel

The effects of heat treatment on laser welded MMn for the purpose of investigating potential for press hardening applications was investigated. Fiber laser welds were produced at a laser power of 4kW and a linear robot movement speed of 12 mmin^{-1} with a defocus distance of 5mm above the surface of the blank. The same specimen preparation procedure used in the previous section were applied to produce the laser welded MMn steel blanks.

Standard ASTM E8-13 sheet type tensile specimens were machined from the 200 mm x 200 mm steel blanks to investigate any effects associated with changes in specimen geometry. The dimensions for the tensile specimens are shown below in Figure 3.8. Tensile testing was conducted using an Instron tensile frame at a constant cross head speed of 10 mmmin^{-1} together with a DIC system with an image capture of at 4-6 Hz. Constant strain rate tensile testing was also conducted at strain rates of 0.1, 0.01 and 0.001 s^{-1} to identify any observable dependency of the mechanical properties on the strain rate.

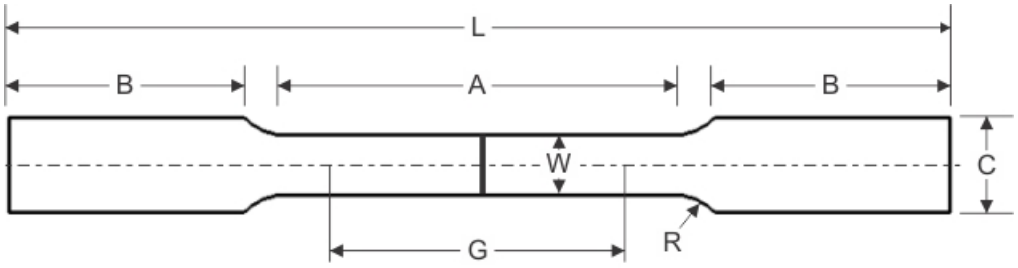

Label	G	W	R	L	A	B	C
Dimension (mm)	50	12.5	12.5	200	57	50	20

Figure 3.8: Standard size uni-axial tensile specimen dimensions

Heat treatment was performed in a baffle furnace at a heating rate of 2 ^{o} Cs^{-1} followed by a quenching sequence to simulate an industrial press hardening thermal cycle (Figure 3.9). Metallographic cross sections were taken of the welded specimens after heat treating and prepared using the aforementioned procedure. Microhardness testing was conducted on the etched cross sections for select specimens. Phase fractions were averaged across 3 XRD patterns per location for each heat treatment temperature.

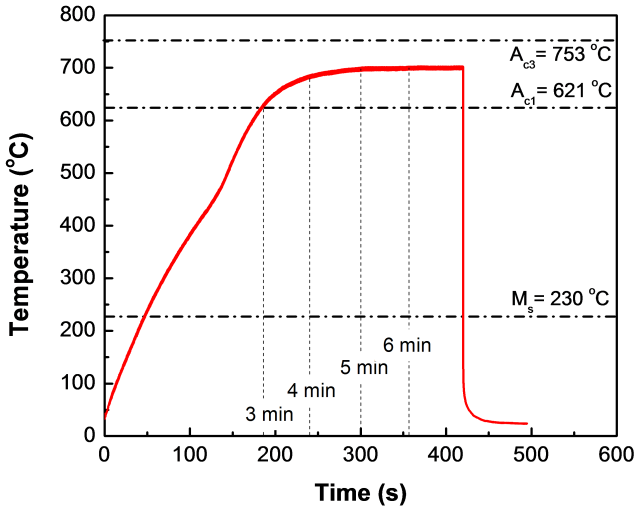

Figure 3.9: Heat treatment thermal cycle

Chapter 4

Microstructure Evolution of Laser Welded Medium-Manganese Steel

The objective of the chapter was to investigate the microstructural features resulting from the exposure to a non-isothermal traveling heat source. A diode laser was traced from one end of a clamped steel blank to another while thermocouples attached at various depths on the underside of the blank took *in situ* measurements of the temperature profile during the welding process. The information gained from this chapter will be used to further inform and contrast the behavior of the material when exposed to a higher energy density fiber laser used to produce production style laser welded blanks in the following chapter.

4.1 Thermal Cycle

In the FZ where complete melting is expected, re-distribution of alloying elements occurs in the liquid phase, driven by convective Marangoni fluid flow patterns within the weld pool [69]. In the HAZ, the steel remains solid and re-distribution must occur as a solid state diffusive process. At temperatures above A_3, the steel is expected to rapidly transform into γ, encouraging movement of solute atoms and dislocations throughout the matrix. Normally, during isothermal heating processes, the rate at which specific elements distribute within the matrix is governed by their respective diffusion coefficients. However, during rapid, non-equilibrium heating processes, the time for solute atoms diffuse is severely limited. In the case of laser welding, the heat source is both confined and moving rapidly across the surface of the substrate, resulting in a highly localized area of elevated temperature.

This causes a large thermal gradient in the specimen thickness resulting in different peak temperatures and time at temperatures. The short heating time combined with the rapid cooling due to conductive heat transfer to the base metal results in a thermal cycle with a sharp heating peak and a lengthy cooling tail characteristic of most welding process.

In Figure 4.1, the thermal cycles obtained by the diode laser welding trials show that the peak temperature obtained at a depth of 1.2 mm from the backside of the plate was the highest as the placement of the thermocouple is closest to the FB. As the laser traveled the length of the sample, the peak temperature experienced by each thermocouple decreased corresponding to their placement depth.

Another critical aspect of the microstructure formation of steel is the time-at-temperature. During heating of the steel, the time at temperature and the respective cooling rate within the various zones of the steel contribute to determining the resultant microstructure. The temperature regimes of particular interest include temperatures above the A_3, and the regime between A_3 and A_1. The A_3 and A_1 temperatures for the MMnS was calculated by Equations 2.1 and 2.2 to be 753 °C and 621 °C respectively. Compared to conventional C-Mn-Si steels, both critical temperatures are significantly lower primarily due to the high concentration of Mn in the steel as reported in Chapter 2.

After the peak temperature is achieved, the steel begins to cool rapidly. This dynamic cooling rate makes for difficult comparison to equilibrium continuous cooling transformation diagrams (CCT) studied by various scholars. In literature, Yi *et al.* showed that a martensitic transformation would occur for cooling rates anywhere between 0.1 °C/s and 100 °C/s [51]. The suppression of the α and α_B noses in the CCT is largely by in part due to the increased Mn content in the steel. As discussed earlier, Mn is an effective solid solution hardening element in steels which contributes to the stabilization of γ. However, the M_s is reduced significantly to approximately 203 °C which implies an even lower M_f. Therefore, even at peak temperatures above A_3, the HAZ should contain a large fraction of room temperature stable γ.

4.2 Microstructure

Figure 4.2 presents the SEM micrographs of microstructures obtained at the thermocouple placement locations. Figure 4.2(b) corresponds to a depth of 0.3 mm into the sheet thickness. The microstructure appears to have lost the ultra-fine lamellar structure observed in the BM. At this location, the peak temperature was slightly above the A_3 temperature, therefore prompting the growth of more globular type γ. The identification of α_B and α'

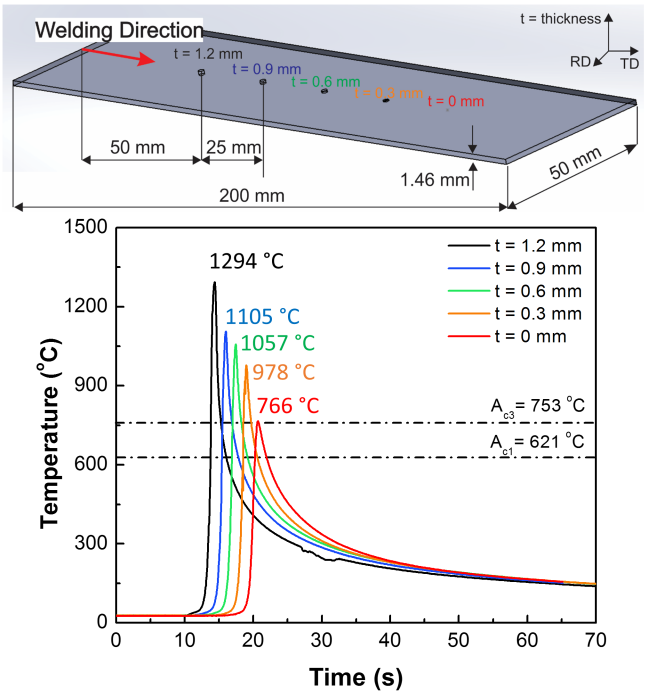

Figure 4.1: Thermal cycle profile obtained at various depths within the steel specimen along the center line during laser welding

could not be distinguished under the SEM. In Figure 4.2(c), the increase in peak temperature leads to a shift toward more lath-like γ. As the peak temperature increases closer to the FB of the weld Figures 4.2(c-d), more lath-type martensite becomes visible and finer carbides can be seen within the martensitic structures. This suggests that the peak temperature of the steel is a significant driving force for the microstructural evolution of the steel. At higher temperatures above A_3, a rapid transformation can occur to transform the pre-existing γ into α'.

Figure 4.3(a) presents an etched cross section of the BoP diode laser welded MMn steel. The overview of the welded cross section shows a significant variation in microstructure and provides insight into the microstructures associated with the rapid heating and cooling of the diode laser weld. Figure 4.3(b) is a micrograph of the as-received BM steel which appears to be unaffected by the laser. Figure 4.3(c-d) indicate that the conductive heat transfer from the weld pool likely produces a slight change in microstructure as evident

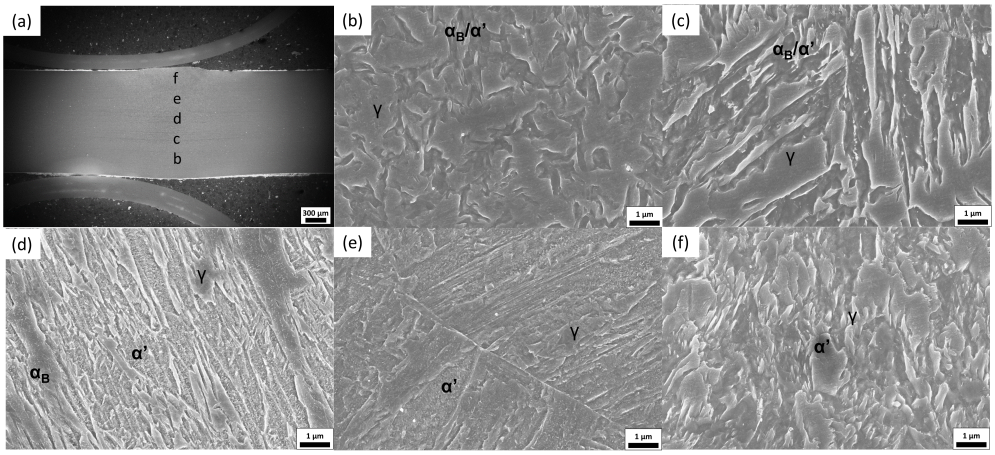

Figure 4.2: SEM micrographs of the microstructures corresponding to the thermocouple placement depths of (a) diode laser weld cross section overview, (b) 0.3 mm, (c), 0.6 mm, (d) 0.9 mm, (e) 1.2 mm and (f) FZ

by a 'dark band' appearing on either side of the weld zone. Figure 4.3(e) shows that the microstructure between the weld pool and the dark band consists of a of small grains which are delineated by polygonal PAGBs. In the area adjacent to the FB (Figure 4.3(f)), the presence of large prior austenite grains are observed and large martensite blocks and bainite sheaths can be seen. Some large white streaks were observed to be unaffected despite the exposure to high temperatures. This suggests that the streaks could possibly by high temperature stable δ-ferrite which could have formed during the rolling and heat treatment process. Figure 4.3(g) shows that the FZ consists mostly of bainite sheaves, lathy martensite and film-like austenite. The preferential growth of the solidification dendrites from the FB towards the center of the weld pool can be observed clearly from the macroscopic overview in Figure 4.3(a).

Provided that the microstructure observed in the optical microscope were extremely fine, higher magnification SEM micrographs were taken of the respective zones of interest. Figure 4.5(a) shows the high magnification microstructure of the BM consists of ultra-fine lamellar colonies of alternating laths of ferrite (α_{L}) and austenite (γ_{L}). Regions of globular ferrite (α_{G}) and austenite (γ_{G}) also exist. As mentioned earlier in Chapter 2, the presence of the duplex α and γ are the result of stabilization of the austenite by partitioning of the C and Mn. An EDS line scan of the lamellar microstructure (Figure 4.4) shows that the relative composition of C and Mn in the α and γ differed considerably, confirming the findings in literature.

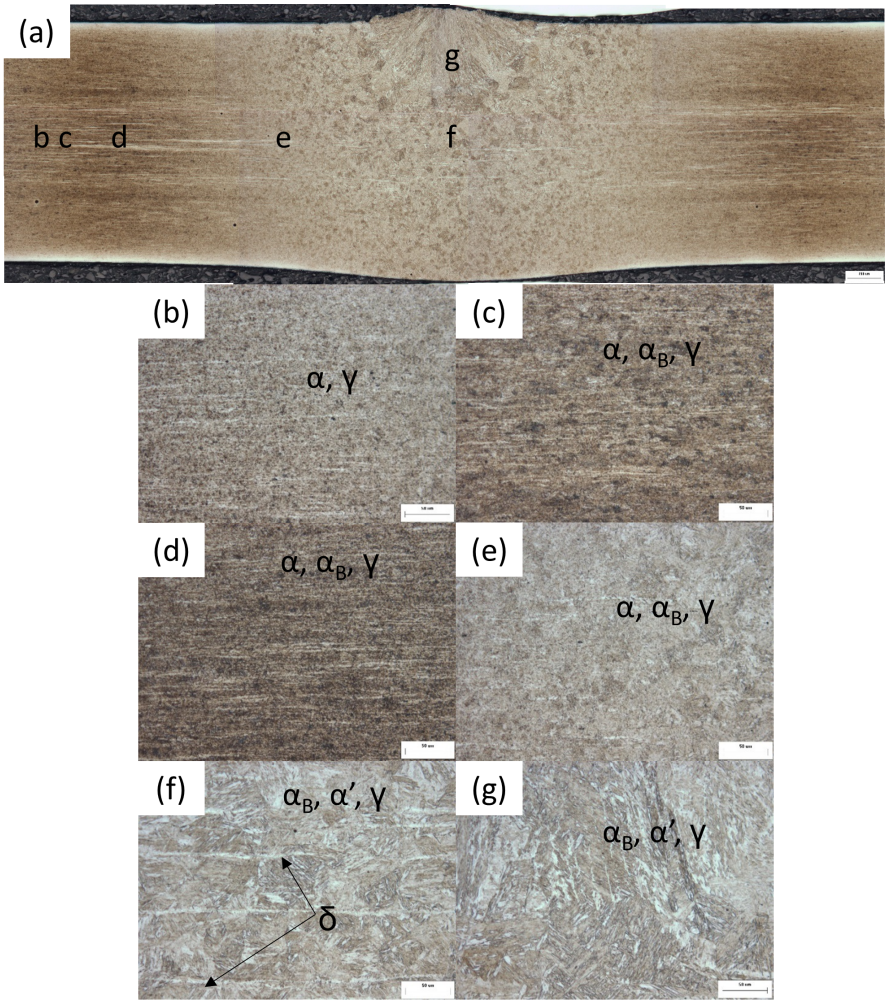

Figure 4.3: Optical microscopy images of diode laser welded medium-Mn steel; (a) Overview, (b) BM, (c-f) HAZ, (g) FZ; (α-ferrite, α_B-bainite (grey), α'-martensite (off white), δ-delta-ferrite (streaks), γ-austenite (white))

The microstructure in the dark band observed in Figure 4.5(b) shows that the well defined lamellar structure of the BM had decomposed slightly. According to Podder and Bhadeshia, the destabilization of the γ, which leads to the decomposition into α + cementite (θ), is highly dependent on the peak temperature experienced by the steel over a period of time [70]. During laser welding, the heating time is extremely rapid, therefore complete homogenization will not be achieved given the limited time at elevated temperature. Fig-

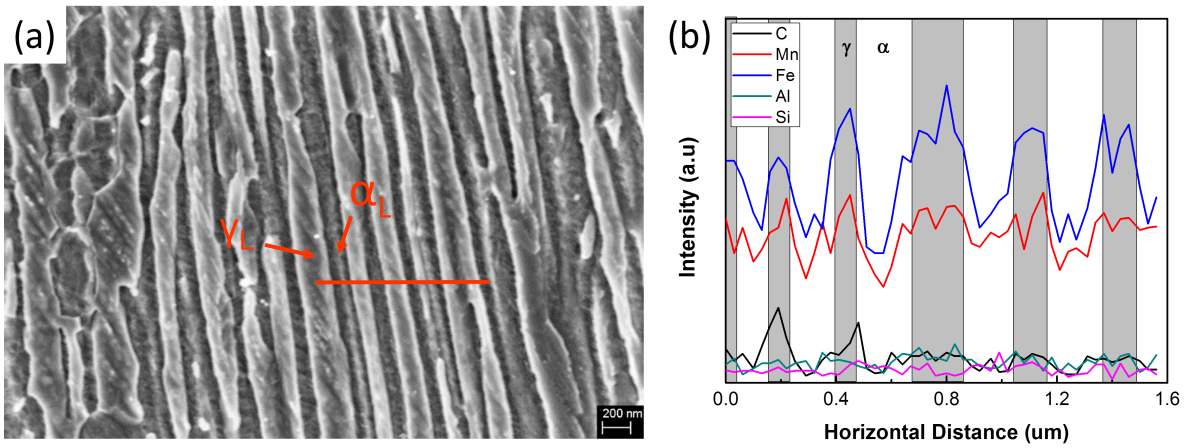

Figure 4.4: EDS line scan of the BM microstructure in the medium-Mn steel; (a) SEM micrograph and (b) EDS line scan results

ure 4.5(c) shows the microstructure in the HAZ between the dark band and the FZ of the laser weld. The high angle grain boundaries which are characteristic of PAGBs are clearly visible (dashed lines) and new α' packets, suggest that the temperature experienced by this region of the steel exceeded the A_3 temperature. Evidence of some θ formation dispersed throughout the matrix indicate the nucleation of some carbides. The presence of γ cannot be readily distinguished between the lathy α' and α_B in this microstructure. Considering that the steel has been re-austenitized, it is possible that some newly formed γ could be stabilized during heating through the two phase region. Figure 4.5(d) shows the micrograph of the HAZ where the δ-ferrite band was observed. From the micrograph, it is visible that some intermediate structures are visible within the δ-ferrite band itself. Figure 4.5(e) reveals the micrograph of the steel at the FB (dashed line). The lath α' in the FZ shows strong directional growth from the polygonal grains in the HAZ adjacent to the FB. Furthermore, Figure 4.5(f) show the regions of interdendritic segregation which separate the primary austenite solidification dendrite cores.

Both Figure 4.3(g) and Figure 4.5(f) indicate that the FZ of the diode laser welded MMn steel exhibits a degree of columnar dendritic solidification. Similar FZ microstructures have been observed in laser welds of both 1st and 2nd generation AHSS. In conventional 1st generation AHSS, TRIP steels containing high concentrations of Al were observed to exhibit preferential dendrite growth that favoured the formation of skeletal δ-ferrite [71]. According to Xia *et al.* [71], a diode laser welded Fe-2Mn-1.73Al-0.15C steel

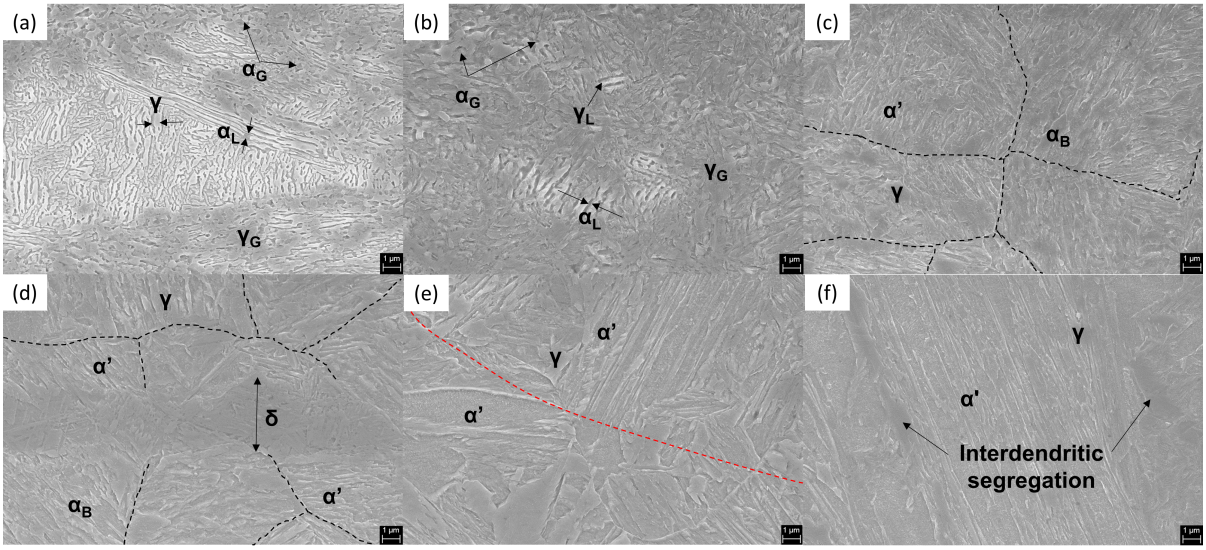

Figure 4.5: SEM micrographs of various zones within diode laser welded medium-Mn steel; (a) BM, (b) dark band HAZ, (c-d) coarse grain HAZ, (e) FB, (f) FZ; (α_G-globular ferrite, α_L-lathy ferrite, γ_G-globular austenite, γ_L-lathy austenite, α'-martensite, α_B-bainite, δ-delta-ferrite)

the presence of skeletal δ-ferrite is a by-product the peritectic reaction stemming from the solidification pathway: $L \rightarrow \delta + L \rightarrow \delta + \gamma \rightarrow \delta + \alpha' + \alpha_B$. Under equilibrium conditions, the molten steel should have fully solidified as δ prior to the formation of γ. Given the highly non-equilibrium conditions during laser welding, the rapid solidification results in the rejection of C and Mn into the interdendritic region [71]. Consequently, the remaining liquid becomes enriched with solute and solidifies as γ, which then transforms into α' and α_B. It should be noted that the FZ microstructure in the interdendritic regions containing lath α' and α_B were found to exhibit thin films of γ_{RA} between ferrite laths. In 2nd generation AHSS, laser welds of a Fe-18.8Mn-0.45Si-0.63C TWIP steel showed significant microsegregation of C and Mn despite the dendritic austenite solidification mode [47]. The laser weld seams exhibited long columnar austenite grains extending from the FB towards the centerline where the difference in the C and Mn concentration between the dendrite core and the interdendritic region could be as large as 0.24 wt%and 6.26 wt% respectively [47]. Provided the high initial concentration of C and Mn, the FZ was able to remain fully austenitic after solidification.

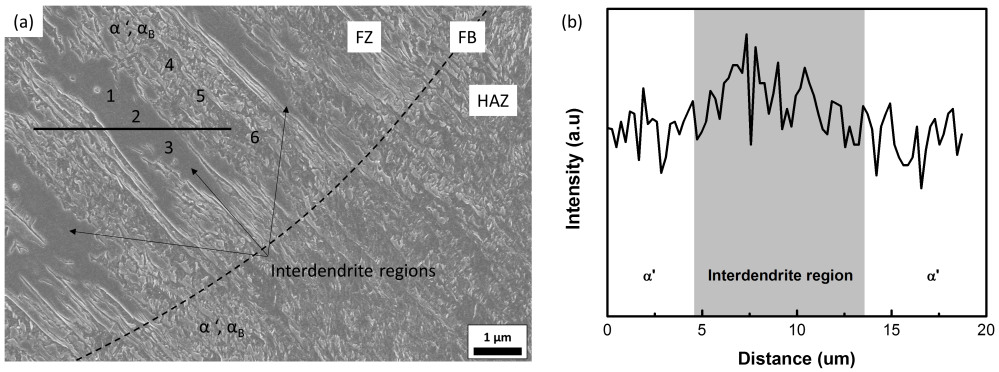

Figure 4.6: Microsegregation of Mn in the FZ of diode laser welded MMn steel; (a) SEM micrograph of the FB region of a laser weld cross section and (b) EDS line scan profile taken across the an inter-dendritic region

Several competing processes are at play when assessing the solidification behaviour of laser welded MMn steel. First, the propensity for the steel to preferentially form skeletal δ-ferrite is limited by the higher Mn concentration in MMn steel compared to conventional TRIP steel. Secondly, the C and Mn concentration in MMn steel is insufficient to maintain a fully austenitic microstructure in the FZ after laser welding. Thirdly, the enrichment of the liquid phase with C and Mn during solidification causes a corresponding depletion in the dendrite cores. Figure 4.6(a) reveals the microstructure observed at the FB of the laser welded MMn steel showing evidence of columnar dendrities containing α' or α_B separated by regular intervals of a darker unetched phase. The EDS line scan in Figure 4.6(b) shows that the inter-dendritic region contains an elevated concentration of Mn. Figure 4.7 indicates that inter-dendritic region contains approximately 2.58 wt% more Mn compared to the dendrite core. The microstructure can be explained by the reduced Mn in the dendrite cores, which result in a lower transformation barrier to α' compared to the liquid material. There is reason to believe that the natural solute microsegregation may result in a stable room temperature γ in the interdendritic regions of the FZ.

4.3 Microhardness

Figure 4.8 presents the horizontal microhardness profile of the diode laser welded MMn steel. The BM of the steel exhibits a hardness value of 366 $\pm$ 3 HV. The high hardness in

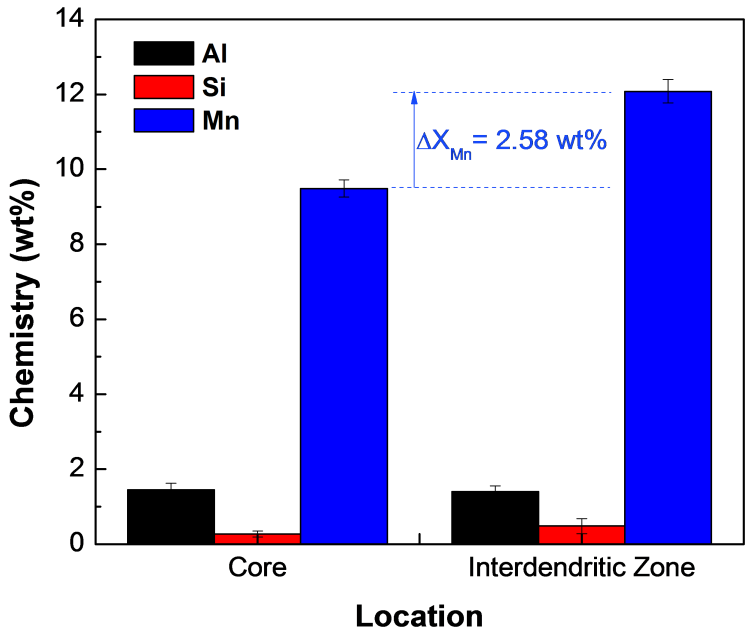

Figure 4.7: Chemical composition of solute elements in the dendrite cores and the interdendritic zones

the BM can be partly attributed to the UFG size. The total HAZ width is approximately 1 mm wide on either size of the FZ and the steel does not show evidence of softening, primarily due to the absence of pre-existing martensite [28, 72]. Since no softening is observed when welding with the diode laser, welding with a lower heat input fiber laser will likely not induce any softening behaviour either. The hardness adjacent to the FZ is similar to that of the FZ hardness. The FZ hardness of the steel was determined to be 449 $\pm$ 9 HV supporting the observation that α' or α_B was present.

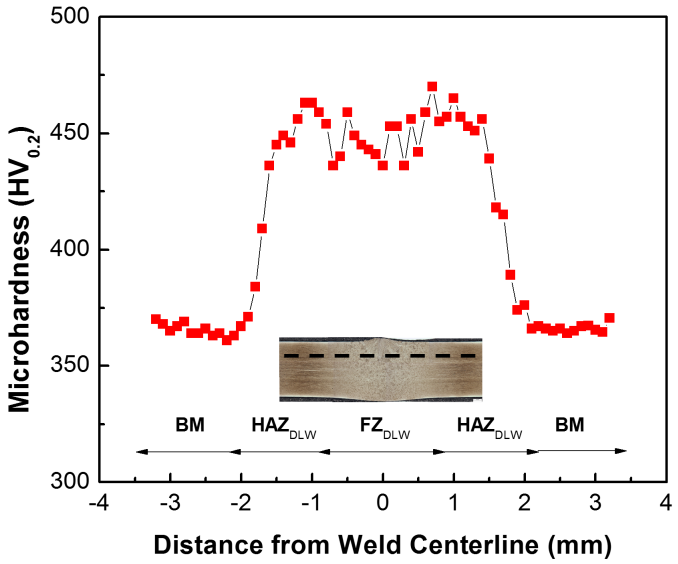

Figure 4.8: Microhardness profile of diode laser welded MMn steel

4.4 Summary

Diode laser BoP welds were made on MMn steel to investigate the effects of laser welding on microstructural evolution. Thermocouples were installed at various depths along the backside of the steel blank to measure the thermal cycle during laser welding.

The ultra-fine lamellar structure of the BM MMn steel was observed to be fairly stable at high temperatures. Exposure to temperatures above A_3 resulted in a shift towards increasing amounts of α'.

At temperatures below A_3, the microhardness profile indicates that the MMn steel is not prone to HAZ softening despite having a very high BM hardness. The reason for this is that the BM does not contain any pre-existing α' nor does the microstructure appear to be susceptible to grain growth like other high-Mn steels.

Solidification of the FZ was columnar dendritic in nature and evidence of microsegregation was observed between the dendrite cores. During the cooling process, the dendrite cores transformed into martensite likely due to the rejection of C and Mn into the inter-dendritic spaces. The resultant morphology of the inter-dendrite spaces appear to be pockets of stable γ.

Chapter 5

Mechanical Property and Microstructure Correlation of Laser Welded Medium-Manganese Steel

The focus of this chapter is to assess the fiber laser weldability and mechanical properties of as-received MMn steel with respect to dissimilar combinations of HSLA and DP980 steel which are commonly used first generation AHSS. Microstructure characterization, microhardness, tensile properties and cold formability were assessed to evaluate the correlation between observed microstructure and joint performance.

5.1 Microstructure

Figure 5.1(a) shows the cross-section overview of a MMn-MMn weld. The FZ microstructure as illustrated in Figure 5.1(b) consists primarily of lath α', however, the original dendrite solidification structure decorated is still visible. Darker regions between dendrite cores suggests the occurrence of C and Mn microsegregation phenomena during solidification, which has been observed in welds of high-Mn AHSS and diode laser welds in the previous chapter [73, 74, 55]. The enrichment of the inter-dendrite regions can suppress the formation of α' and thereby result in stable γ [33]. However, unlike high-Mn AHSS, the Mn content in MMn steels appears to be insufficient to produce a fully austenitic FZ microstructure after laser welding. In Figure 5.1(c), the microstructure of the HAZ consists of a dense network-like structure of α and γ compared to the distinct lamellar structure

observed in the BM (Figure 5.1(d)). The microstructures observed across the HAZ are not distinct enough to qualitatively distinguish between specific temperature zones.

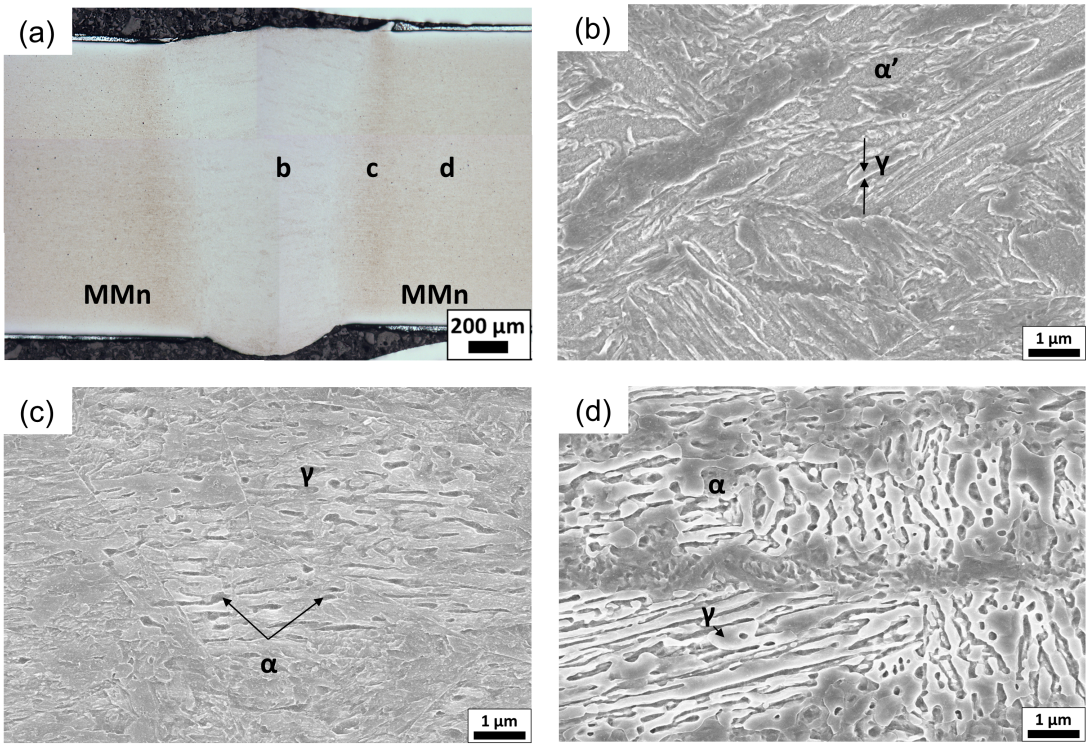

Figure 5.1: SEM micrographs of MMn-MMn laser weld cross section; (a) full weld profile, (b) FZ, (c) HAZ, (d) MMn BM(γ: austenite, α: ferrite, α': martensite).

Figure 5.2(a) illustrates the different regions in the MMn-HSLA laser welded specimens. The FZ of the MMn-HSLA laser weld (Figure 5.2(b)) appears to consist primarily of martensite formed upon rapid cooling of the weld pool. Austenite in the FZ can not be determined by qualitative observations of the SEM micrographs. This can be attributed to the FZ mixing between the low alloy content in the HSLA and the higher alloy content in the MMn steel. The super-critical region in the HSLA steel (Figure 5.2(c)) adjacent to the FZ consists of lath α', and the inter-critical HAZ of the HSLA side (Figure 5.2(d)) reveals nucleation of block α' between α grains. Both of which, are typical HAZ microstructures observed in laser welded HSLA steel [75].

Figure 5.3(a) shows the cross section of the MMn-DP980 laser weld along with the microstructural evolution across the respective regions. The micrographs of the MMn-DP980 welds are consistent with typical microstructures observed in laser welded DP steel

found in literature [75, 28]. The FZ displays α', while the presence of γ is indiscernible (Figure 5.3(b)). Similarly to the MMn-HSLA welds, the dilution of the Mn in the FZ contributes to reducing austenite stability, effectively preventing dendritic solidification. The super-critical HAZ (Figure 5.3(c)) contains well defined α' blocks with large high angle grain boundaries delineating the PAGBs. The inter-critical HAZ (ICAHAZ) (Figure 5.3(d)) contains a continuous network of newly transformed α' and α. The sub-critical HAZ (SCHAZ) exhibits pre-existing α' that was tempered by exposure to temperatures slightly below A_1 (Figure 5.3(e)) [72].

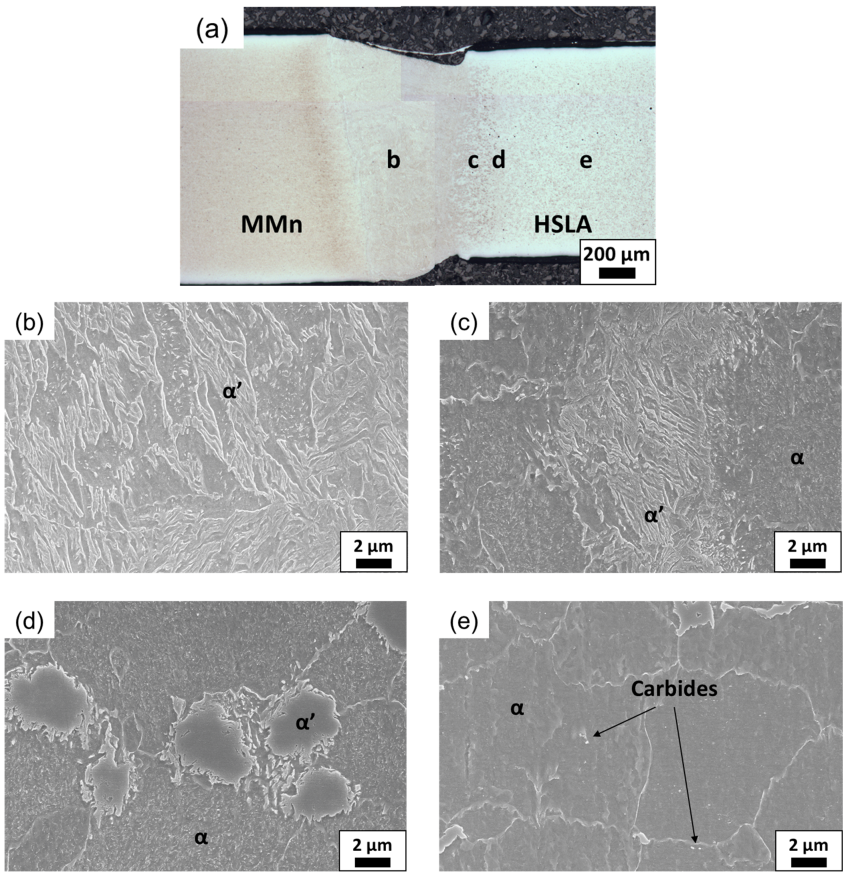

Figure 5.2: Micrographs of MMn-HSLA laser weld cross section;(a) full weld profile, (b) FZ, (c) supercritical HAZ, (d) intercritical HAZ, and (e) HSLA BM (α: Ferrite, α': Martensite).

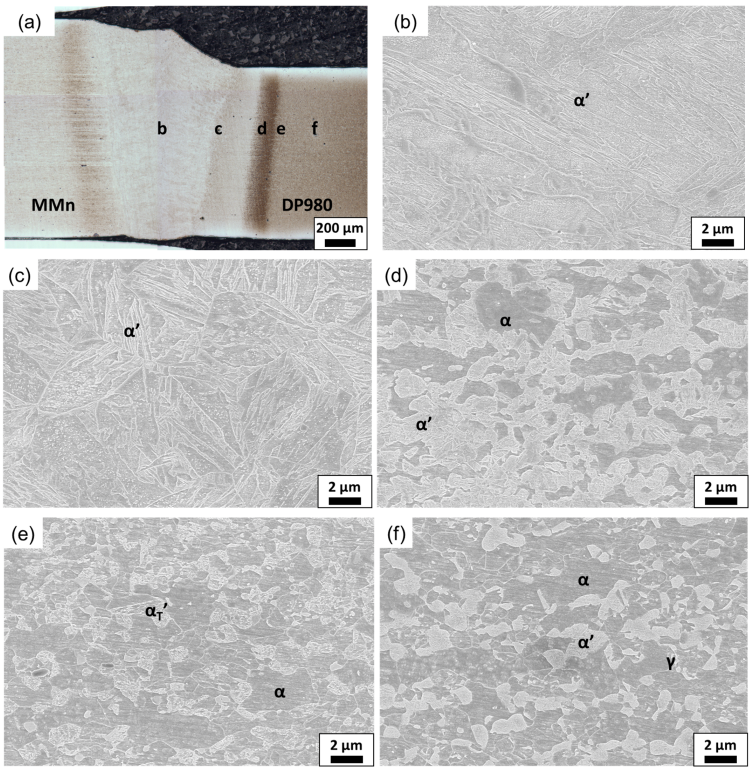

Figure 5.3: Micrograph of MMn-DP980 laser weld cross section. (a) full weld profile, (b) FZ, and HAZ on the DP980 side showing (c) super-critical HAZ, (d) ICHAZ, (e) SCHAZ, (f) DP980 BM. (γ: Austenite, α: Ferrite, α': Martensite, α_T': Tempered Martensite).

5.2 X-Ray Diffraction

XRD was performed on the FZ, HAZ and BM of the three different laser welded joints. Figure 5.4(a) illustrates the characteristic 2θ peaks associated with α and γ in the BM, HAZ and FZ of the similar MMn-MMn steel laser welded joint. The γ volume fraction in the BM, HAZ and FZ is determined to be approximately 50.2 %, 41.4 % and 28.0 % respectively. The large volume fraction of γ in the BM is consistent with the ultra-fine lamellar microstructure observed in the SEM micrographs of Figure 3.1(a). The XRD results also confirm that the laser interaction with the MMn steel destabilizes some of the γ, triggering a solid-state transformation in the HAZ which causes a decrease in the γ volume fraction compared to the BM. The large volume fraction decrease in the FZ coincides with the presence of lath α' observed from the SEM micrographs. This can be

attributed to the rapid solidification of the molten metal in the weld pool. However, the FZ was found to contain a significant amount of γ, which suggests that the Mn content in the steel is sufficient to prevent some of the γ from transforming into α' upon cooling. Compared to Figure 5.4(b) and 5.4(c), where the γ peaks are absent from the BM and HAZ of the HSLA and DP980 steels, the FZ of the dissimilar joints appear to contain a considerable volume fraction of γ. Figure 5.4(d) graphically illustrates the effect of mixing dissimilar chemistry on the resultant γ volume fraction within the FZ of the laser weld.

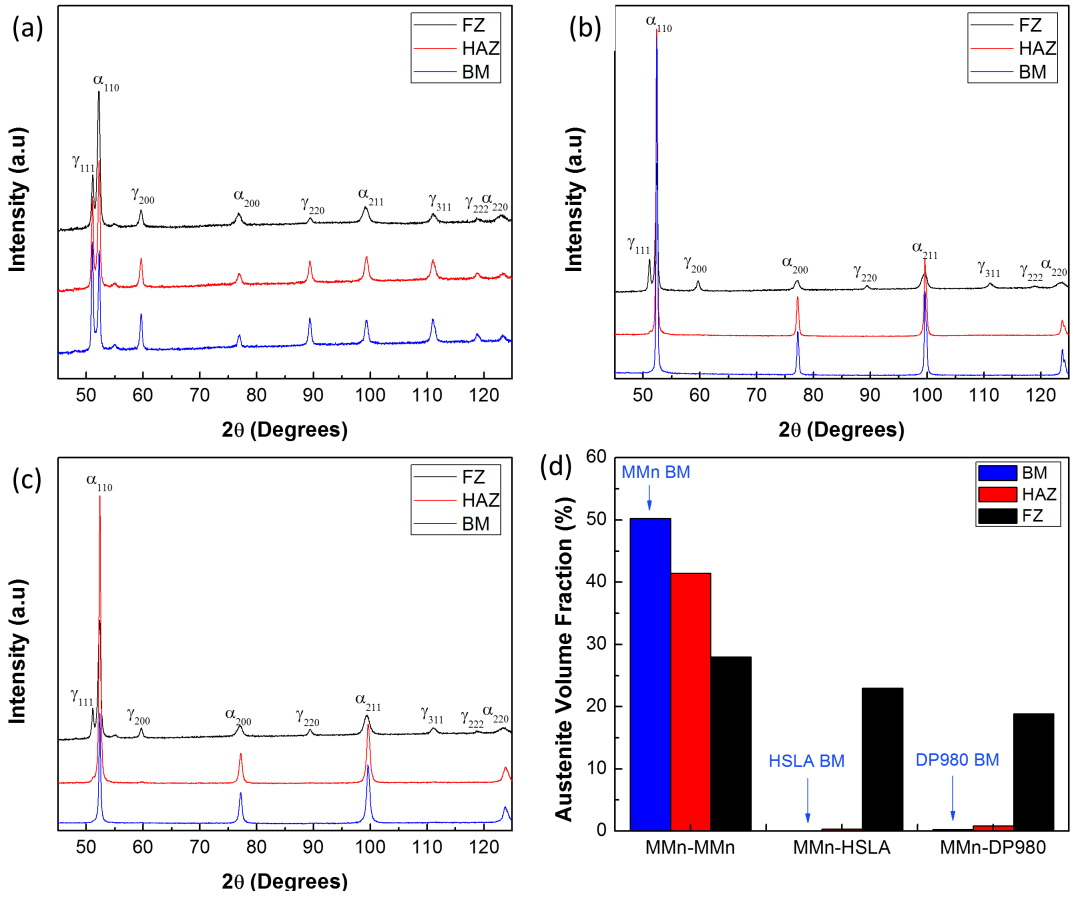

Figure 5.4: XRD pattern for the FZ, HAZ and BM of the (a) MMn-MMn, (b) MMn-HSLA and (c) MMn-DP980 laser welded joints

5.3 Microhardness

Figure 5.5 shows the microhardness profiles on cross sections of MMn-MMn, MMn-HSLA and MMn-DP980 welds. The microhardness of the MMn BM is determined to be 396 ± 10 HV. Although the majority of the microstructure consisted of α and γ (Figure 3.1(a)), the ultra-fine lamellar structure of γ resulted in a high BM hardness value. The MMn-MMn microhardness profile reveals no HAZ softening, as predicted in Chapter 4, which can be attributed to the lack of α' in the BM. The super-critical HAZ of the welded joint exhibits the highest hardness values of approximately 463 HV and can be attributed to the formation of α' at the rapid cooling rates experienced by the steel adjacent to the FZ. The effects of rapid local thermal cycles on the microstructural stability of MMn steel are not fully understood in literature. However, the ultra-fine lamellar duplex microstructure of the γ appears to avoid significant grain coarsening observed in high-Mn steels during short exposure time at elevated temperatures present in the laser weld HAZ [47]. Both diode laser and fiber laser welding have shown that rapid heating of MMn steel has little effect on the microstructure in the HAZ at temperatures below A_3. The FZ of the weld exhibits an average hardness of 421 ± 16 HV, which is slightly higher than the BM hardness (396 ± 10 HV) due to the presence of α' in the FZ. The HSLA steel (Figure 3.1(b)) is found to be significantly softer (155 ± 9 HV) due to large polygonal α grains which offer less resistance to the applied load during hardness testing. The hardness profile of the HSLA steel gradually increases when approaching the FZ of the weld, which can be attributed to the nucleation of α' at the α grain boundaries caused by the rapid thermal cycle during laser welding [75, 76]. The FZ of the MMn-HSLA weld had an average hardness of 413 ± 13 HV. The hardness of the FZ was lower than that of the MMn-MMn FZ, which is likely a result of the reduced C and Mn content caused by mixing of the two different steel chemistries. The microhardness of the DP980 steel BM (Figure 3.1c) is measured to be 343 ± 8 HV; a slight reduction in SCHAZ hardness (315HV) on the DP980 side of the joint was observed which is due to the tempering of pre-existing martensite [75, 28]. The martensitic FZ of the MMn-DP980 weld had an average hardness of 438 ± 11 HV, which is higher than the FZ of the MMn-MMn weld. The findings agree with the reduced amount of γ found in the MMn-DP980 FZ compared to the MMn-MMn weld as determined by XRD.

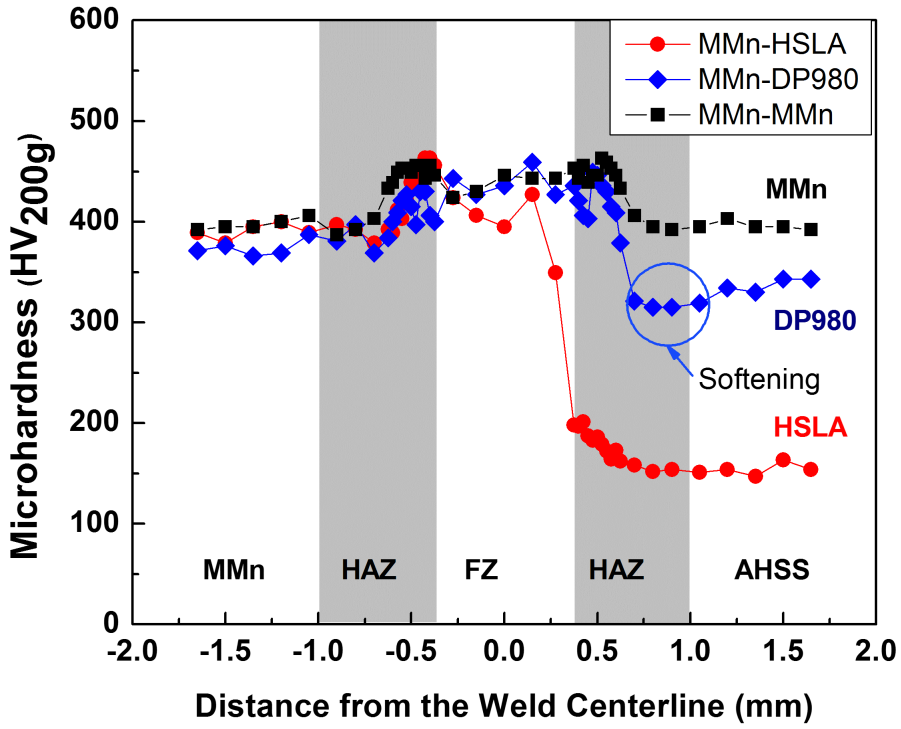

Figure 5.5: Microhardness profiles of laser welded MMn steel to HSLA and DP980 steels

5.4 Tensile Testing

Figure 5.6 presents the representative BM engineering stress versus strain curves of MMn, HSLA, and DP980 steel while Table 5.1 summaries the mechanical properties. The MMn steel exhibits upper and lower yield strengths (σ_{YS}) of 995 MPa and 966 MPa, respectively (inset of Figure 5.6(a)). A large yield point elongation of approximately 10% was detected as a result of Lüders band formation [58, 77, 78, 79]. This behaviour is consistent with the tensile curves in literature of MMn steels, which suggest a pronounced MMn effect [80, 24, 67, 56, 81]. Unlike traditional first generation TRIP steels where the TRIP effect is stress induced, the transformation induced plasticity in MMn steels is largely influenced by a the local plastic strain front initiated by the movement of Lüders bands [78]. Lee *et al.* [82] studied the velocity at which the Lüders bands travel across the gauge length of MMn steels and determined that the subsequent movement results in significant strain-dependent transformation of the austenite into ϵ-martensite. The ultimate tensile strength (σ_{UTS}) and ϵ_{Total} of the MMn steel is determined to be 1126 MPa and 32%, respectively. Therefore,

the tensile strength and ductility product is calculated to be 36,032 MPa% which aligns with the target mechanical properties for a third generation AHSS [79]. The HSLA steel exhibits lower σ_{YS}, σ_{UTS}, and ϵ_{Total} of 428 MPa, 453 MPa and 32.3%, respectively. The DP980 steel is determined to have a σ_{YS}, σ_{UTS}, and ϵ_{Total} of 651 MPa, 998 MPa, and 14.7%, respectively.

Table 5.1: Tensile mechanical properties of steels used

Steel	σ_{YS} *(MPa)*	σ_{UTS} *(MPa)*	ϵ_{YPE} *(%)*	ϵ_{Total} *(%)*	σ_{UTS} x ϵ_{Total} *(MPa%)*
MMn	966 ± 4	1126 ± 12	9.9	32.0 ± 2.4	36,032
HSLA	428 ± 15	453 ± 19	8.6	32.3 ± 1.6	14,632
DP980	651 ± 6	998 ± 6		14.7 ± 0.1	14,671

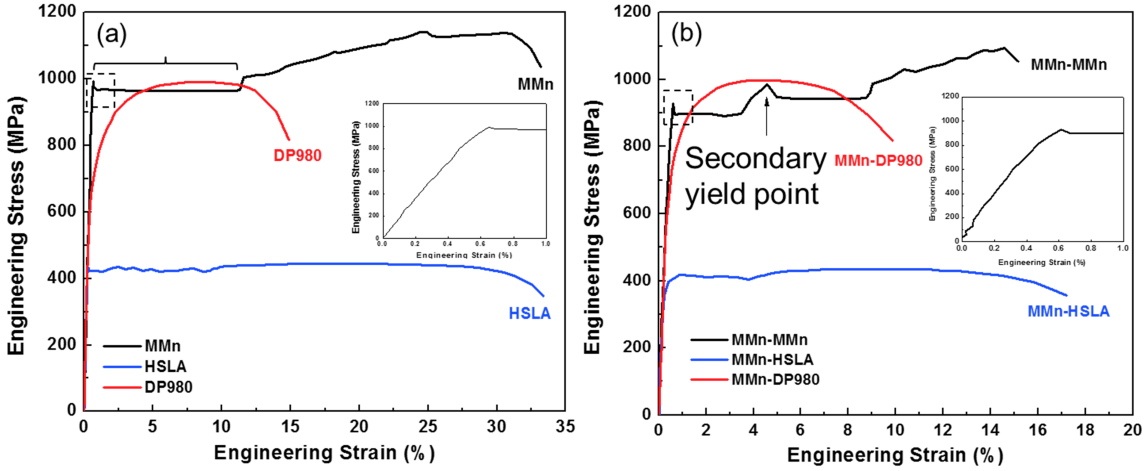

Figure 5.6: Representative engineering stress versus strain curves of (a) BM and (b) laser welded joints tested at a constant cross head travel speed of 10 mm min^{-1}. The bracket in (a) delineates the yield point elongation region of the MMn BM whereas the arrow in (b) indicates the secondary yield point that occurs in the MMn-MMn laser welded specimens

The engineering stress-strain curves of laser welded blanks consisting of MMn-MMn, MMn-HSLA and MMn-DP980 are presented in Figure 5.6(b) and the mechanical properties are summarized in Table 5.2. From the tensile tests, the MMn-MMn weld had a σ_{YS}, σ_{UTS}, and ϵ_{Total} of 897 MPa, 1091 MPa, and 16.2%, respectively. The joint efficiency of the weld, determined as the ratio between the σ_{UTS} of the welded joint and the MMn steel, was 95.9%. Comparatively, the tensile strength of the joint appeares to achieve desirable

values; however, the ϵ_{Total} is significantly lower than the BM. The MMn-MMn weld shows a significant decrease in ductility as fracture occurred after the yield point elongation. It was observed that the beginning of the yield point elongation marks the entrance of the Lüders band front into the reduced section of the specimen. As it travels across the gauge length, the band front encounters the FZ that mainly consists of hard α', resulting in the impediment of the plastic deformation front. As a result, the engineering stress increases to a secondary upper yield point (marked with vertical arrow in Figure 5.6(b)). Before fracture occurs, the Lüders band front initiates on the other side of the weld bead and continues towards the other end of the gauge length. This phenomena results in the reduction of the gauge width across the entire gauge length of the tensile specimen. After the Lüders band exits the gauge length, subsequent work hardening occurs. Therefore, the secondary yield point phenomenon in the engineering stress-strain curve can be attributed to the effect of the non-uniform microstructure imposed by the laser weld, which causes significant strain concentration on either side of the weld bead resulting in fracture (Figure 5.7) as will be explained in a later section.

Table 5.2: Mechanical properties of laser welded joints

Steel	$\sigma_{\mathbf{YS}}$ *(MPa)*	$\sigma_{\mathbf{UTS}}$ *(MPa)*	$\epsilon_{\mathbf{Total}}$ *(%)*	**Joint Efficiency** *(%)*	$\sigma_{\mathbf{UTS}}$ **x** $\epsilon_{\mathbf{Total}}$ *(MPa%)*
MMn-MMn	897 ± 3	1091 ± 1	16.2 ± 0.6	95.9	17,722
MMn-HSLA	414 ± 8	442 ± 6	17.1 ± 0.3	97.6	7,560
MMn-DP980	602 ± 6	1005 ± 9	9.3 ± 0.3	∼100	9,310

The tensile curve of the MMn-HSLA welded specimen behaves similarly to that of the HSLA steel BM as the welded joint failed in the HSLA side. Nominal σ_{YS}, σ_{UTS}, and ϵ_{Total} achieved by the MMn-HSLA welded specimen were determined to be 414 MPa, 442 MPa, and 17.1%, respectively. Provided that the σ_{YS} and the σ_{UTS} of the welded joint was similar to that of the weaker HSLA steel, it is reasonable to suggest that most of the deformation occurred in the HSLA steel BM, which is confirmed by final fracture in the HSLA steel BM (Figure 5.7). Given that the σ_{YS} of the MMn steel is significantly larger than the σ_{YS} of the HSLA, the HSLA steel begins to plastically deform before the MMn finishes elastically deforming. Therefore, the hard weld FZ microstructure becomes an anchor point and effectively reduces the gauge length of the specimen, resulting in an overall decrease in perceived ϵ_{Total}. The laser welded MMn-HSLA specimen achieved a joint efficiency of 97.9% with respect to the HSLA steel. The tensile response of the MMn-DP980 welded specimen indicated deformation behaviour akin to the BM of DP980 due to the higher yield strength of the MMn BM. The σ_{YS}, σ_{UTS}, and ϵ_{Total} achieved by

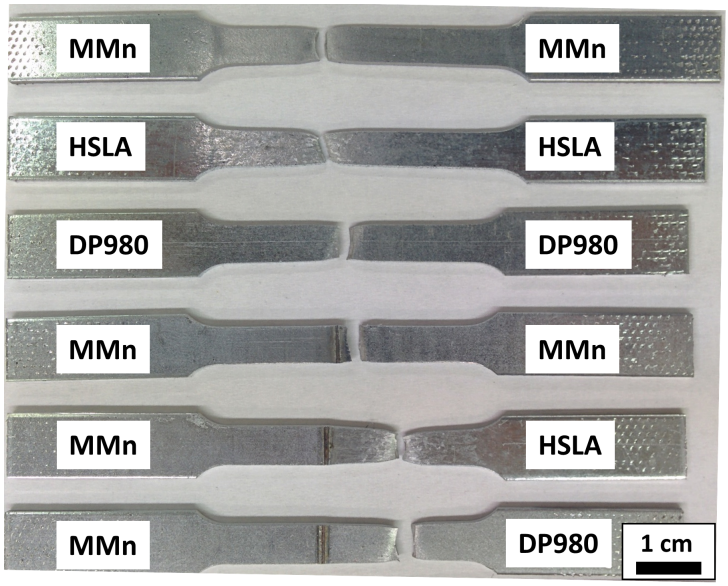

Figure 5.7: Typical tensile failure locations for BM and laser welded joints

the MMn-DP980 welded specimen were determined to be 602 MPa, 1005 MPa, and 9.3%, respectively. The joint efficiency was determined to be about 100% when considering the weaker DP980 BM as the basis for comparison. The reduction in ductility of the welded specimen can be attributed to the fact that deformation occurs in the DP980 prior to the onset of yielding in the MMn steel. Despite the small reduction in hardness in the SCHAZ of the DP980 steel as shown previously, the softened zone is not significant enough to reduce the mechanical properties and induce an elevated stress concentration region. Ultimately, fracture of the welded specimen occurs in the BM of the DP980 steel (Figure 5.7).

Figure 5.8 shows the development of local axial strain along the gauge length of the welded specimens at various stages of deformation during tensile loading. Figure 5.8(a) represents the plastic strain development in MMn-MMn welded specimens. The shape of the strain profile is clearly bimodal, showing evidence of a decrease in strain in the FZ region. Figure 5.8(b) and Figure 5.8(c) illustrate the strain development in the MMn-HSLA and MMn-DP980 laser welded specimens, respectively. In contrast to the MMn-MMn specimen, the strain concentration occurs only on the weaker materials i.e., at the HSLA side for MMn-HSLA joint and DP980 side for MMn-DP980 joint. As discussed earlier, the degree of HAZ softening in the MMn-DP980 weld was small and had a negligible effect on the weld performance. Figure 5.8(c), vividly shows that the majority of the strain

was concentrated approximately 7 mm away from the weld centerline, whereas SCHAZ is about 0.6 mm away from the FZ, confirming that HAZ softening is not detrimental for this particular steel chemistry combination.

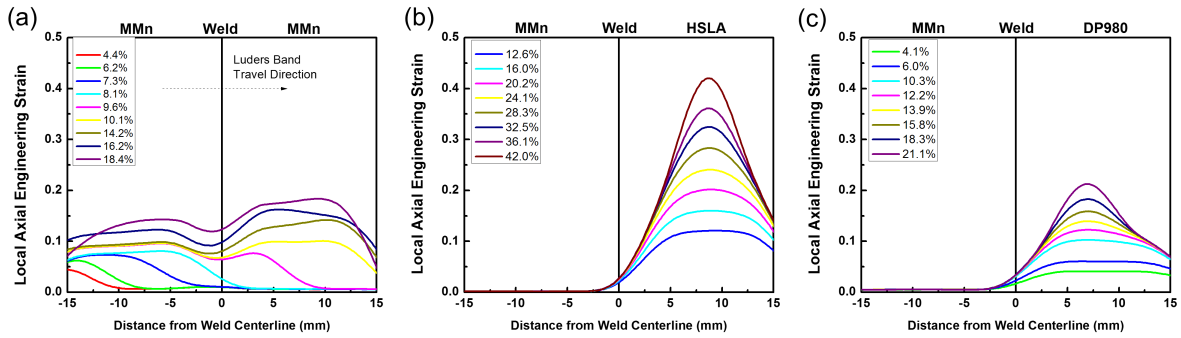

Figure 5.8: Axial strain development along the gauge length of the tensile specimen at various time steps during uniaxial tensile testing of the (a) MMn-MMn, (b) MMn-HSLA and (c) MMn-DP980 laser welded specimens

Figure 5.9 illustrates the progression of local axial engineering strain across the gauge length of the MMn-MMn laser welded tensile specimen. The strain profile clearly shows that as the Lüders band propagates from one end of the gauge length, it raises the local strain by approximately 7% (position 2). Ryu *et al.* [78] reported that the localized deformation front is responsible for austenite to martensite strain induced transformation for a Fe-5.6Mn-0.055C-2.2Al-0.49Si wt% alloy steel. As a result, a large axial strain differential occurs in front Lüders band which is also accompanied by a corresponding cross section area reduction where the band sweeps through the gauge length. Other research groups analyzed the microstructure before and after the local plastic deformation front and found a significant reduction in γ volume fraction [83]. However, as the front reaches the FZ, it is arrested by the hard, α' microstructure present in the weld bead (position 3). This results in a local decrease in axial engineering strain as the α' does not plastically deform to the same degree as the BM microstructure. Therefore, the secondary yield point phenomenon noticed in Figure 5.6(b) is a direct result of the Lüders band front impediment by the laser weld FZ. If the specimens do not fail in the FZ, a secondary Lüders band front initiates on the other side of the weld (position 4). The secondary band front results in a bimodal strain distribution on either side of the weld. When the Lüders band exits the other end of the gauge length (position 5), plastic strain begins to accumulate in the region adjacent to the FZ due to the large local difference. Consequently, localized strain concentration initiates premature fracture under tensile loading (position 6).

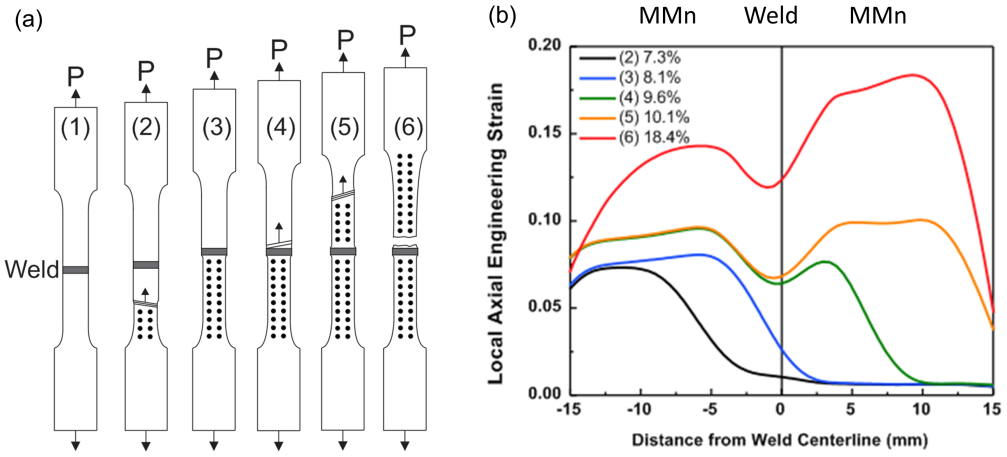

Figure 5.9: Schematic illustration of the (a) MMn-MMn laser welded tensile specimen loaded under uniaxial tensile strain and the (b) corresponding local axial engineering strain profiles present at various stages

5.5 Formability

Figure 5.10 and Figure 5.11 illustrate the strain profiles and LDH values obtained by biaxial stretch forming the BM and laser welded blanks. Given the monolithic nature of the BM steels, the strain profiles are largely parabolic in nature with the majority of the strain localized near the center of the punch. According to Figure 5.10(a), the MMn steel has a wider and more distributed strain profile compared to both the HSLA (Figure 5.10(b)) and DP980 (Figure 5.10(c)) steels. The HSLA steel appears to favour multiple strain localization areas whereas the strain in the DP980 steel is concentrated at the center. The LDH values obtained for the MMn, HSLA, and DP980 steels were 34.0 $\pm$ 0.6 mm, 35.6 $\pm$ 1.6 mm, and 30.8 $\pm$ 1.8 mm, respectively. Figure 5.10(d) illustrates the strain profile of the MMn-MMn laser welded blank. The blank immediately fractured along the FZ centerline upon punch contact at a maximum LDH value of 1.9 $\pm$ 1.1 mm, suggesting that laser welds of the MMn steel are extremely brittle when subjected to out of plane loading. The MMn-HSLA specimen (Figure 5.10(e)) achieved an average LDH value of 15.7 $\pm$ 1.7 mm. The strain profile transverse to the weld line indicated a disproportionate plastic strain occurring approximately 5 mm towards the HSLA side of the specimen. Fracture of the specimen was first observed to occur transverse to the weld line approximately 15 mm from the punch center. Figure 5.10(f) shows the representative strain profile obtained by the MMn-DP980 specimen. The maximum true strain achieved by the MMn-DP980

combination was lower than the MMn-HSLA specimen but higher than the MMn-MMn specimen. Comparatively, the strain distribution ratio between the DP980 and MMn sides of the blank was significantly closer than the MMn-HSLA specimens. This can be attributed to the smaller difference in σ_{YS} of the two base metals. The LDH value achieved by the MMn-DP980 combination was observed to be 11.1 $\pm$ 1.7 mm. Fracture of the MMn-DP980 laser welded blank generally initiated transverse to the weld line and eventually progressed to a crack parallel to the weld. This suggests that the effects of HAZ softening were still present during out-of-plane deformation and must be taken into consideration when forming laser welded blanks using DP980 steel.

5.6 Summary

Fiber laser welded blanks of MMn steel were produced by welding to HSLA and DP980 steel. The microstructure and mechanical performance of the similar and dissimilar welds were analyzed.

Similar laser welds of MMn steel were observed of exhibit FZ that consisted primarily of α' and a small amount of γ. The columnar dendrite solidification mode was still visible. The dissimilar welds to HSLA and DP980 produced mostly martensitic FZ due to mixing of the low alloy content chemistry with the MMn steel.

HAZ softening was not observed in fiber laser welds due to a stable high temperature microstructure. The HAZ in fiber laser welds were significantly narrower than the lower energy dense diode laser welds.

Tensile testing of sub-size specimens of MMn-MMn joints achieved roughly 96%. The effects associated with the Lüders band movement through the specimen gauge length and the interaction with the FZ was analyzed. Dissimilar welds failed in the weaker HSLA and DP980 steels due to lower strength compared to the MMn steel.

Cold formability of MMn similar welds was severely limited due to the brittle nature of the FZ under biaxial stretch forming. Forming of the dissimilar LWBs improved the ductility significantly by moving the stress localization point towards the weaker AHSS.

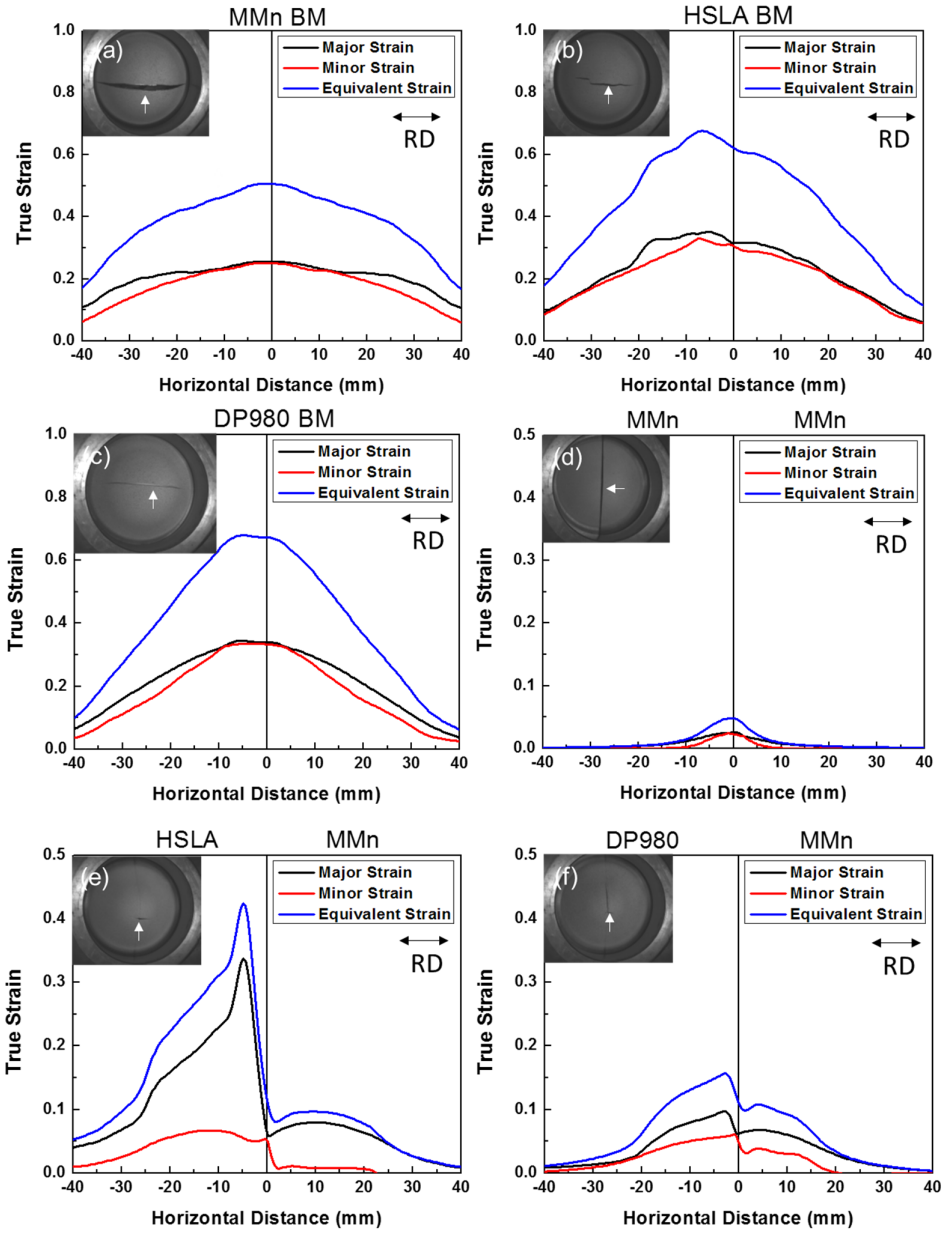

Figure 5.10: Strain profiles parallel to the rolling direction of base metal and laser welded blanks under biaxial stretch forming. (a) MMn BM, (b) HSLA BM, (c) DP980 BM (d) MMn-MMn, (e) MMn-HSLA, (f) MMn-DP980. (White arrow in the inset indicates initial fracture location on the laser welded blanks)

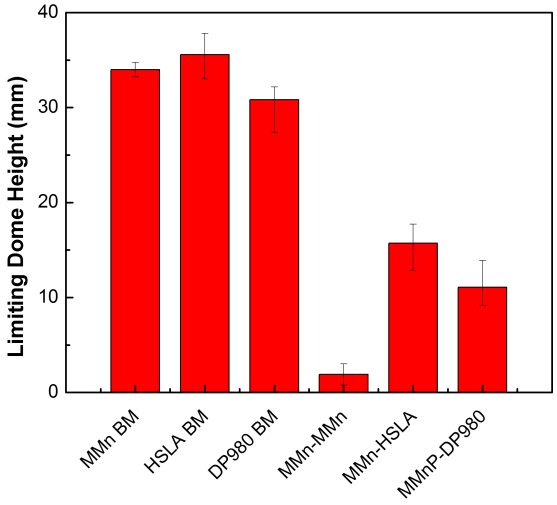

Figure 5.11: LDH values of biaxial stretch formed BM and laser welded steel blank combinations

Chapter 6

Heat Treatment of Laser Welded Medium-Manganese Steel Blanks

In this chapter, laser welded blanks of MMn steels were heat treated to investigate the viability of their usage as a potential steel for press hardening applications. Conventional press hardening steels (PHS) used in the automotive industry are typically C-Mn-Si steels with a small amount of boron as a hardenability agent [84, 85, 86]. Although boron steels can exhibit high strength (σ_{UTS} = 1.5 - 2 GPa), the ductility of the steel decreases proportionally with the increasing addition of carbon and boron interstitial solute elements. During high impact events, energy absorption is a key factor in determining the energy dissipation and intrusion resistance of the structural member. Steels with low ductility have a tendency of fail suddenly once the tensile strength is surpassed, whereas a steel with higher ductility will be capable of absorbing more energy.

6.1 Heat Treatment

MMn steels have shown some potential as a new class of PHS in several recent studies. First, the increased Mn concentration in the steel reduces the A_3 temperature considerably. This ensures that a full austenization treatment could be performed at a lower temperature and a shorter period of time compared to conventional boron steels. Rana *et al.* performed hot forming of a Fe-9.76Mn-0.15C-1.37Al-0.19Si (mass%) steel at temperatures of 650, 700, 750 and 800 $^{\circ}\mathrm{Cs}^{-1}$ for 3 minutes followed by quenching. Tensile specimens of the press hardened steel showed that the BM could obtain σ_{UTS} = 1619 MPa and ϵ_{T} = 16.5 %,

indicating significant promise as a PHS solution. Secondly, the increased Mn concentration in the steel increases the hardenability of the steel such that critical cooling rate can be sufficiently suppressed. Han *et al.* demonstrated that the α_B noses can be completely avoided for a range of cooling rates between 0.1 - 100 $^oCs^{-1}$ [87]. After press hardening, the steel was found to exhibit $\sigma_{UTS} = 1791$ MPa and $\epsilon_T = 10.4$ %. Thirdly, the heightened concentration of Mn reduces the M_f temperature of the steel such that γ_{RA} can exist after press hardening. Electron backscatter diffraction (EBSD) analysis of a press hardened MMn steel exhibited approximately 12 vol% γ_{RA} [87]. Yi *et al.* reported that a partitioning step after press hardening a MMn steel containing Fe-(5-8)Mn-(0.2-0.4)C-(0.7-2.5)Si could also dramatically increase the ductility of the steel. Mechanical properties of the MMn steel tempered at 250 ^{o}C for 30 minutes after die quenching were $\sigma_{UTS} = 1883$ MPa and $\epsilon_T = 15.9$ % [51]. It was observed that the tempering step at 250 ^{o}C to initiate C and Mn partitioning after the die quench could increase the γ vol% up to 15.1% [51].

LWBs of PHS are an attractive method of achieving weight reductions by combining high strength PHS steel with strategic material placement. During press hardening, the FZ of the material, which is initially martensitic, is heat treated to the γ single phase region with the rest of the steel blank. Upon die quenching, the joint achieves a homogeneous microstructure with the BM. No studies to date have been conducted on the viability of MMn steel as a potential solution for press hardened LWB.

6.1.1 Effect of Heat Treatment Temperature

A range of heat treatment temperatures were selected such that the effects of temperature on the BM and FZ could be analyzed. Heat treating at temperatures of 650, 700, 750, 800, 850 ^{o}C allowed for assessment of the microstructural evolution across the inter-critical (between A_1 and A_3) and super-critical regimes ($>A_3$).

Figure 6.1 reveals the BM microstructure of the MMn steel after heat treatment and quenching for various furnace temperatures. Figure 6.1(a) shows the BM microstructure as a comparison. Figure 6.1(b) indicates that heat treatment at 650 ^{o}C shows a slight coarsening of the α laths in some locations. 650 ^{o}C is slightly above the inter-critical temperature for the MMn steel. The findings in Chapter 3 and 4 have shown that the MMn steel is remarkably stable after exposure to high temperature at short interaction times. Figure 6.1(c) reveals a small fraction of α' dispersed with in the α and γ phases in the BM after heat treatment at 700 ^{o}C. Some dissociation of the γ can also be observed resulting from the exposure to a higher inter-critical temperature. Figure 6.1(d) indicates the presence of more α' present in the BM heat treated at 750 ^{o}C. The conversion of

more pre-exisitng α to γ followed by rapid quenching results in the formation of more α'. The presence of carbide particles observed in the BM could be a result γ destabilization in the BM. The loss of the characteristic lamellar structure in the BM reinforces the fact that the steel BM reached a temperature close to the A_3 critical boundary. Figure 6.1(e) shows the microstructure of the MMn heat treated at 800 °C consists of more α', smaller globular γ grains and θ particles. After crossing the A_3 critical temperature, the diffusionless transformation from $\gamma \rightarrow \alpha$' martensite begins to govern a larger fraction of the microstructure. Figure 6.1(f) shows even larger volume fraction conversion to α' after heat treatment to 850 °C. This indicates that the peak temperature during heat treatment has a significant effect on the final microstructure of the steel.

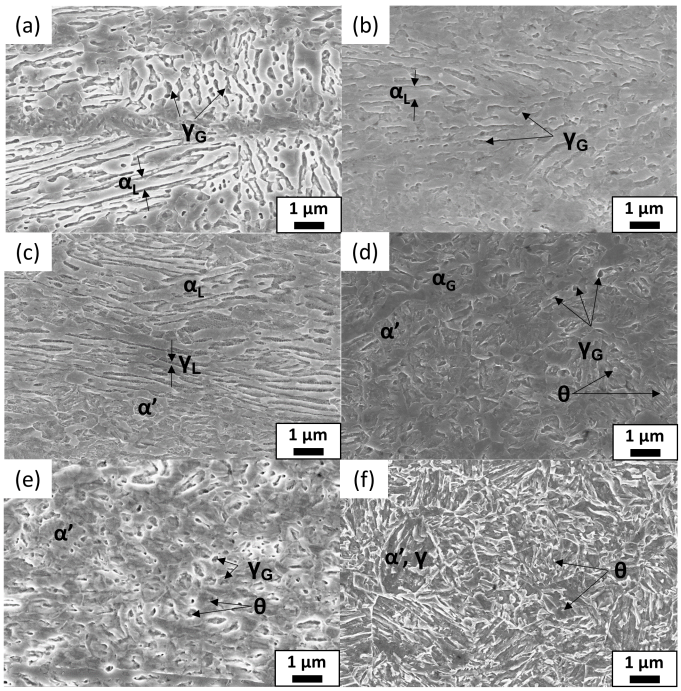

Figure 6.1: SEM micrographs of the BM after heat treatment for 3 mins followed by quenching for various furnace temperatures: (a) AR, (b) 650 °C, (c) 700 °C, (d) 750 °C, (e) 800 °C, (f) 850 °C

Figure 6.2(a) shows the typical microstructures observed in laser welds of as-received MMn steel consist of α' formed after rapid solidification and stabilized γ as a result of the Mn content in the steel. After heat treatment at 650 °C, the FZ microstructure shown in Figure 6.2(b) shows evidence of initial α' $\rightarrow \gamma$ reverse transformation. The presence of

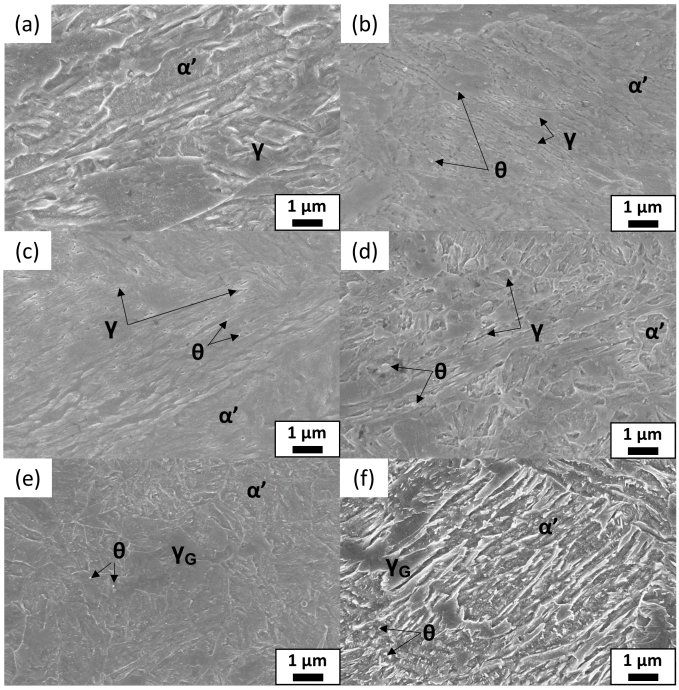

Figure 6.2: SEM micrographs of the FZ after heat treatment for 3 mins followed by water quenching for various furnace temperatures: (a) AR, (b) 650 °C, (c) 700 °C, (d) 750 °C, (e) 800 °C, (f) 850 °C

θ particles and the formation of γ along α' lath boundaries indicate the initial stages of lamellar growth. As the furnace temperature was increased to 700 °C, the microstructure of the FZ appeared to homogenize slightly and the lamellar structure appeared to be more pronounced in certain locations. Figure 6.2(d) shows that the presence of lathy α' becomes more pronounced. Figure 6.2(e-d) show that the nucleation of more θ particles and the conversion to more lath α' with γ taking form of globular grains rather than laths. The findings are consistent with the observations made by Gibbs *et al.* that higher annealing temperatures destabilize enriched γ [88].

Microhardness profiles (Figure 6.3) of the heat treated joints corroborate the observations of the microstructure. The hardness of the as-received MMn BM and FZ was determined to be 396 ± 10 HV and 413 ± 13 HV respectively. For the joint heat treated at 650 °C, the BM hardness remained relatively the same, but the FZ hardness was found to decrease significantly to 376 ± 11 HV. This effect can be attributed to the austenite reverse transformation which increases the amount of γ in the FZ. By increasing the heat

treatment temperature to 700 °C, The BM hardness appears to decrease significantly to 360 ± 7 HV and more of the α' transforms to γ in the FZ, reducing the hardness to 348 ± 7 HV. Heating the FZ to 700 °C appears to result in a more homogeneous microhardness profile. At 750 °C, a drastic change in microhardness occurs. The BM and FZ hardness increase to 436 ± 9 HV and 463 ± 7 HV respectively. This coincides with a heat treatment temperature close to the A_3 critical temperature of the steel. Up to this temperature it appears that the FZ steel has a tendency to retain the dual phased α' and γ structure after quenching. At 750 °C, the steel microstructure appears to become dominated by the transformation from $\gamma \rightarrow \alpha' + \alpha_B$. At 800 °C, the BM and FZ hardness values increase to 457 ± 10 HV and 473 ± 8 HV respectively. A further increase of soak temperature to 850 °C results in a small decrease in BM and FZ hardness values to 449 ± 14 HV and 457 ± 4 HV respectively. BM hardness value for the 850 °C soak temperature is within error of the MMn steel processed at 800 °C, but the FZ appears to show slight decease in hardness.

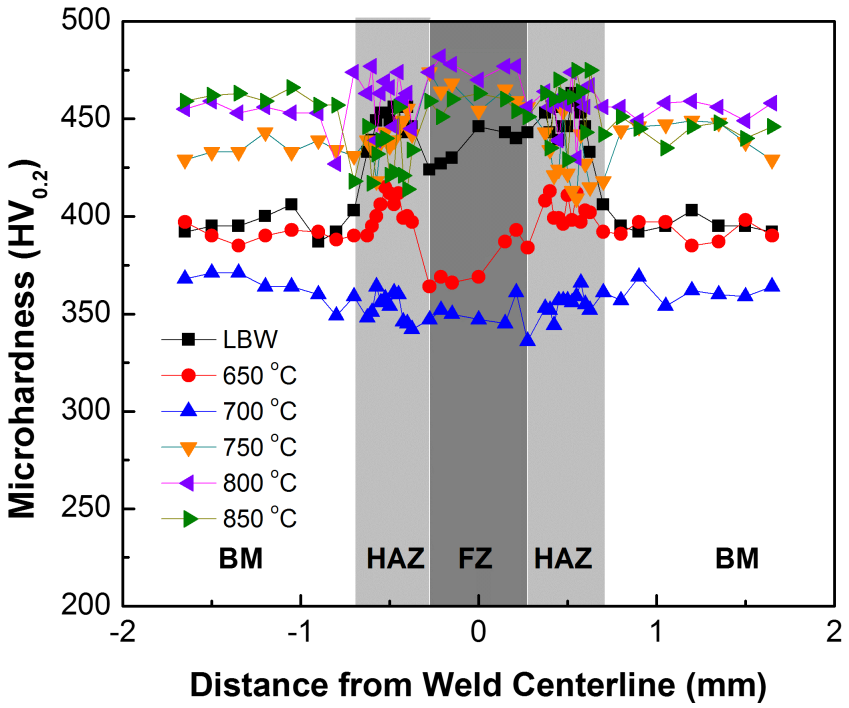

Figure 6.3: Microhardness profile of laser welded MMn steel joints after heat treatment at various temperatures for 3 min

The re-appearance of lamellar microstructure and the microhardness decrease in the FZ of the laser welded MMn steel joint heat treated at 700 °C for 3 minutes was of

particular interest. Figure 6.4(a) shows the cross section of the laser welded MMn steel joint after heat treatment at 700 °C for 3 minutes. The SEM micrograph shows that the BM microstructure (Figure 6.4(b)) retains most of the lamellar structure seen in the BM of the as-received steel. Evidence of α' dispersed between what appears to be γ grains indicate that the temperature was sufficient to austenize a portion of pre-existing α in the BM. At the inter-critical heat treatment temperature, it was expected the steel would consist of a mixture of α and γ in the furnace. Over a sufficient amount of time, the pre-existing γ would eventually begin to nucleate θ [89]. The FZ (Figure 6.4(c)) clearly shows distinct separation between the dendrites. Due to the re-solidification of the material, the FZ consists of a significant amount of α' within the dendrite cores. By exposing the α' in the FZ to inter-critical temperatures, the α' $\rightarrow \gamma$ reverse transformation is induced. The inter-dendritic regions enriched with γ stabilizing elements during solidification appear darker compared to the dendrite cores. The dendrite cores show the beginning formations of the ultra-fine lamellar structure as the austenite nucleates preferentially between the martensite laths and at θ particles. Further partitioning of C and Mn stabilizes the γ resulting in a mixed microstructure of α' and γ.

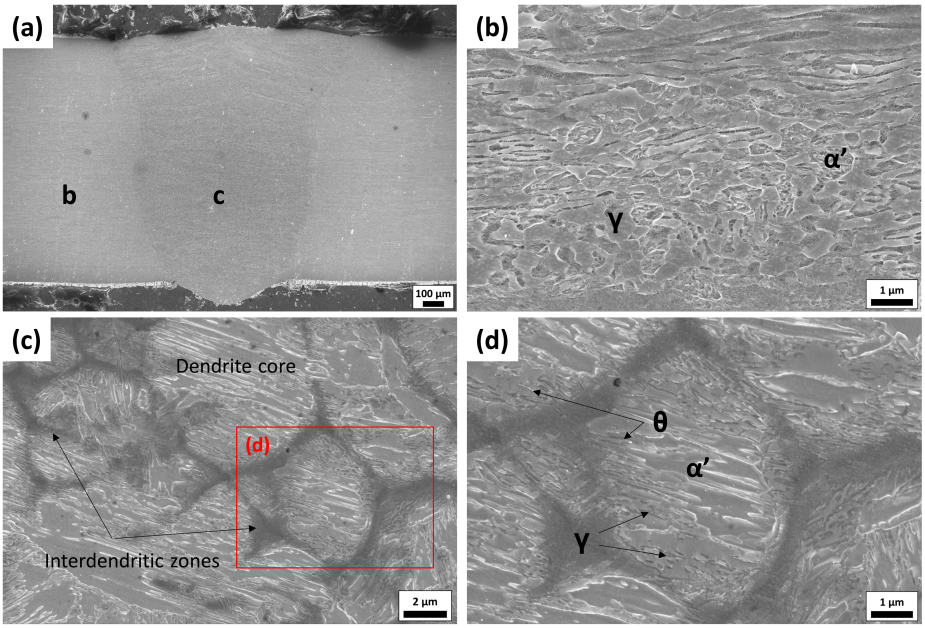

Figure 6.4: SEM micrograph cross section of laser welded MMn steel butt joint heat treated at 700 °C for 3 mins; (a) overall view, (b) BM, (c) FZ, (d) magnified inset view of FZ

6.1.2 Effect of Heat Treatment Time

To assess the effects of heat treatment time on the microhardness of the MMn steel BM and FZ, laser welded specimens were left in the furnace at elevated temperature ranging from 3-7 minutes. Figure 6.5 shows the microhardness values for the furnace temperatures between 650 - 800 °C. At a furnace temperature of 650 °C (Figure 6.5(a)), the BM microhardness increased slightly with respect to increasing soak time while the FZ microhardness was observed to decrease slightly. Previously, the BM microstructure processed at 650 °C appeared to be almost unaffected by the heat treatment and quenching when compared to the BM of the as-received material. However, the microstructure of the FZ at 650 °C contained a mixture of α', γ and θ which showed the beginnings of the austenite reverse transformation. An increase in annealing time at this temperature would permit the formation of more γ which could explain the decrease in FZ microhardness over time. At a furnace temperature of 700 °C (Figure 6.5(b)), both the BM and FZ decreased initially after exposure to elevated temperature at 3 minutes. With increasing soak time, the FZ material exhibited a slight increase in microhardness over the BM; nevertheless, remaining fairly similar. The decrease in microhardness over time could be explained by the microstructure observed in the 700 °C condition earlier, which showed a more distinct lamellar structure associated with the austenite reverse transformation. For a furnace temperature of 750 °C (Figure 6.5(c)), a rapid increase in microhardness of the BM and FZ was observed which then quickly leveled with increasing soak time. A similar trend was observed for furnace temperatures of 800 and 850 °C respectively (Figure 6.5(d,e)). This trend could be explained by exceeding the A_3 temperature enabling greater formation of new martensite upon rapid cooling. The rapid increase followed by a leveling off of the microhardness values with prolonged time suggests that potential press hardening applications do not require significant soaking times to achieve a desired microhardness value.

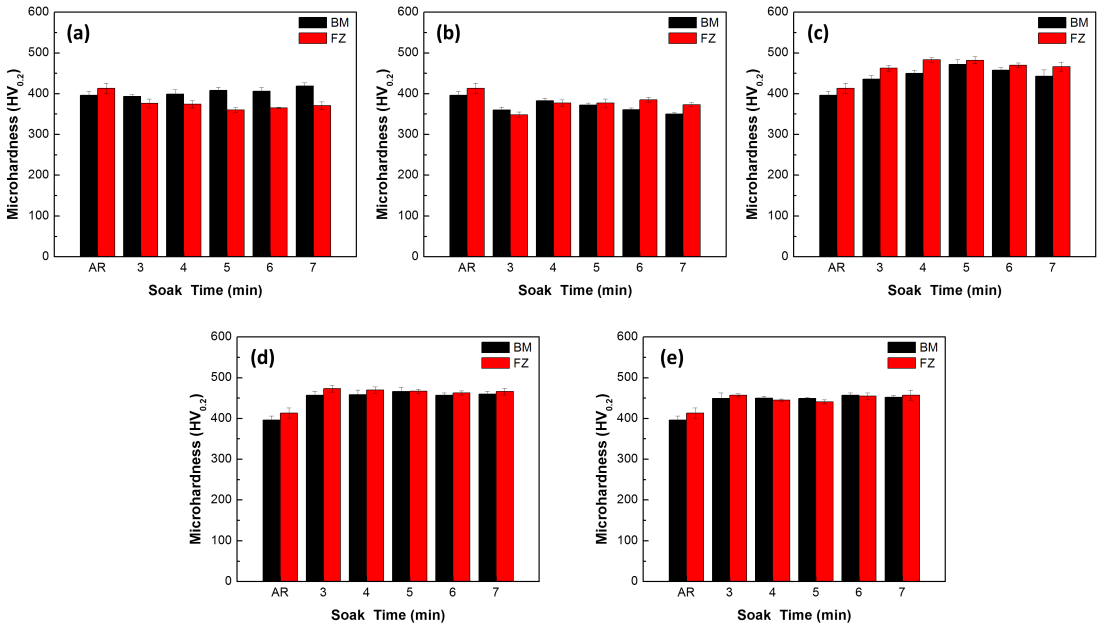

Figure 6.5: Microhardness values for BM and FZ of fiber laser welded MMn steel joints after heat treatment and water quenching; (a) 650 °C, (b) 700 °C, (c) 750 °C, (d) 800 °C, (e) 850°C

6.2 X-Ray Diffraction

Figure 6.6(a) and Figure 6.6(b) shows the XRD patterns for the heat treated BM and FZ of laser welded MMn steel. The prominence of the γ peak in the 650 °C and 700 °C patterns indicates the growth of the γ volume fraction in both the BM and FZ. Figure 6.7 clearly demonstrates that the growth in the γ volume fraction increases up to the 700 °C heat treatment condition, but immediately experiences a significant drop after heat treating at 750 °C. The γ volume growth can be explained by annealing at the inter-critical temperature in the $\alpha + \gamma$ region of the phase diagram. In the BM, continual grain growth could increase the γ volume fraction, whereas the FZ contains supersaturated α' which is ideal for the austenite reverse transformation. Gibbs *et al.* [88] showed that an optimal annealing temperature exists for the austenite reverse transformation, after which, subsequent grain growth begins to destabilize the γ by detrimentally increasing the M_s temperature [90].

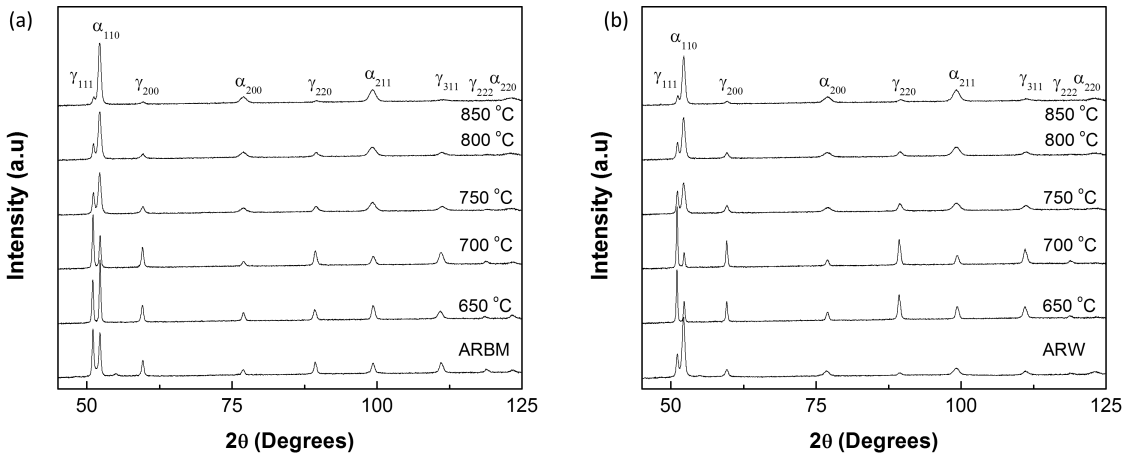

Figure 6.6: X-Ray Diffraction patterns of the heat treated MMn steel (a) BM and (b) FZ.

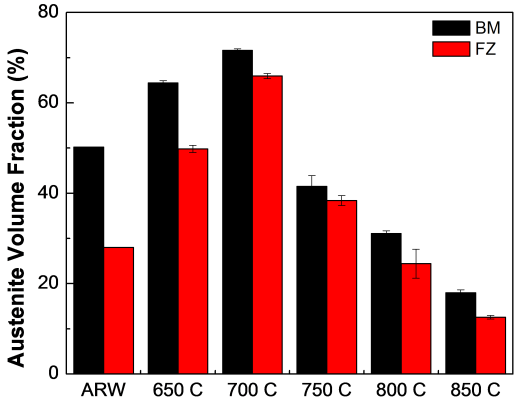

Figure 6.7: Austenite volume fractions of the BM and FZ of heat treated MMn steel

6.3 Tensile Testing

Continued from tensile testing conducted on sub-size specimens in Chapter 5, testing of full size sheet type ASTM E8-13 tensile specimens was conducted to determine the effects associated with specimen geometry. It was observed that the as-received BM (ARBM) exhibited anisotropic mechanical property behavior depending on the orientation of the specimen as shown in Figure 6.8. Table 6.1 contains a summary of the mechanical properties of the BM properties. The strong anisotropic nature of the as-received material suggests that the directionality of the sheet during cold forming operations must be taken into consideration.

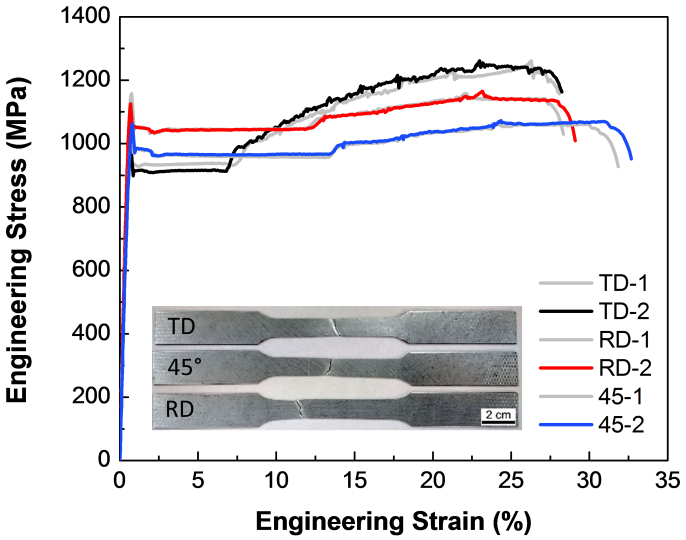

Figure 6.8: Engineering stress-strain curves of as-received MMn steel BM for specimens machined along the rolling direction (RD), transverse direction (TD) and diagonal directions (45°)

Standard sheet type tensile specimens of as-received laser welded (ARW) MMn steel were observed to fracture in a brittle manner at the FZ contrary to the findings of the sub-size tensile specimen geometry observed in Chapter 5. Figure 6.9 shows the engineering stress-strain curves. From Table 6.2, the σ_{UTS} and ϵ_{Total} were 1003 $\pm$ 28 MPa and 0.69 $\pm$ 0.04 % respectively. Compared to the ARBM specimens, fracture in the ARW specimens occurred when the stress approached the yield point of the BM. The joint strength and ductility ratios of the ARW condition were observed to be approximately 80% and 2%

Table 6.1: Tensile mechanical properties of medium-manganese steel

Orientation	$\sigma_{\mathbf{LYP}}$ *(MPa)*	$\sigma_{\mathbf{UTS}}$ *(MPa)*	$\epsilon_{\mathbf{YPE}}$ *(%)*	$\epsilon_{\mathbf{Total}}$ *(%)*	$\sigma_{\mathbf{UTS}}$ **X** $\epsilon_{\mathbf{Total}}$ *(MPa%)*
TD	1044 ± 8	1259 ± 2	6.3 ± 0.3	28.7 ± 0.4	33,342
45°	963 ± 2	1068 ± 5	12.5 ± 0.2	32.1 ± 0.6	34,258
RD	924 ± 11	1161 ± 3	11.0 ± 0.2	27.9 ± 0.2	35,122

respectively. The effect of introducing a local heterogeneous microstructure as a result of melting and re-solidification of the material during laser welding ultimately leads to fracture. This suggests that the FZ material of the laser welded MMn steel is very brittle and unsuitable for cold forming applications.

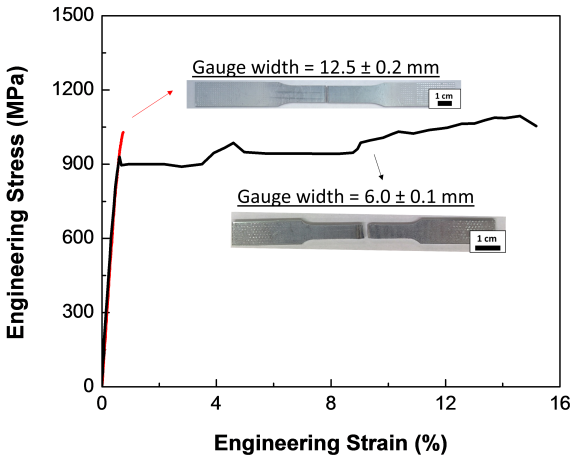

Figure 6.9: Engineering stress-strain curve of laser welded MMn steel with two different specimen geometries

The fracture surfaces of the BM MMn tensile specimen (Figure 6.10(a)) reveal classic flat dimple rupture resulting from micro-void coalescence. Comparatively, the flat facetted grain boundaries observed on the FZ fracture surface of the laser welded specimen (Figure 6.10(b)) suggests weak adhesion between individual grains in the FZ.

A cross section of the fractured weld specimen (Figure 6.11(a)) shows that the fracture occurred directly down the center of the fusion line. The center-line is the last material to solidify in welds and has a tendency to contain a high solute concentration while experiencing the slowest cooling rate [69]. Bifurcation of the crack (Figure 6.11(b-c))into the

Table 6.2: Mechanical properties of laser welded medium-manganese steel for different tensile specimen geometries

Gauge Width *(mm)*	$\sigma_{\mathbf{UTS}}$ *(MPa)*	$\epsilon_{\mathbf{Total}}$ *(%)*	$\sigma_{UTS}^{ARW}/\sigma_{UTS}^{ARBM}$ *(%)*	$\epsilon_{Total}^{ARW}/\epsilon_{Total}^{ARBM}$ *(%)*
12.5	1003 ± 28	0.69 ± 0.04	79.7	2.5
6.0	1091 ± 1	16.2 ± 0.6	95.9	50.6

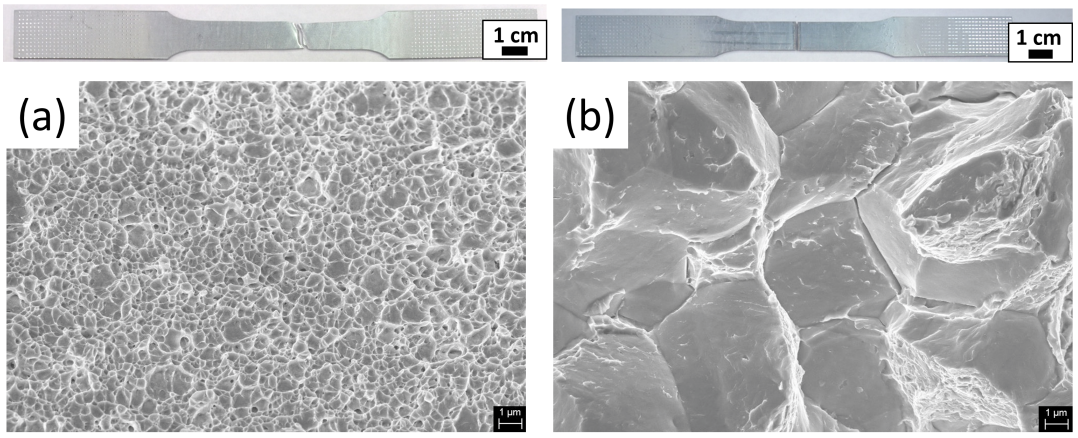

Figure 6.10: SEM micrographs of the fracture surfaces of (a) BM and (b) laser welded MMn steel

weld material transverse to the fracture plane was also observed. The secondary cracks were observed to progress along the prior austenite grain boundaries (PAGBs), leading to suspicion that unfavorable grain boundary nucleation of a specific phase was responsible for the brittle behavior.

High resolution SEM micrographs (Figure 6.12) of several grain boundaries revealed the presence of a white nanoscale sized precipitates along grain boundaries and particularly pronounced at triple point junctions. EDS scans of the region showed increased concentration of C and Mn at these locations. Kuzmina *et al.* found heightened concentrations of C and Mn occurred at PAGBs upon slow cooling after a homogenization heat treatment [91]. The microsegregation of these elements upon solidification and their nucleation on high energy sites such as grain boundaries could be partly responsible for the premature fracture. However, further investigation by TEM analysis must be conducted to characterize and quantify these precipitates.

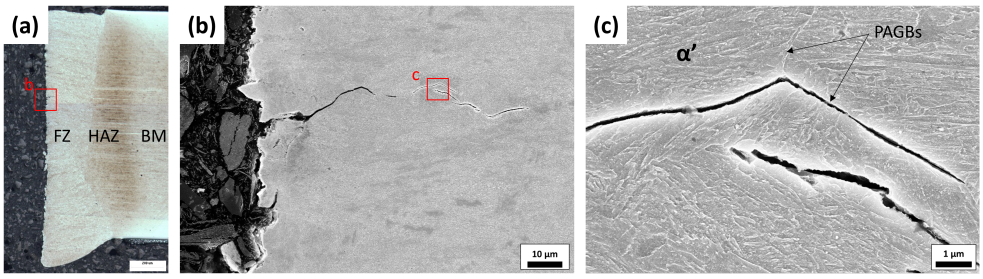

Figure 6.11: Cross section of fractured laser welded MMn tensile test specimen showing the (a) overall view, (b) secondary crack, (c) magnified view of the inset region in (b)

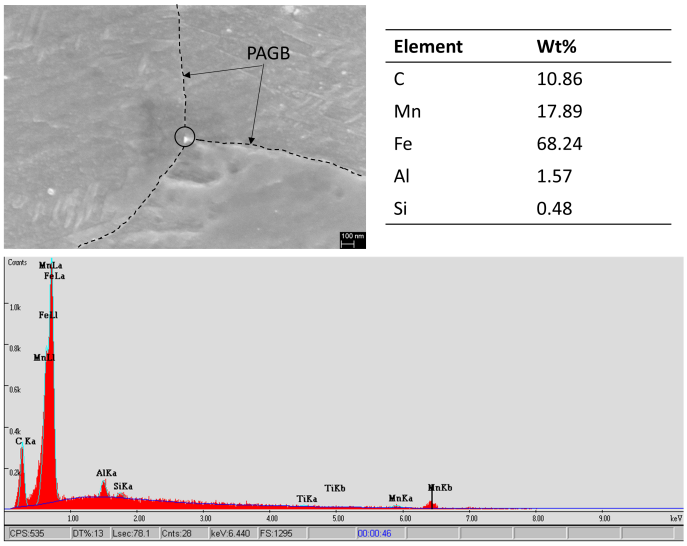

Element	Wt%
C	10.86
Mn	17.89
Fe	68.24
Al	1.57
Si	0.48

Figure 6.12: Representative SEM micrograph and EDS spectrum of the zone around a prior austenite triple point grain boundary

6.3.1 Effect of Strain Rate

The effect of strain rate on the as-received MMn steel BM and laser weld mechanical properties were investigated to determine if the premature fracture in the laser welded joints was dependent on the deformation rate. Sheet type tensile specimens of both the BM and laser welded joints were tested under constant tensile strain rates of 0.001, 0.01 and 0.1 s^{-1}. Figure 6.13 shows the mechanical properties obtained under the various strain rate conditions. As the strain rate increases, the σ_{YS} of the BM MMn steel (Figure 6.13(a)) increased slightly whereas σ_{UTS} decreased. The ϵ_{Total} of the BM also increased slightly. Table 6.3 summarizes the mechanical properties of the BM obtained under various strain rate conditions.

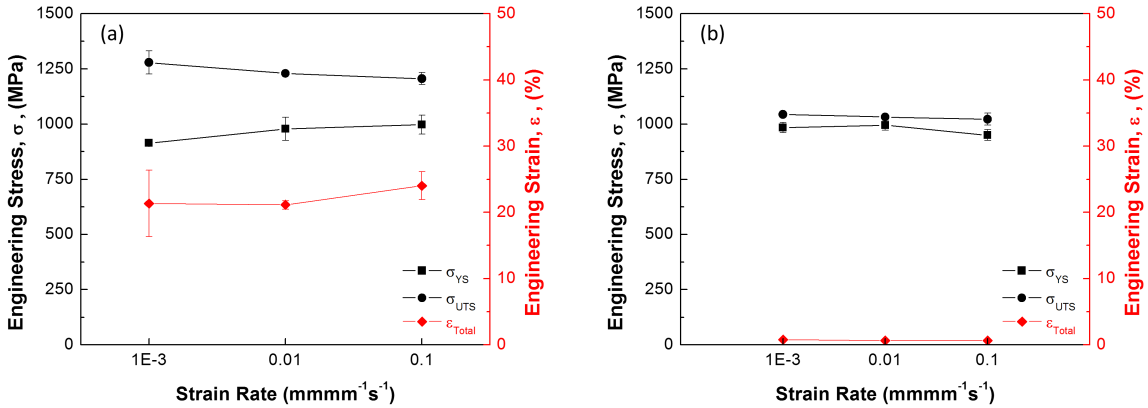

Figure 6.13: Engineering stress and strain values of (a) BM and (b) laser welded joints of MMn under strain rates of 0.001, 00.1 and 0.1 s^{-1}

Table 6.3: Strain rate mechanical properties of medium-manganese steel

Strain Rate s^{-1}	$\sigma_{\mathbf{LYP}}$ *(MPa)*	$\sigma_{\mathbf{UTS}}$ *(MPa)*	$\epsilon_{\mathbf{Total}}$ *(%)*
0.001	914 ± 2	1279 ± 52	21.4 ± 5.0
0.01	977 ± 52	1229 ± 8	21.1 ± 0.6
0.1	998 ± 43	1206 ± 27	24 ± 2

Comparatively, the laser welded joints (Figure 6.13(b))showed little deviation over the strain rate testing range. Table 6.4 summarizes the mechanical properties of the BM obtained under various strain rate conditions. Therefore, the strain rate has a negligible

effect on the failure of the laser welded joint and that the limiting factor contributing to the FZ failure of the laser welded joints is the brittle nature of the FZ.

Table 6.4: Mechanical properties of fiber laser welded medium-manganese steel under different strain rates

Strain Rate s^{-1}	$\sigma_{\mathbf{YS}}$ *(MPa)*	$\sigma_{\mathbf{UTS}}$ *(MPa)*	$\epsilon_{\mathbf{Total}}$ *(%)*
0.001	984 ± 23	1044 ± 7	0.8 ± 0.1
0.01	995 ± 23	1032 ± 8	0.7 ± 0.1
0.1	950 ± 24	1022 ± 28	0.7 ± 0.1

6.4 Heat Treatment and Mechanical Properties

Tensile testing of MMn steel BM and laser welded joints showed several complications which could limit the applications of MMn as a viable AHSS steel alternative. Firstly, the large yield point elongation associated with the localized deformation caused by the TRIP effect can give rise to undesirable cosmetic surfaces after forming. Secondly, the substantial anisotropy associated with the blank orientation may decrease the potential applications within the structural body. Lastly, the brittle FZ after laser welding prevents the application of the steel under mass manufacturing environments. However, applying an industrially acceptable post-weld heat treatment process, such as press hardening, may improve the prospects. Inter-critical annealing has been shown to effectively decrease the yield point elongation and anisotropy of MMn steels [81, 92]. The austenite reverse transformation has been shown to be an effective method to reduce the brittle α' into ultra-fine lamellar duplex $\alpha + \gamma$ [93]. By applying a press hardening heat treatment to the laser welded MMn steel blank, the brittle α' martensite may have a chance to undergo an austenite reverse transformation while simultaneously encouraging the diffusion of segregated solute atoms to redistribute throughout the FZ.

Figure 6.14 shows the engineering stress-strain curves of the ARW condition after heat treatment at the specified temperature for 3 minutes. At 650 °C, the laser welded specimen recovers a substantial amount of ductility over the ARW baseline condition. A reduced yield point elongation effect is observed, which is accompanied by an increase in stress which was associated with the interaction of the Lüders bands with the hard FZ microstructure shown previously in Chapter 5. Due to the furnace temperature and short soak time, the microstructure is not sufficiently homogenized with the rest of the BM in the specimen.

The ductility recovery of the joint is even more pronounced in the 700 °C specimen, which corroborates the findings reported in the aforementioned microstructural investigation that the austenite reverse transformation is more advanced at 700 °C compared to 650 °C. At a heat treatment temperature of 750 °C, the yield point elongation is completely eliminated and a large increase in σ_{UTS} is also observed; possibly due to greater homogenization of the steel at a temperature close to A_3. Above 700 °C, failure initiated in a very brittle fashion, which could be attributed to the formation of undesirable carbides and destabilization of γ [90]. As a result of the temperature investigation, 700 °C was identified as the best potential heat treatment parameter to further study the effect of heat treatment on fiber laser welds of MMn steel.

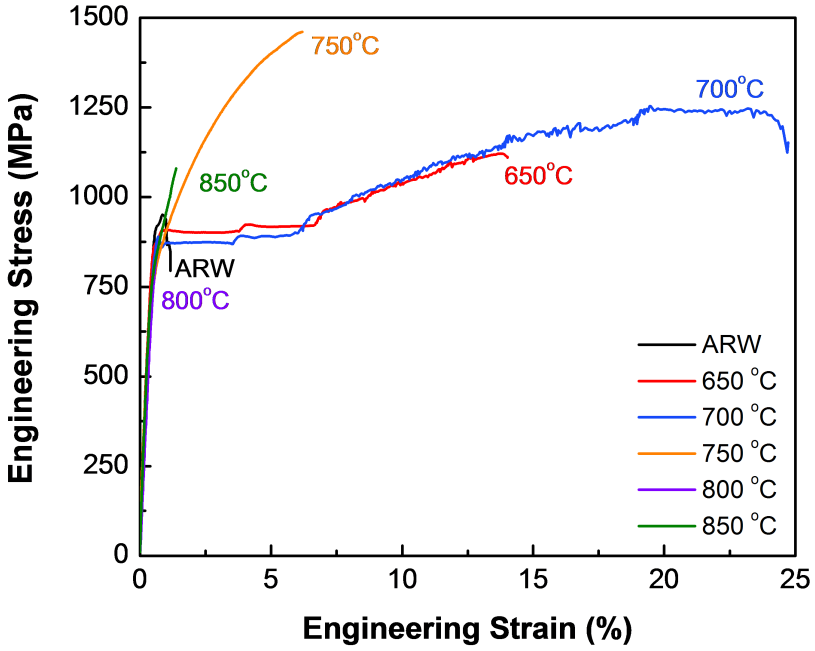

Figure 6.14: Engineering stress-strain curves of laser welded MMn heat treated at temperatures between 650-850 °C for 3 mins

Figure 6.15(a) shows the representative engineering stress-strain curves of the MMn BM processed at 700 °C for various soak times between 3-7 minutes. Heat treatment effectively reduced the yield point elongation, raised the σ_{UTS} and reduced the total achievable $\epsilon_{\mathrm{Total}}$ with increasing soak time. The inset macro photographs of the tensile specimen indicate that failure occurred along within the gauge length region for all the tests. A transition from ductile necking behaviour to flat, brittle fracture occurred between soak temperatures of 5 and 6 minutes. Figure 6.15(b) illustrates the engineering stress-strain curves of the

laser welded MMn specimens. Heat treatment improved the ductility of the specimens significantly, achieving elongations on par with the heat treated BM at times. Visual inspection of the tensile specimens show that fracture in the BM region outside of the weld occurs for temperatures of 3 and 4 minutes, where as prolonged exposure to the higher temperature environments resulted in fracture within the FZ.

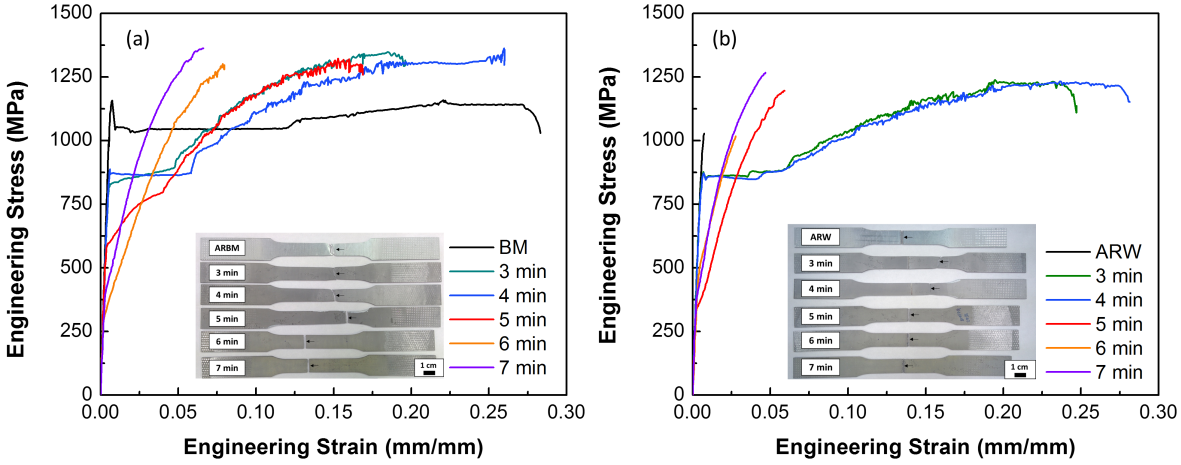

Figure 6.15: Representative Engineering stress-strain curves of MMn (a) base metal and (b) laser welded specimens heat treated at 700 °C for furnace soak temperatures of 3-7 minutes followed by quenching

Figure 6.16(a) and Figure 6.16(b) compare the σ_{YS} and σ_{UTS} of both ARBM and ARW to the non-heat treated specimens respectively. As expected, the σ_{YS} decreases with increasing soak temperature; however, the σ_{UTS} was not as significantly affected. This could be a result of the limited amount of unstabilized γ allowed to transform to martensite upon quenching. From the microstructure study earlier, it was observed that the BM microstructure remained fairly intact when heat treating at 700 °C which suggests that a significant volumetric fraction exists as austenite even after quenching. Figure 6.16(c) illustrates the tensile toughness as a function of soak temperature. Toughness was calculated as the integrated area under the curve of the respective engineering stress-strain curve shown in Equation 6.1 below.

$$U_T = \int_0^{\epsilon_f} \sigma d\epsilon \tag{6.1}$$

Every soak temperature tested resulted in a lower toughness value compared to the as-received BM condition; however, the welded specimens all showed significant improvement. Figure 6.16(d) indicates that the total elongation achieved by the heat treated welded specimens approached those of the as-received BM after 3 - 4 minutes. A sharp decrease in ductility occurs after 4 minutes indicates an increase in the formation of brittle phases in the steel. These findings are consistent with the observations that although increasing the annealing time may increase the γ volume fraction, grain growth eventually decreases the the stability of the γ [94].

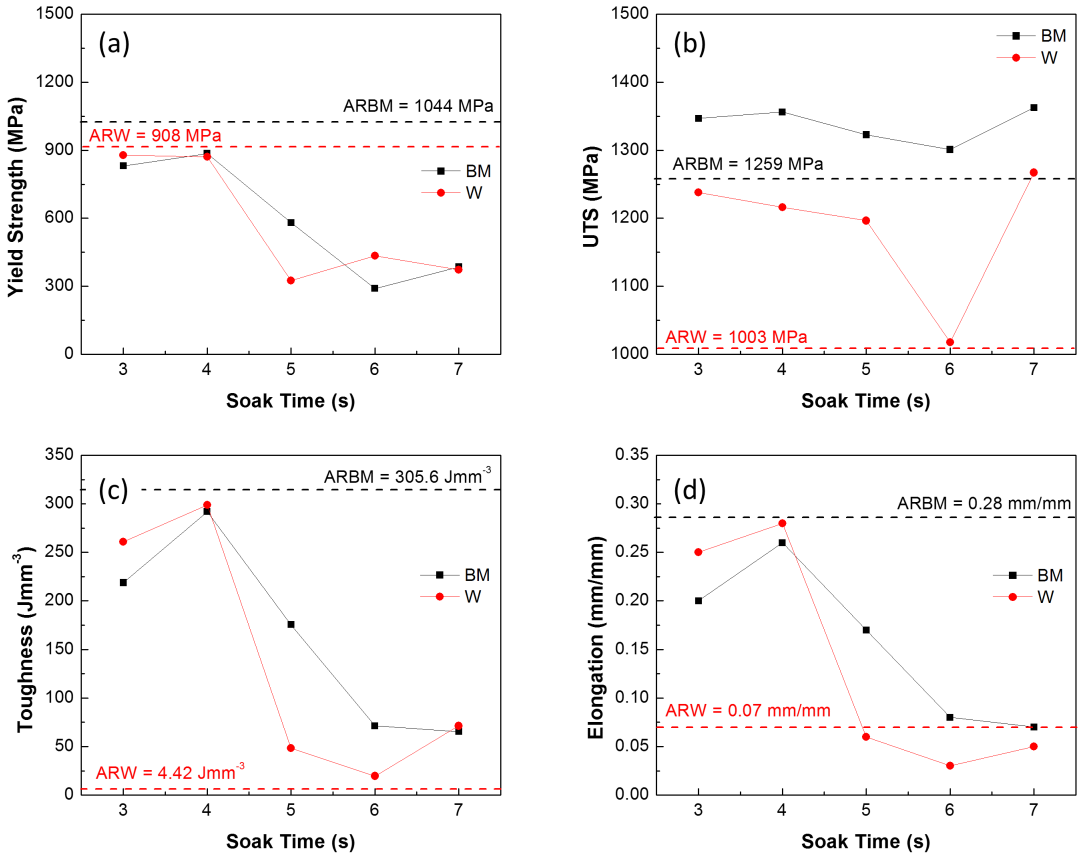

Figure 6.16: Comparison of (a) yield strength, (b) ultimate tensile strength, (c) toughness and (d) elongation achieved by base metal (BM) and laser welded (W) MMn steel after 700 °C heat treatment

Figure 6.17 illustrates the stark difference in ductility observed in laser welded specimens in terms of the surface fracture morphology. After processing for 3 minutes (Figure 6.17(a)), the fracture of the welded specimen occurred in the base metal, showing evidence of flat dimple rupture. Sporadic large dimples on the surface (Figure 6.17(b)) were found to contain AlN inclusions, possibly a by-product of the elevated temperature encouraging the growth of such inclusions in the steel. After processing for 7 mins (Figure 6.17(c)), the fracture surface was more inter-granular in nature, exhibiting signs of cleavage fracture across grains (Figure 6.17(b)).

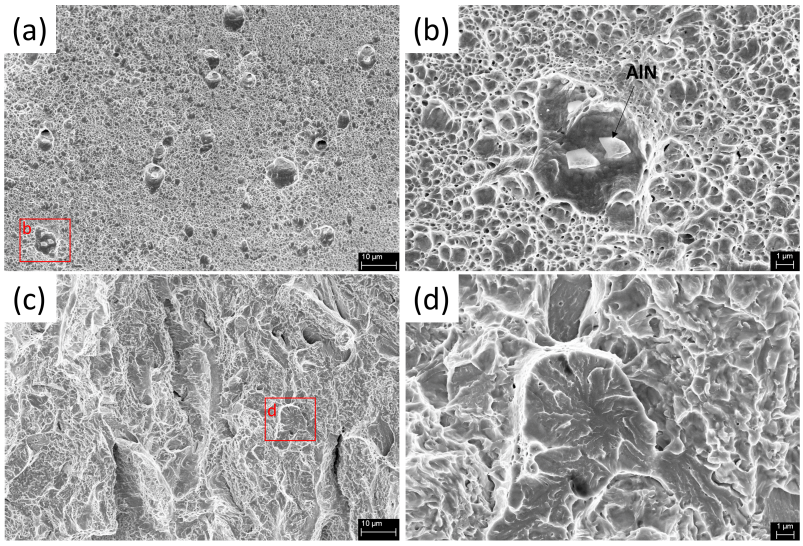

Figure 6.17: SEM micrographs of the fracture surface of laser welded MMn steel joints processed at 700 °C for (a,b) 3 mins and (c,d) 7 mins

6.5 Summary

Heat treatment of MMn steel LWB was explored to assess the potential application to press hardening. Microstructure characterization and phase analysis was performed in order to explain the microstructure.

The formation of carbides at high angle grain boundaries result in void nucleation at prior austenite grain boundaries at lower stress levels. As a result, tensile testing of standard sized specimens cut from laser welded blanks appear to exhibit lower ultimate tensile strength compared to the base metal. Additional investigation on the sensitivity of the FZ to the tensile specimen geometry should be conducted to assess the effects of heat treatment on the yield point elongation.

Heat treating laser welded joints over a range of temperatures indicated that the microstructure rapidly loses the ultra-fine lamellar structure above the A_3 temperature. Heat treating at an inter-critical temperature was found to cause the austenite reverse transformation to occur in the laser weld FZ.

Joint ductility of the laser welded MMn was substantially improved with an inter-critical heating temperature of 700 °C for 3 -4 minutes. However, a prolonged holding time can cause severe destabilization of the γ and is detrimental to the ductility of the steel.

Chapter 7

Conclusions and Recommendations

7.1 Microstructure Evolution of Laser Welded Medium-Manganese Steel

The investigation of diode laser welding on the thermal cycle and microstructural evolution of MMn steel was conducted. The steel temperature was measured *in situ* and compared to the microstructure and microhardness observed at the respective locations within the blank. The following conclusions were made:

1. The ultra-fine lamellar structure of the BM MMn steel is remarkably stable despite exposure to high temperatures in the HAZ.
2. Peak temperature above A_3 has a significant effect on microstructure morphology.
3. Transverse microhardness profile suggests the absence of HAZ softening.
4. Microsegregation of Mn was observed between dendrite cores in the weld FZ which shift the M_s temperature and produce pockets of stable γ.

7.2 Mechanical Property and Microstructure Correlation of Laser Welded Medium-Manganese Steel

MMn steel, HSLA steel and DP980 steel and their dissimilar fiber laser welded combinations were investigated in relation to their microstructure, hardness and mechanical

properties. The following conclusions were derived from this study:

1. The FZ of the laser welded similar MMn-MMn steel joints consisted primarily of martensite with a small amount of austenite between dendrite cores. Dissimilar welds with HSLA and DP980 produced primarily martensitic FZ with similar hardness.

2. Negligible HAZ softening in the MMn steel was observed due to limited grain growth kinetics and a lack of pre-existing martensite in the BM.

3. The laser welded similar MMn-MMn joints achieved approximately 96% joint efficiency with respect to the BM. MMn-MMn laser welded specimens were observed to exhibit a secondary yield point due to the impediment of the strain-induced transformation by the martensitic FZ microstructure. Dissimilar welds failed in BM of the DP980 and HSLA steel due to yielding in the weaker substrate material.

4. Formability of similar MMn-MMn laser welded blanks was severely limited by the brittle nature of the fusion zone when subjected to bi-axial stretch loading conditions. Forming ductility of MMn-HSLA and MMn-DP980 steels demonstrated significant improvement by shifting the stress localization towards the weaker steel.

7.3 Heat Treatment of Laser Welded Medium-Manganese Steel Blanks

The application of LWB consisting of MMn steel to press hardening applications was studied. Evaluation of the microstructure and hardness with respect to heat treatment time and temperature were analyzed. Tensile testing was conducted to assess the performance of the treated joints.

1. A comparison of different tensile geometry types showed that the mechanical properties appear to be sensitive to the specimen geometry. Brittle FZ fracture occurred in the standard size tensile specimen compared to the more ductile fracture observed in the sub-size tensile specimen in the previous chapter.

2. Subjecting laser welded joints to inter-critical temperatures rapidly causes the austenite reverse transformation to occur which decreases the overall hardness of the joint.

3. Prolonged holding time produces an extremely brittle joint due to destabilization of the austenite; this suggests that the heat treatment window is fairly narrow.

4. Joint ductility was significantly improved by heat treating the joint at 700 °C for 3 and 4 minutes followed by quenching. The heat treatment temperature and soak time for this MMn steel is lower and shorter than that of conventional C-Mn-Si PHS.

7.4 Recommendations

The investigation addressed several issues surrounding laser welding of MMn steel. The novelty of the study resided primarily in the unknown response of the BM with respect to the rapid heating and cooling associated with laser welding. Although several conclusions were made, the following recommendations for future study can be made:

1. Provided the ultra-fine lamellar structure of the BM and the apparent stability at high temperature, it is of great interest to evaluate the crystallographic structure via transmission electron microscopy (TEM) of the HAZ and FZ of MMn steel after laser welding.

2. BM formability of MMn steel shows promising results; a different grade of MMn steel with less yield point elongation may yield better LWB formability results by reducing the strain between the FZ and the BM.

3. Additional tensile testing of the similar MMn-MMn laser welded blanks to determine the sensitivity of the FZ to the specimen geometery should be investigated

4. The heat treatment investigation shows promising potential for a new grade of PHS. Further testing with a MMn steel with a reduced Mn concentration (5-7 wt%) should be investigated in conjunction with LWB to assess the potential for material cost reduction.

APPENDICES

Appendix A

A.1 Fiber Laser Welding Parameter Selection

Figure A.1 demonstrates a 4 x 4 matrix used to narrow down the laser power and welding speed for BoP welds on MMn steel. Laser power above 4kW was observed to be unstable and generated a significant amount of weld spatter due to keyhole instability [4, 95, 96]. The instability arises from fluctuations in the vapor-liquid interface within the keyhole where the surface tension of the liquid and the vapor pressure of the gas inside the keyhole are not in equilibrium. Spatter generation results in mass loss from fusion zone, causing a sharp notch called concavity. One aspect of quality control systems used by LWB manufacturers accounts for the concavity to ensure that a stress raiser does not occur as a result of excessive concavity. Figure A.2(a) illustrates an example calculation used to quantify concavity from standard GM4485M. Therefore, laser powers below 4kW were considered adequate for the purposes of consistency. Figure A.2(b) shows the typical relationship between concavity, laser power and welding speed.

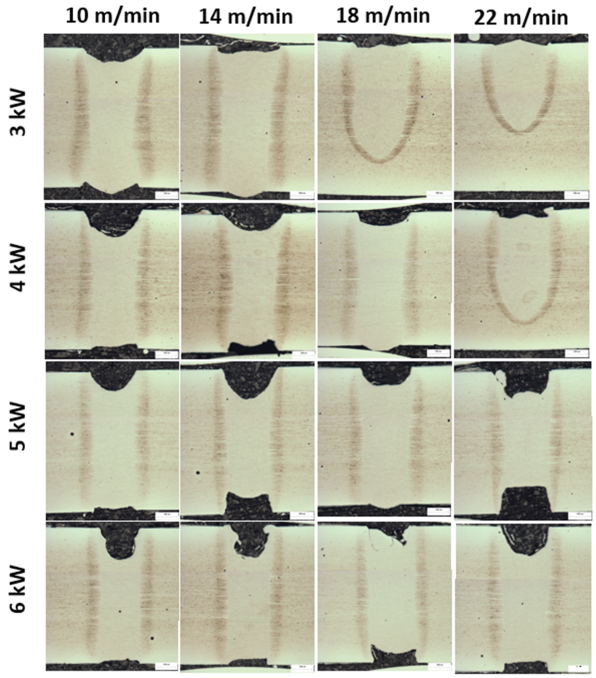

Figure A.1: Fiber laser weld parameter selection matrix

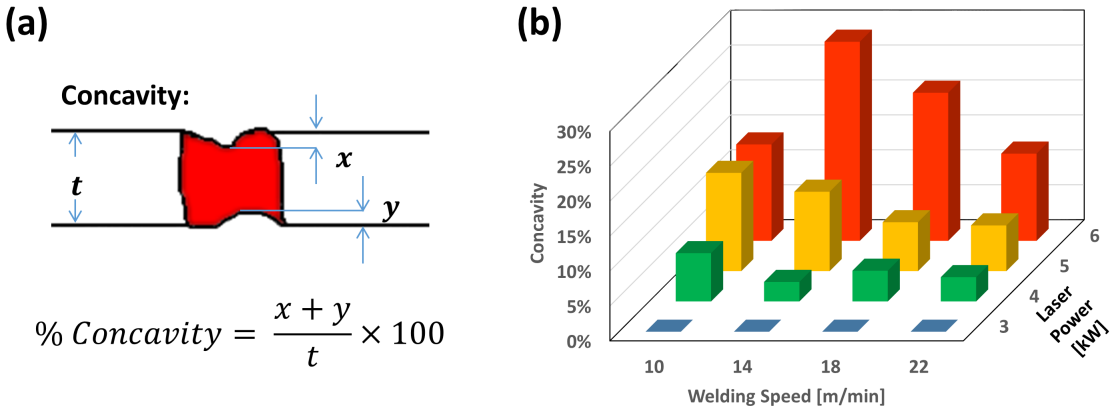

Figure A.2: Schematic illustration of the (a) geometrical calculation for concavity defined by GM4485M and (b) an example of the concavity, laser power and welding speed relationship

A.2 Concavity Mitigation by Defocusing

The focal position of the laser beam has a significant effect on the overall heat delivered to the workpiece. Having the laser focused on the top plane of the workpiece is not always the best solution when welding a butt joint because the spot size may be very small and unable to bridge gaps. Even in a situation where the clamping appears adequate and the butt joint is almost near perfect, the vapour pressure caused by the expanding gases during laser welding can be large enough to force the faces apart, reducing the effective energy delivery to the workpiece. From the optimization experiments, it was clear that in order to generate a wider operational window defocusing the beam was necessary to avoid any concavity that would adverse affect the results. Figure A.3(a) demonstrate the effect of defocusing on the reduction of concavity. A consequence of defocusing the beam results in a wider HAZ and FZ as shown graphically by the microhardness profile (Figure A.3(b)) and measurements of both the HAZ and the FZ (Figure A.3(c)). It was determined that a defocusing condition of 5 mm above the plane would be the most optimal condition to effectively eliminate concavity from occurring during the laser welding process.

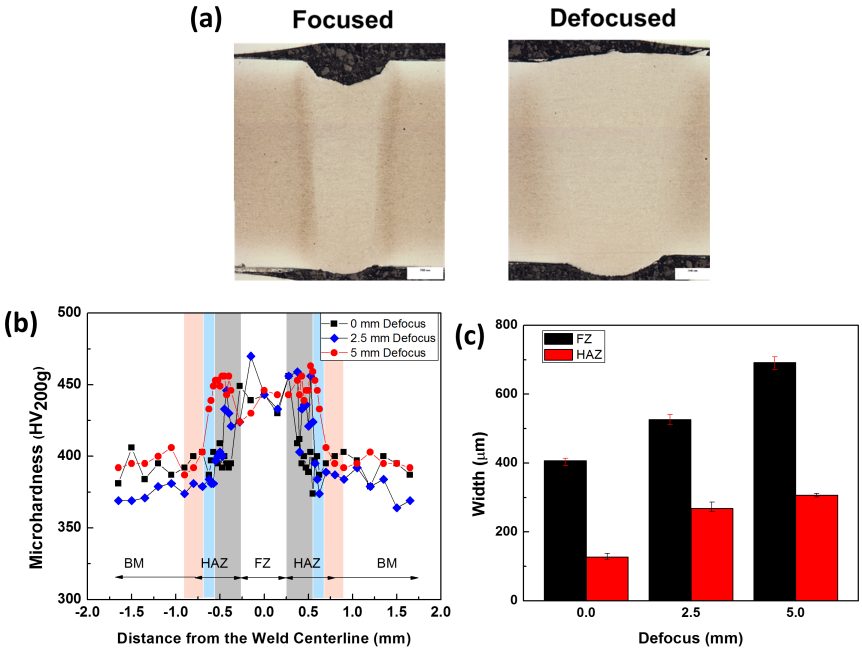

Figure A.3: Effect of defocusing on the (a) concavity profile, (b) microhardness profile and (c) FZ widths of fiber laser welded MMn steel

Appendix B

B.1 Manganese Evaporation

One the more noticeable effects of laser welding on high-Mn steel is the evaporation of Mn from the FZ [45]. It has been hypothesized that a decrease in the Mn concentration in the FZ could adversely affect the mechanical performance of the steel [45]. However, despite the evaporation of Mn from the FZ, LBWs of TWIP steel was still observed to exhibit a fully austenitic microstructure [47]. This indicates that the evaporation of Mn is not significant enough to effectively reduce the SFE of the FZ material because the initial Mn concentration is sufficiently large enough to offset the loss. In terms of MMn steel where the Mn concentration is much lower, the effects associated with Mn evaporation could have a more significant effect. EDS analysis was conducted on three different points in the BM and FZ of a MMn steel weld as shown in Figure B.1 and summarized in Table B.1. The average Mn concentration in the FZ of the weld compared to the BM was measured by EDS to be approximately 10.4 0.1 wt% and 10.2 0.2 wt% respectively. Compared to high-Mn steels, the amount of Mn evaporation during fiber laser welding MMn steel appears to be negligible.

Table B.1: Manganese Content (wt.%) in the BM and FZ of Laser Welded MMn Steel

Material	**Point**	**Location**	**Mn (wt.%)**
BM	1	Top	9.89
BM	3	Mid	10.12
BM	5	Bottom	10.42
FZ	2	Top	10.52
FZ	4	Mid	10.41
FZ	6	Bottom	10.31

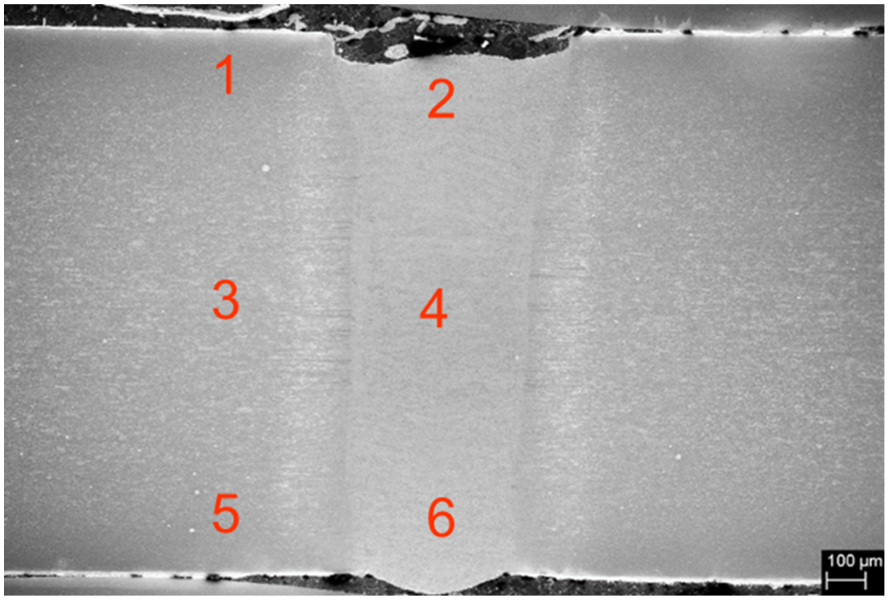

Figure B.1: SEM micrograph of a BoP fiber laser weld cross section of MMn steel demonstrating EDS locations

References

[1] Office of Transportation and Air Quality. EPA and NHTSA Finalize Hisotric National Program to Reduce Greenhouse Gases and Improve Fuel Economy for Cars and Trucks. 2010.

[2] Office of Transportation and Air Quality. EPA and NHTSA Set Standards to Reduce Greenhouse Gases and Improve Fuel Economy for Model Years 2017-2025 Cars and Light Trucks. 2010.

[3] A. Bandivadekar, K. Bodek, L. Cheah, C. Evans, T. Groode, J. Heywood, E. Kasseris, M. Kromer, and M. Weiss. On the Road in 2035 - Reducing transportation's petroleum consumption and GHG emissions. Technical Report July, MIT: Lab for Energy and the Environment, 2008.

[4] C. Dawes. *Laser Welding*. McGraw-Hill, New York, 1992.

[5] G. R. Gould. The Laser, Light Amplification by Stimulated Emission of Radiation. In *Ann Arbor Conf. Opt. Pump.*, page 128, Ann Arbor, 1959.

[6] G. Shannon. Laser welding modes: conduction, transisition & keyhole welding. [Online; Accessed 25-February-2016], 2016. http://info.amadamiyachi.com/blog/conduction-transition-and-keyhole-welding-modes.

[7] C. A. Walsh. Laser Welding - Literature Review. Technical Report July, Materials Science and Metallurgy Department, Univeristy of Cambridge, 2002.

[8] M. C. Chaturvedi. *Welding and Joining of Aerospace Materials*. Cambridge, UK ; Philadelphia, PA, USA : Woodhead Pub, Cambridge, UK ; Philadelphia, PA, USA, 2012.

[9] J. Zhou. Developments in pulsed and continuous wave laser welding technologies. In S Katayama, editor, *Handb. Laser Weld. Technol.*, pages 103–132. Cambridge : Woodhead Publishing, Cambridge, 1st edition, 2013.

[10] Y.-Y Cheng, X.-Z. Jin, S.-C. Li, and L.-C. Zeng. Fresnel absorption and inverse bremsstrahlung absorption in an actual 3D keyhole during deep penetration CO 2 laser welding of aluminum 6016. *Opt. Laser Technol.*, 44(5):1426–1436, 2012.

[11] P. Shcheglov. *Study of Vapour-Plasma Plume during High Power Fiber Laser Beam Infl uence on Metals*. PhD thesis, BAM Federal Institute for Materials Research and Testing, 2012.

[12] J. E. Geusic, H. M. Marcos, and L. G. Van Uitert. Laser Oscillations in Nd-Doped Yttrium Aluminum, Yttrium Gallium and Gadolinium Garnets. *Appl. Phys. Lett.*, 4(10):182, 1964.

[13] K. Howard, S. Lawson, and Y. Zhou. Welding Aluminium Sheet Using a High Power Diode Laser. *Weld. J.*, 85(5):81–90, 2006.

[14] Coherent Inc. Welding with High Power Diode Lasers. [Online; Accessed 25-February-2016], 2016. http://www.coherent.com/downloads/WeldingwithHPDoide Lasers_ Whitepaper.pdf.

[15] Photonics Media. Semiconductor lasers: An overview of commercial devices. [Online; Accessed 25-February-2016], 2016. http://www.photonics.com/EDU/Handbook.aspx?Tag=Lasers&AID=25099.

[16] C. J. Koester and E. Snitzer. Amplification in a Fiber Laser. *Appl. Opt.*, 3(10):1182, 1964.

[17] K. O. Hill, Y. Fujii, D. C. Johnson, and B. S. Kawasaki. Photosensitivity in optical fiber waveguides: Application to reflection filter fabrication. *Appl. Phys. Lett.*, 32(10):647–649, 1978.

[18] B. Shiner. Fiber Lasers: New types and features expand applications, 2016.

[19] C. Schneider and W. Prange. Tailored blanks: a material for new ways of design. *Thyssen Tech. Rep.*, 24(1):97–106, 1992.

[20] J. C. Ion. *Laser Processing of Engineering Materials*. Elsevier, 2005.

[21] Ž. Babic and M. Šljivic. Application of Tailored Blanks. *J. Technol. Plast.*, 27(1), 2002.

[22] Auto/Steel Partnership. Tailor welded blank applications and manufacturing A State-of-the-Art Survey. Technical report, Auto/Steel Partnership, 2001.

[23] Y.-K. Lee and J. Han. Current opinion in medium manganese steel. *Mater. Sci. Technol.*, 31(7):843–856, 2015.

[24] R. L. Miller. Ultrafine-grained microstructures and mechanical properties of alloy steels. *Metall. Trans.*, 3(4):905–912, 1972.

[25] E. O. Hall. The Deformation and Ageing of Mild Steel: II Characteristics of the L ders Deformation. *Proc. Phys. Soc. Sect. B*, 64(9):742–747, 1951.

[26] W. M. Baldwin. Yieid strength of metals as a function of grain size. *Acta Metall.*, 6:139–141, 1958.

[27] M. S. Rashid. Dual Phase Steels. *Annu. Rev. Mater. Sci.*, 11:245–66, 1981.

[28] M. S. Xia, E. Biro, Z.L. Tian, and Y. Zhou. Effects of Heat Input and Martensite on HAZ Softening in Laser Welding of Dual Phase Steels. *ISIJ Int.*, 48(6):809–814, 2008.

[29] S. K. Panda, N. Sreenivasan, M. L. Kuntz, and Y. Zhou. Numerical Simulations and Experimental Results of Tensile Test Behavior of Laser Butt Welded DP980 Steels. *J. Eng. Mater. Technol.*, 130(October):041003, 2008.

[30] N. Farabi, D.L. Chen, J. Li, Y. Zhou, and S.J. Dong. Microstructure and mechanical properties of laser welded DP600 steel joints. *Mater. Sci. Eng. A*, 527:1215–1222, 2010.

[31] G. Tandon and I. Vlaux. Lightweight door ring concepts using hot stamped laser welded blanks. In *Gt. Des. Steel*, 2014.

[32] G. Tandon and S. Devaraj. Light Weight Hot Stamped Laser Welded Blanks Side Structures for Narrow Offset Crash. In *Gt. Des. Steel*, 2015.

[33] E. De Moor, D. K. Matlock, J. G. Speer, and M. J. Merwin. Austenite stabilization through manganese enrichment. *Scr. Mater.*, 64(2):185–188, 2011.

[34] S. Allain, J. P. Chateau, O. Bouaziz, S. Migot, and N. Guelton. Correlations between the calculated stacking fault energy and the plasticity mechanisms in Fe-Mn-C alloys. *Mater. Sci. Eng. A*, 387-389(1-2 SPEC. ISS.):158–162, 2004.

[35] B. C. De Cooman, O Kwon, and K-G Chin. State-of-the-knowledge on TWIP steel. *Mater. Sci. Technol.*, 28(5):513–527, 2012.

[36] B. C. De Cooman. Alloy design UHS Intercritically Annealed 6%-12%Mn TWIP+TRIP steel. In *Comb. Aust. Mater. Soc.*, 2014.

[37] J.-H. Ryu, S. K. Kim, C. S. Lee, D.-W. Suh, and H. K. D. H. Bhadeshia. Effect of aluminium on hydrogen-induced fracture behaviour in austenitic Fe-Mn-C steel. *Proc. R. Soc. A Math. Phys. Eng. Sci.*, 469(201220458), 2012.

[38] M. Koyama, E. Akiyama, T. Sawaguchi, D. Raabe, and K. Tsuzaki. Hydrogen-induced cracking at grain and twin boundaries in an Fe-Mn-C austenitic steel. *Scr. Mater.*, 66(7):459–462, 2012.

[39] C. Beal. *Mechanical behaviour of a new automotive high manganese TWIP steel in the presence of liquid zinc.* Phd dissertation, L'Institut National des Sciences Appliquées de Lyon, 2011.

[40] C. Beal, X. Kleber, D. Fabregue, and M. Bouzekri. Embrittlement of a zinc coated high manganese TWIP steel. *Mater. Sci. Eng. A*, 543:76–83, 2012.

[41] C. Beal, X. Kleber, D. Fabregue, and M. Bouzekri. Liquid zinc embrittlement of twinning-induced plasticity steel. *Scr. Mater.*, 66(12):1030–1033, 2012.

[42] E. Tolf, J. Hedegård, and A. Melander. Surface breaking cracks in resistance spot welds of dual phase steels with electrogalvanised and hot dip zinc coating. *Sci. Technol. Weld. Join.*, 18(1):25–31, 2013.

[43] D Keil, M Zinke, and H Pries. Hot Cracking Phenomena in Welds III. In John C. Lippold, Thomas Boellinghaus, and Carl E. Cross, editors, *Hot Crack. Phenom. Welds III*, pages 209–223. Springer-Verlag Berlin Heidelberg, 2011.

[44] B. J. Sutton. *Solidification Behaviour and Hot Cracking Susceptibility of High Managanese Steel Weld Metals.* Msc thesis, Ohio State University, 2013.

[45] L. Mújica, S. Weber, and W. Theisen. Welding of twinning-induced plasticity steels. *Scr. Mater.*, 66(12):997–1001, 2012.

[46] V. Behm, M. Höfemann, A. Hatscher, A. Springer, S. Kaierle, D. Hein, M. Otto, and L. Overmeyer. Investigations on Laser Beam Welding Dissimilar Material Combinations of Austenitic High Manganese (FeMn) and Ferrite Steels. *Phys. Procedia*, 56:610–619, 2014.

[47] T. Wang, M. Zhang, W. Xiong, R.-D. Liu, W. Shi, and L. Li. Microstructure and tensile properties of the laser welded TWIP steel and the deformation behavior of the fusion zone. *Mater. Des.*, 83:103–111, 2015.

[48] R. Krupitzer. Auto/Steel Partnership: NSF 3rd Generation Advanced High Strength Steels. In *Am. Iron Steel Inst. - Auto/Steel Partnersh.*, 2010.

[49] T. Furukawa. Dependence of strengthductility characteristics on thermal history in lowcarbon, 5 wt-%Mn steels. *Mater. Sci. Technol.*, 5(5):465, 1989.

[50] J.-C. Han, Seung Joon Lee, C.-Y. Lee, S.-J. Lee, S.-Y. Jo, and Y.-K. Lee. The size effect of initial martensite constituents on the microstructure and tensile properties of intercritically annealed Fe9Mn0.05C steel. *Mater. Sci. Eng. A*, 633:9–16, 2015.

[51] H. L. Yi, P. J. Du, and B. G. Wang. A new invention of press-hardened steel achieving 1880 MPa tensile strength combined with 16% elongation in hot-stamped parts. In *5th Int. Conf. Hot Sheet Met. Form. High-Performance Steel2*, pages 725–734, 2015.

[52] R. Rana, C. H. Carson, and J. G. Speer. Hot forming response of medium manganese transformation induced plasticity steels. In *5th Int. Conf. Hot Sheet Met. Form. High-Performance Steel*, pages 391–399, 2015.

[53] J. G. Speer, D. K. Matlock, B. C. De Cooman, and J. G. Schroth. Carbon partitioning into austenite after martensite transformation. *Acta Mater.*, 51(9):2611–2622, 2003.

[54] M. Maalekian. The Effects of Alloying Elements on Steels. Technical report, Technische Universität Graz Institut, Institut für Werkstoffkunde, Schweißtechnik und Spanlose Formgebungsverfahren, Graz, Austria, 2007.

[55] D.C. Saha, I.S. Chang, and Y.-D. Park. Heat-affected zone liquation crack on resistance spot welded TWIP steels. *Mater. Charact.*, 93:40–51, 2014.

[56] J.-H. Han, S.-J. Lee, J.-G. Jung, and Y.-K. Lee. The effects of the initial martensite microstructure on the microstructure and tensile properties of intercritically annealed Fe9Mn0.05C steel. *Acta Mater.*, 78:369–377, 2014.

[57] N. Nakada, K. Mizutani, T. Tsuchiyama, and S. Takaki. Difference in transformation behavior between ferrite and austenite formations in medium manganese steel. *Acta Mater.*, 65:251–258, 2014.

[58] D.-W. Suh, J.-H. Ryu, M. S. Joo, H. S. Yang, K. Y. Lee, and H. K. D. H. Bhadeshia. Medium-Alloy Manganese-Rich Transformation-Induced Plasticity Steels. *Metall. Mater. Trans. A*, 46A:286–293, 2013.

[59] H. Huang, O. Matsumura, and T. Furukawa. Retained austenite in. *Mater. Sci. Technol.*, 10(July):621–626, 1994.

[60] Y.-K. Lee. Heat Treatment of Medium-Manganese Steels, 2013.

[61] J.-H. Ryu, D.-I. Kim, H.-S. Kim, H. K. D. H. Bhadeshia, and D.-W. Suh. Strain partitioning and mechanical stability of retained austenite. *Scr. Mater.*, 63(3):297–299, 2010.

[62] C. Wang, J. Shi, C.Y. Wang, W.J. Hui, and M.Q. Wang. Development of Ultrafine Lamellar Ferrite and Austenite Duplex Structure in 0.2C5Mn Steel during ART-annealing. *ISIJ Int.*, 51(4):651–656, 2011.

[63] W. Q. Cao, C. Wang, C. Y. Wang, J. Shi, M. Q. Wang, H. Dong, and Y. Q. Weng. Microstructures and mechanical properties of the third generation automobile steels fabricated by ART-annealing. *Sci. China Technol. Sci.*, 55(7):1814–1822, 2012.

[64] G. Krauss. *Steels: Processing, Structure, and Performance*. ASM International, 2005.

[65] J. Shi, H. F. Xu, J. Zhao, W. Q. Cao, C. Wang, C. Y. Wang, J. Li, and H. Dong. Effect of austenization temperature on the microstructure evolution of the medium manganese steel (0.2C-5Mn) during ART-annealing. *Acta Metall. Sin. (English Lett.*, 25(2):111–123, 2012.

[66] J. Shi, Jun Hu, C. Wang, C.-Y. Wang, H. Dong, and W. Q. Cao. Ultrafine Grained Duplex Structure Developed by ART-annealing in Cold Rolled Medium-Mn Steels. *J. Iron Steel Res. Int.*, 21(2):208–214, 2014.

[67] R. Zhang, W. Q. Cao, Z. J. Peng, J. Shi, H. Dong, and C. X. Huang. Intercritical rolling induced ultrafine microstructure and excellent mechanical properties of the medium-Mn steel. *Mater. Sci. Eng. A*, 583:84–88, 2013.

[68] D.-W. Suh, Seong Jun Park, Chang Hoon Lee, and Sung Joon Kim. Microstructure and mechanical behaviors of 0.1C-13Mn metastable austenitic steel. *Metall. Mater. Trans. A*, 40(2):264–268, 2009.

[69] S. Kou. *Welding Metallurgy*. John Wiley & Sons Inc., Hoboken, New Jersey, 2nd edition, 2003.

[70] A. S. Podder and H. K. D. H. Bhadeshia. Thermal stability of austenite retained in bainitic steels. *Mater. Sci. Eng. A*, 527(7-8):2121–2128, 2010.

[71] M. S. Xia, Z.L. Tian, L. Zhao, and Y. Zhou. Fusion Zone Microstructure Evolution of Al-Alloyed TRIP Steel in Diode Laser Welding. *Mater. Trans.*, 49(4):746–753, 2008.

[72] V. H. Baltazar Hernandez, S. S. Nayak, and Y. Zhou. Tempering of martensite in dual-phase steels and its effects on softening behavior. *Metall. Mater. Trans. A Phys. Metall. Mater. Sci.*, 42(10):3115–3129, 2011.

[73] L. Mujica, S. Weber, H. Pinto, C. Thomy, and F. Vollertsen. Microstructure and mechanical properties of laser-welded joints of TWIP and TRIP steels. *Mater. Sci. Eng. A*, 527(7-8):2071–2078, 2010.

[74] B. Wang, Q. Q. Duan, G. Yao, J. C. Pang, Z. F. Zhang, L. Wang, and X. W. Li. Fatigue fracture behaviour of spot welded B1500HS steel under tensile-shear load. *Fatigue Fract. Eng. Mater. Struct.*, pages n/a–n/a, 2015.

[75] D.C. Saha, D. Westerbaan, S.S. Nayak, E. Biro, a.P. Gerlich, and Y. Zhou. Microstructure-properties correlation in fiber laser welding of dual-phase and HSLA steels. *Mater. Sci. Eng. A*, 607:445–453, 2014.

[76] W. Xu, D. Westerbaan, S.S. Nayak, D.L. Chen, F. Goodwin, and Y. Zhou. Microstructure and fatigue properties of fiber laser welded dissimilar joints between high strength low alloy and dual-phase steels. *Mater. Des.*, 51:665–675, 2013.

[77] J.-H. Ryu, M. S. Joo, H. S. Yang, D.-W. Suh, and H. K. D. H. Bhadeshia. Medium Mn TRIP-assisted steels. In *POSTECH Gift*, 2010.

[78] J.-H. Ryu, J.-I. Kim, H.-S. Kim, C.-S. Oh, H. K. D. H. Bhadeshia, and D.-W. Suh. Austenite stability and heterogeneous deformation in fine-grained transformation-induced plasticity-assisted steel. *Scr. Mater.*, 68(12):933–936, 2013.

[79] C.W. Lee, W.S. Choi, L. Cho, Y.R. Cho, and B. C. De Cooman. LME Related Microcrack propagation on Zn coated PHS. *ISIJ Int*, 55(1):264–271, 2015.

[80] C.-Y. Lee, J.-Y. Jeong, J.-H. Han, S.-J. Lee, S. Lee, and Y.-K. Lee. Coupled strengthening in a medium manganese lightweight steel with an inhomogeneously grained structure of austenite. *Acta Mater.*, 84:1–8, 2015.

[81] S.-W. Lee and B. C. De Cooman. On the selection of the optimal intercritical annealing temperature for medium Mn TRIP steel. *Metall. Mater. Trans. A Phys. Metall. Mater. Sci.*, 44(11):5018–5024, 2013.

[82] Y.-K. Lee, B.J. Kwak, and J. E. Jin. Microstructures and tensile properties of annealed medium Mn TRIP steels. In TMS, editor, *Proc. Conf. PRICM 7*, page 116, Cairns, Australia, 2010. Symposium A.

[83] R.-M. Sun, W.-H. Xu, C.-Y. Wang, J. Shi, H. Dong, and W. Q. Cao. Work hardening behavior of ultrafine grained duplex medium-Mn steels processed by ART-annealing. *Steel Res. Int.*, 83(4):316–321, 2012.

[84] M. Geiger, M. Merklein, and C. Hoff. Basic Investigations on the Hot Stamping Steel 22MnB5. *Adv. Mater. Reserach*, 6(8):795–804, 2005.

[85] M. Merklein and J. Lechler. Investigation of the thermo-mechanical properties of hot stamping steels. *J. Mater. Process. Technol.*, 177:452–455, 2006.

[86] H. Karbasian and A. E. Tekkaya. A review on hot stamping. *J. Mater. Process. Technol.*, 210(15):2103–2118, 2010.

[87] Q.-H. Han, W.-Z. Bi, X.-Y. Jin, W.-L. Xu, L. Wang, X.-C. Xiong, J. Wang, and P. Belanger. Low-temperature Hot Forming of Medium-Mn Steel. In *5th Int. Conf. Hot Sheet Met. Form. High-Performance Steel*, pages 381–390, 2015.

[88] P. J. Gibbs, E. De Moor, M. J. Merwin, B. Clausen, J. G. Speer, and D. K. Matlock. Austenite stability effects on tensile behavior of manganese-enriched- austenite transformation-induced plasticity steel. *Metall. Mater. Trans. A Phys. Metall. Mater. Sci.*, 42(12):3691–3702, 2011.

[89] T. Furukawa, H. Huang, and O. Matsumura. Effects of carbon content on mechanical properties of 5%Mn steels exhibiting transformation induced plasticity. *Mater. Sci. Technol.*, 10(11):964, 1994.

[90] H.-S. Yang and H. K. D. H. Bhadeshia. Austenite grain size and the martensite-start temperature. *Scr. Mater.*, 60(7):493–495, 2009.

[91] M. Kuzmina, D. Ponge, and D. Raabe. Grain boundary segregation engineering and austenite reversion turn embrittlement into toughness: Example of a 9wt.% medium Mn steel. *Acta Mater.*, 86:182–192, 2015.

[92] J. Hu, W. Q. Cao, C. X. Huang, C. Y. Wang, H. Dong, and J. Li. Characterization of Microstructures and Mechanical Properties of Cold-rolled Medium-Mn Steels with Different Annealing Processes. *ISIJ Int.*, 55(10):2229–2236, 2015.

[93] C. Zhao, W. Q. Cao, C. Zhang, Z. G. Yang, H. Dong, and Y. Q. Weng. Effect of annealing temperature and time on microstructure evolution of 0·2C5Mn steel during intercritical annealing process. *Mater. Sci. Technol.*, 30(7):791–799, 2014.

[94] J.-M. Jang, S.-J. Kim, N. H. Kang, K.-M. Cho, and D.-W. Suh. Effects of annealing conditions on microstructure and mechanical properties of low carbon, manganese transformation-induced plasticity steel. *Met. Mater. Int.*, 15(6):909–916, 2009.

[95] Y. Kawahito, M. Mizutani, and S. Katayama. Elucidation of high-power fibre laser welding phenomena of stainless steel and effect of factors on weld geometry. *J. Phys. D. Appl. Phys.*, 40(19):5854–5859, 2007.

[96] S. Katayama, Y. Kawahito, and M. Mizutani. Elucidation of laser welding phenomena and factors affecting weld penetration and welding defects. *Phys. Procedia*, 5:9–17, 2010.